Online ISSN : 2249-4626
Print ISSN : 0975-5896
DOI : 10.17406/GJSFR

Global Journal

of Science Frontier Research: A

Physics and Space Science

Collapse of Quantum Waves

A Simple Model Unifies Space

Highlights

Alloy Hydrogen Storage Materials

Links of Terrestrial Volcanic Eruptions

Discovering Thoughts, Inventing Future

VOLUME 23 ISSUE 3 VERSION 1.0

Global Journal of Science Frontier Research: A
Physics & Space Science

Global Journal of Science Frontier Research: A
Physics & Space Science

Volume 23 Issue 3 (Ver. 1.0)

Open Association of Research Society

Incorporation No.: 0423089
License No.: 42125/022010/1186
Registration No.: 430374
Import-Export Code: 1109007027
Employer Identification Number (EIN):
USA Tax ID: 98-0673427

Global Journals Inc.

*(A Delaware USA Incorporation with "Good Standing"; **Reg. Number: 0423089**)*
Sponsors: Open Association of Research Society
Open Scientific Standards

Publisher's Headquarters office

Global Journals® Headquarters
945th Concord Streets,
Framingham Massachusetts Pin: 01701,
United States of America
USA Toll Free: +001-888-839-7392
USA Toll Free Fax: +001-888-839-7392

Offset Typesetting

Global Journals Incorporated
2nd, Lansdowne, Lansdowne Rd., Croydon-Surrey,
Pin: CR9 2ER, United Kingdom

Packaging & Continental Dispatching

Global Journals Pvt Ltd
E-3130 Sudama Nagar, Near Gopur Square,
Indore, M.P., Pin:452009, India

Find a correspondence nodal officer near you

To find nodal officer of your country, please email us at *local@globaljournals.org*

eContacts

Press Inquiries: *press@globaljournals.org*
Investor Inquiries: *investors@globaljournals.org*
Technical Support: *technology@globaljournals.org*
Media & Releases: *media@globaljournals.org*

Pricing (Excluding Air Parcel Charges):

Yearly Subscription (Personal & Institutional)
250 USD (B/W) & 350 USD (Color)

Editorial Board

Global Journal of Science Frontier Research

Contents of the Issue

Global Journal of Science Frontier Research: a Physics and Space Science
Volume 23 Issue 3 Version 1.0 Year 2023
Type: Double Blind Peer Reviewed Interenational Research Journal
Publisher: Global Journals
Online ISSN: 2249-4626 & Print ISSN: 0975-5896

Links of Terrestrial Volcanic Eruptions to Solar Activity and Solar Magnetic Field

By Vasilieva Irina & Zharkova Valentina

Northumbria University

Abstract- We compare frequencies of volcanic eruptions (VEs) in the past 270 years with variations of solar activity and summary curve of eigen vectors (EVs) of the solar background magnetic field (SBMF) from the WSO synoptic magnetic maps. In the period 1868 - 1950 and 1990-2020 the total numbers of volcanic eruptions are maximal during the maxima or the descending phase of the magnetic field cycles with the dominant southern polarity, and minimal during the maxima or ascending phase of the magnetic field cycles with the northern polarity. While in the earlier years (1762-1868) this link disappeared. The frequency analysis of VEs with Morlet wavelet reveals the dominant period of about 22 years and weaker periods of 10.7 and 55-70 years. Comparison of VE frequencies with the modulus summary curve (MSC) of EVs of SBMF for solar cycles after 1868 reveals a strong positive correlation (coefficient of 0.84) with the maxima of VEs occurring when the summary curve of EVs derived from the solar magnetic fields have the southern polarity, or more active southern hemisphere of the Sun, and minima when the northern one.

Keywords: volcanic eruption, solar activity, sunspots, magnetic field, eigen vectors, correlation, magnetic pole migration.

GJSFR-A Classification: LCC: QE523.V65, QB529

Strictly as per the compliance and regulations of:

Links of Terrestrial Volcanic Eruptions to Solar Activity and Solar Magnetic Field

Vasilieva Irina [α] & Zharkova Valentina [σ]

Abstract- We compare frequencies of volcanic eruptions (VEs) in the past 270 years with variations of solar activity and summary curve of eigen vectors (EVs) of the solar background magnetic field (SBMF) from the WSO synoptic magnetic maps. In the period 1868 - 1950 and 1990-2020 the total numbers of volcanic eruptions are maximal during the maxima or the descending phase of the magnetic field cycles with the dominant southern polarity, and minimal during the maxima or ascending phase of the magnetic field cycles with the northern polarity. While in the earlier years (1762-1868) this link disappeared. The frequency analysis of VEs with Morlet wavelet reveals the dominant period of about 22 years and weaker periods of 10.7 and 55-70 years. Comparison of VE frequencies with the modulus summary curve (MSC) of EVs of SBMF for solar cycles after 1868 reveals a strong positive correlation (coefficient of 0.84) with the maxima of VEs occurring when the summary curve of EVs derived from the solar magnetic fields have the southern polarity, or more active southern hemisphere of the Sun, and minima when the northern one. The maxima of VE frequencies associated with southern polarity of the summary curve of EVs can be linked with the increased disturbances in the geomagnetic field leading to increased volcanic activity. The correlation between VEs and MSC cycles before 1868 becomes much lower and negative (coefficient -0.33) that can reflect a real change caused by migration of the Earth's magnetic pole to lower latitudes. The next maximum of VEs is expected during cycle 26 when the EVs have the southern polarity that can affect the terrestrial atmosphere transparency and solar radiation input to Earth during the modern Grand Solar Minimum (2020-2053).

Keywords: volcanic eruption, solar activity, sunspots, magnetic field, eigen vectors, correlation, magnetic pole migration.

I. Introduction

Volcanos occur when the inner energy of Earth under its surface approaches a certain critical level, so that the hot magma, which is under a huge inner pressure, can squirt from the Earth's interior through a weak region of the crust producing volcanos. Geomagnetic storms induced by interplanetary coronal mass ejections, interplanetary magnetic fields and solar wind particles [see, for example, [1] and references therein] can cause either sporadic electric currents in the earth locations along the breaks of the surface, which can heat up the surface and reduce their resistivity to the shifts [2], or induce the currents leading to piezoelectric tension of the breaks on the surface leading to volcanos [3].

The Volcanic Explosivity Index (VEI) [4] was introduced for evaluation of the eruption effects on the terrestrial atmosphere based on the estimation of the volume of volcanic eruption materials (ejected tephra, ashflows, pyroclastic flows etc), the height of the ash column, duration of eruption. The eruptions with the VEI=6 and higher can cause the effect of a volcanic winter [5] - a noticeable cooling of the atmosphere caused by the ash pollution that can, in turn, cause anti-greenhouse effect shielding the solar radiation leading to global cooling.

Also the long-term cooling effect of major VEs can be assisted by variations of ozone abundances affected by stratospheric sulphuric aerosols appearing after volcanic eruptions [6, 7]. Ash-rich particles are found to dominate the volcanic cloud optical properties for 2-3 months, while the lifetime of sulphuric aerosols is determined their uptake on ash, rather than by reaction with radicals [8]. Therefore, volcanic activity can be an important component of the solar-terrestrial interaction.

Author α: Dr. Vasilieva Irina, Solar Physics, Main Astronomical Observatory, Street, Kyiv, 03027, State, Ukraine. e-mail: vasil@mao.kiev.ua
Author σ: Prof. Zharkova Valentina, MPEE, Northumbria University, 1 Ellison square, Newcastle, NE1 8ST, Wear and Tear, U.K. e-mail: valentina.zharkova@northumbria.ac.uk
Author α σ: The both authors also worked for ZVS Research Enterprise Ltd., 128 City Road, London, EC1V 2NX, UK.

The early papers tried to link the terrestrial volcanic occurrences with solar activity [9–16]. Later by applying the wavelet analysis to the historical records of large volcanic eruptions other authors managed to establish a connection between the global volcanicity and solar activity cycle of 11 years [17, 18]. Other papers either confirmed [19] or denied [20] the existence of 11 year cycles in a frequency of volcanic eruptions, while some studies showed close relationships between earthquakes, volcanic eruptions and solar activity proxies in the Earth atmosphere [7, 21, 22].

There was a clear correlation detected between the occurrences of large earthquakes at any terrestrial location and high-speed solar wind streams active during solar minima [22–24] and high energy protons, whose densities are known increasing during the maxima of solar activity defined by averaged sunspot numbers [25, 26]. This suggests that geomagnetic storms occurring in the terrestrial atmosphere during maximum years of solar activity can affect the properties of the faults and gestate in some regions with large earthquakes and associated volcanic eruptions [2, 3, 7, 21, 27].

A number of authors discussed existing relationships between proxies for solar activity and climate, including variations in ozone, temperatures, winds, clouds, precipitation, and modes of variability such as the monsoons and the North Atlantic Oscillation (NAO) [see, for example, [6, 7] and references therein]. The volcanic aerosols serve as sources for heterogeneous chemical reactions destroying stratospheric ozone, that can lower absorption of the solar UV radiations and reduces the radiative heating in the lower stratosphere [6]. Most of the authors still support the idea that volcanic activity is increased during minima of solar activity [15, 17, 20], although without providing the confidence levels of their analysis.

The increase of frequency of strong volcanic eruptions during the minima of solar activity was suggested to be associated with the variations of circulation of atmospheric masses in the terrestrial atmosphere induced by the solar input linked to a solar cycle [7]. The further link of volcanic eruptions with solar activity can involve some induced changes in the basic state of the atmosphere caused by the effects energetic particles from solar flares, which can change atmospheric circulation patterns. This was suggested to alter the Earth's spin that, in turn, can lead to moderate earthquakes and volcanos relieving the tension of the volcanic magma [17]. This mechanism could reduce a probability of powerful volcanic eruptions while increase the number of moderate eruptions [17].

Anderson [28] suggested an alternative model, in which the presence of sufficient quantities of volcanic aerosols can change the circulation of the terrestrial atmosphere to such the extent that it would change the velocity of the Earth rotation that, in turn, leading to an increase of earthquakes and eruption of powerful volcanos. At the same time, Bumba [29] demonstrated possible links of longitudinal distribution of solar magnetic fields with geomagnetic disturbances.

Hence, despite definite inks are not clear yet between volcanic eruptions and solar activity, these eruptions can have essential consequences for terrestrial environment by the emergence of volcanic lava and ashes, which can affect terrestrial atmosphere, its energy exchanges, air quality and living conditions in neighbouring cities [5, 6, 17]. Thus, effects of volcanic eruptions, if their frequencies are noticeable, should be included in one or another ways into any models of the global climate changes [30].

Although, there was a recent development of finding a new proxy of solar activity, the eigen vectors of the solar background magnetic field (SBMF) derived with the principle component analysis (PCA) from the synoptic magnetic maps captured by the full-disk magnetograph of the Wilcox Solar Observatory, US [31, 32]. The modulus of the summary curve of the two principal components of SBMF fits rather closely the averaged sunspot numbers currently used as the solar activity index [31–33]. The advantage of the new proxy, the summary curve of PCs, is that it not only provides the amplitudes and shapes of solar activity cycles but also captures the leading magnetic polarities in these cycles and links not only to the sunspot index but also to various solar flare indices [33].

The solar activity was shown to be defined by the solar dynamo action in the two layers of the solar interior producing two magnetic waves having close but not equal periods of about 11 years. The interference of these two magnetic waves leads to a grand period of about 350-400 years for their amplitude oscillations when the normal magnetic wave (and cycle)

amplitudes approach grand solar minima (GSM) caused by the wave's beating effect [32]. Such grand periods coincide with well-known GSMs as Maunder minimum (MM), Wolf and Oort and other grand minima [34]. In fact, the Sun was shown to enter in 2020 the period of a modern GSM lasting until 2053 [32, 35].

Recently, Velasco Herrera et al. [36] using the Bayesian algorithm applied to the averaged sunspot numbers obtained the similar results reporting the modern Grand Solar Minimum to occur in cycles 25-27, similar to that reported by Zharkova et al. [32]. Furthermore, these prediction results about the modern GSM in cycles 25-27 were confirmed by some other researchers [37, 38], who used the same WSO synoptic magnetic field data and obtaining the spectra of the zonal harmonics of the SBMF approaching the GSM, which were interpreted with 3D solar dynamo models.

During the most recent GSM, MM, there was a reduction for solar radiation [39] and the terrestrial temperature by about 1C [40], which, in turn, was proxied by the absence of sunspots and active regions on the solar surface during the MM [34]. Although, the terrestrial temperature was found increasing since Maunder minimum by 0.5C per century [41, 42], which was first assigned to the increase of solar activity producing a modern warming period [43]. However, from cycle 21 the solar activity became systematically decreasing that coincided with a decrease of the solar background magnetic field in the approach of the GSM [31, 32]. And indeed, from cycle 21 the solar activity became systematically decreasing that coincided with a decrease of the solar background magnetic field in the approach of the grand solar minimum (GSM) [32, 33].

On the other hand, in the past few hundred years the Sun was shown to provide some additional radiation to the Earth by moving closer towards the Earth orbit because of the solar inertial motion (SIM) caused by the gravitation of large planets [44, 45]. These periodic variations of the Sun-Earth distance, and the solar irradiance, occur every 2100-2200 years, called Hallstatt's cycles, which were independently derived from the isotope abundances in the terrestrial biomass [46, 47]. In the current Hallstatt's millennial cycle, the Sun-Earth distances are decreasing from the MM until 2600 that leads to the increase of solar irradiance deposited to the atmosphere of the Earth (and other planets) [45]. This SIM effect is likely to contribute to the terrestrial atmosphere heating, in addition to any heating caused by the greenhouse gasses considered in the terrestrial models that requires further investigation.

However, the most essential effect of SBMF in the next few decades will come from a reduction of solar activity, or the modern grand solar minimum, which started in 2020 and will last until 2053 [32]. Geomagnetic storms can be associated with volcanic eruptions [2, 3, 7, 21] either by causing sporadic electric currents [2], or by inducing the currents leading to piezoelectric tension of the breaks on the surface [7]. The scope of the current paper is to establish more definite links between the frequency of volcanic activity and the variations of solar activity using both the sunspot numbers [48] and the new proxy of solar activity linked to eigen vectors of the solar background magnetic field [32, 33].

II. Annual Frequency of Volcanic Eruptions

The information about the volcanic eruptions was derived from the Smithsonian Institution's GVP database [49]. including the volcanoes that are known or suspected to have erupted within the Holocene or Pleistocene. The GVP website provides access to the raw data and a history of volcanic eruptions. The main list of Holocene volcanoes contains 1408 volcanoes associated with 9928 eruptions (version 4.10.0 dated May 14, 2021) [49]. The dates of volcanic eruptions are determined by different methods and with varying precision. There are 2 criteria, which a volcanic eruption must satisfy, in order to be included into this research: it must be accurately dated, and it must be historically confirmed.

Fig. 1 shows the annual frequency of volcanic eruptions, N_{yr}, (violet line) that were recorded from 1700 to 2020 (4961 in total, of which 3822 with VEI ≥ 2), which are are used for investigation of volcanic eruptions numbers links with a solar cycle in section 3.1 and the wavelet spectral analysis in section 3.2. In order to eliminate random variations of the annual

volcanic eruption frequencies, N_{yr}, the data was smoothed with the running averaging filter over an 11 year window and plotted as the averaged (black) curve in Fig. 1. This is the frequency of volcanic eruptions (VEs), which is used in the future statistical analysis in section 3.5.

Also in Fig. 1 we built the envelope curve (red line) along the maximal magnitudes of the averaged curve of volcanic eruption occurrences (black curve). In order to built this curve, we needed to do some interpolation of the data in the gaps when none of the data available. In the last century, the frequency of observed volcanic eruptions, N_{yr}, is higher, and in the twentieth century (1900-1999), 2944 eruptions were observed (of which 1940 with VEI ≥ 2). However, the fixation of a larger number of the eruptions in recent years is most likely due to changes in the method registrations of the eruptions. Completeness of the dates of volcanic eruptions for VEI ≥ 5 begins since 1800, for VEI ≥ 4 - since 1900 and for VEI ≥ 3 - since 1960.

Hence, for building this red curve only in Fig. 1, the interpolation by the cubic spline was carried out for the intermediate magnitudes of the VE averaged frequencies marked by the black curve to produce the red line, during the times when volcanic data were missing, by assuming that in the past three centuries the maximal numbers of volcanic eruptions were similar to that in the past few decades. In this operation we assumed that the data gaps in volcanic eruptions of different strength are a random process that is reasonable assumption for the timescale of 200 years applied, and the trends in the early data have been eliminated by a cubic spline. For all other research in this paper the real counts of VEs are used.

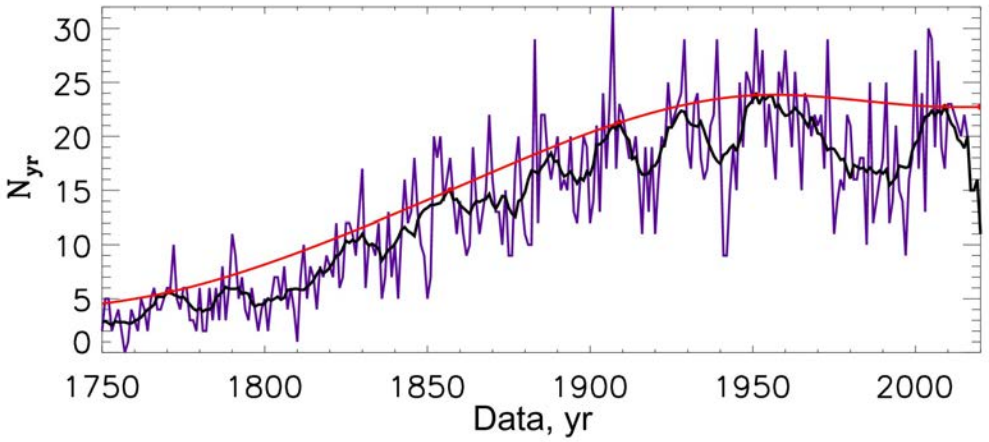

Fig. 1: Total numbers, N_{yr}, of the annual volcanic eruptions in the period of 1750-2020 (violet line). The annual numbers of volcanic eruptions (VEs) averaged with a running filter of 11 years (black line) over-plotted with the envelope curve (red line) marking the maximal magnitudes in the black curve (see text in section 2 for details).

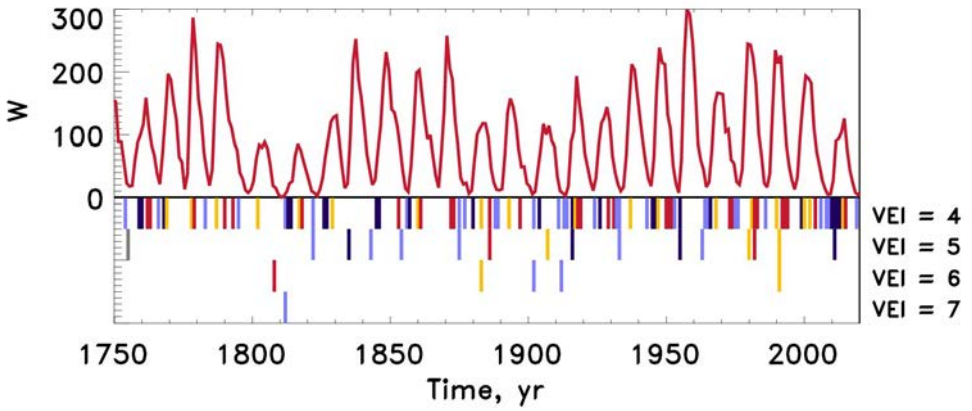

Fig. 2: The averaged sunspot numbers (red curve) describing solar activity in 1750-2020 (top) versus the annual frequencies for volcanic eruptions of different significance (from lower (top line) to higher (bottom line) marked by colour bars. Colours of the bars below the redd curve define the phases of solar activity cycles when eruptions occurred: blue - ascending, yellow - maxima, red - descending and light blue - minima.

III. Data Analysis

3.1 Eruptions frequencies versus averaged sunspot numbers

Solar activity is currently defined by the average number of sunspots and groups on a solar disk at a given day or month. [48]. There is a well-known 11-year cycle of solar activity [48], or a 22-year cycle, during which a complete reversal of the magnetic polarity of the sunspots occurs. The annual numbers of sunspots were taken from the Solar Influences Data Analysis Center (SIDC) at the Royal Observatory of Belgium [1].

The 25 cycles of solar activity occurred during the period of 270 years from 1750 until 2020 are shown in Fig. 2, top plot. The averaged sunspot numbers are plotted versus the available frequencies of the eruption of volcanos of different significance. It is seems that the very strong volcanic eruptions (VEI $\geq$ 5) occur during the minima of solar activity defined by the sunspot index.The further analysis of these links is presented in section 3.4 below.

3.2 Periods of volcanic activity from the wavelet analysis

If the volcanic activity has a periodicity and the dominant one is about 11 years then this would be a good verification of the connection between solar and volcanic activity. This point was investigated following the fruitful results for other active terrestrial features [18] by applying a wavelet spectral analysis with Morlet mother wavelet to the frequencies of volcanic eruptions (VEs) plotted by the black curve in Fig. 1 discussed in section 2, and the result is plotted Fig. 3.

Wavelet transform of signals is the spectral analysis method providing a two-dimensional scan of the analysed signal (time and frequency, or period), in which the coordinates of the time and frequency are independent variables. This representation allows one to explore the properties of the signal simultaneously in time and frequency domains. This makes the wavelet analysis as an excellent tool for examining the series with time-varying frequency characteristics. By considering the time series in the frequency-time space it is possible to derive dominant periods and their variations in time. The mother wavelet was selected as the Morlet wavelet (the real part of it is damped function of cosine), because with this choice one can obtain a high frequency resolution, which is important for our task.

The power of the wavelet spectrum is shown in Fig. 3 by a colour bar plotted next to the wavelet spectrum. The cone of influence (COI) marked by the black dashed line, defines the parts of the spectrum with the essential boarder effects in the starting and finishing parts of the time series, because of a limited statistical data (boarder effects). Consequently, the results outside the COI are excluded from the further investigation, in particularly, in the calculations of the global wavelet spectrum. In order to verify the spectral features derived from the wavelet analysis, Fourier spectrum of the VE frequencies is also calculated and presented by the indigo line in Fig. 3.

The wavelet spectrum of the temporal series of volcanic eruptions (VEs) in 1750-2020 years reveals the two powerful peaks: one occurring at 21.4 ± 1.4 years (corresponding to a double 11 year cycle) and the second one occurring at 55.6± 10.5 years (its nature is unknown yet); although the latter is loosely close to the one of 80 years reported by Stothers [17]. At the same time, the peak near the period of 10.7±0.9 (close to the duration of a single solar activity cycle) previously reported by some researchers [see for example, [17] and references therein] is much less pronounced than the one of 22 years. This double cycle feature indicates the importance of some factors associated with 22 year cycles.

This motivates us to investigate further the link of volcanic eruptions with the solar activity and to use the proxy of solar activity where such the double period naturally occurs. Namely, we need to compare the variations of VE frequencies with the variations of the two eigen vectors (EVs) of SBMF linked to magnetic polarities for each solar cycle, thus, accounting for a double solar cycle of about 22 years. The basics of how these eigen vectors were obtained and what they represent [32] are reiterated below.

[1] http://www.sidc.be/silso/

3.3 Solar background magnetic field as a new solar activity proxy

Recently [32, 33, 50], the Principle Component Analysis was applied to the low-resolution full disk solar background magnetic field (associated with the poloidal magnetic field) measured by the Wilcox Solar Observatory from the synoptic full disk magnetic maps.

We use the temporal variations of the initial vector$\vec{X}$ of latitudinal magnetic waves, $\vec{X}$, obtained from the full disk synoptic magnetic maps with 30 strips in latitude averaged over 360 points in longitudes. By calculating the covariance matrix $C = var\vec{X}$, one can find the eigen values λ_i of this vector $\vec{X}$ by equating the determinant to zero, e.g. $det(C - \lambda I) = 0$, where I is the unity matrix. For each eigen value λ_i one can calculate the corresponding components Y_i of eigen vectors $\vec{Y} = A\vec{X}$ where A is the matrix of regression coefficients. One can find that $var(\vec{Y}_i) = \lambda_i$. The covariance matrix can be also written as $C = ADA^T$, where A^T is the transported matrix A and D is the diagonal matrix of the derived eigen values. In this definition the components $\vec{Y}_i$ of the new vectors $\vec{Y}$ can be assigned to a separate process supported by the variance derived for this component. The components $\vec{Y}_i$ with the largest variance are called principal components (PCs).

The sets of eigen values λ_i and eigen vectors $\vec{Y}_i$ were derived from the observed magnetic synoptic maps and sorted by the variance of the data contributing to each eigen vector, revealing that the eigen values and corresponding eigen vectors come in pairs: first two eiigen values covering for 39% of the observed magnetic data variance, the next two - 18% and for the all four pairs covering for about 95% of the magnetic data variance [33]. The first pair of two largest eigen values with the maximum variances of the data corresponding to the two largest eigenvectors, EVs, were considered to be the Principal Components (PCs).

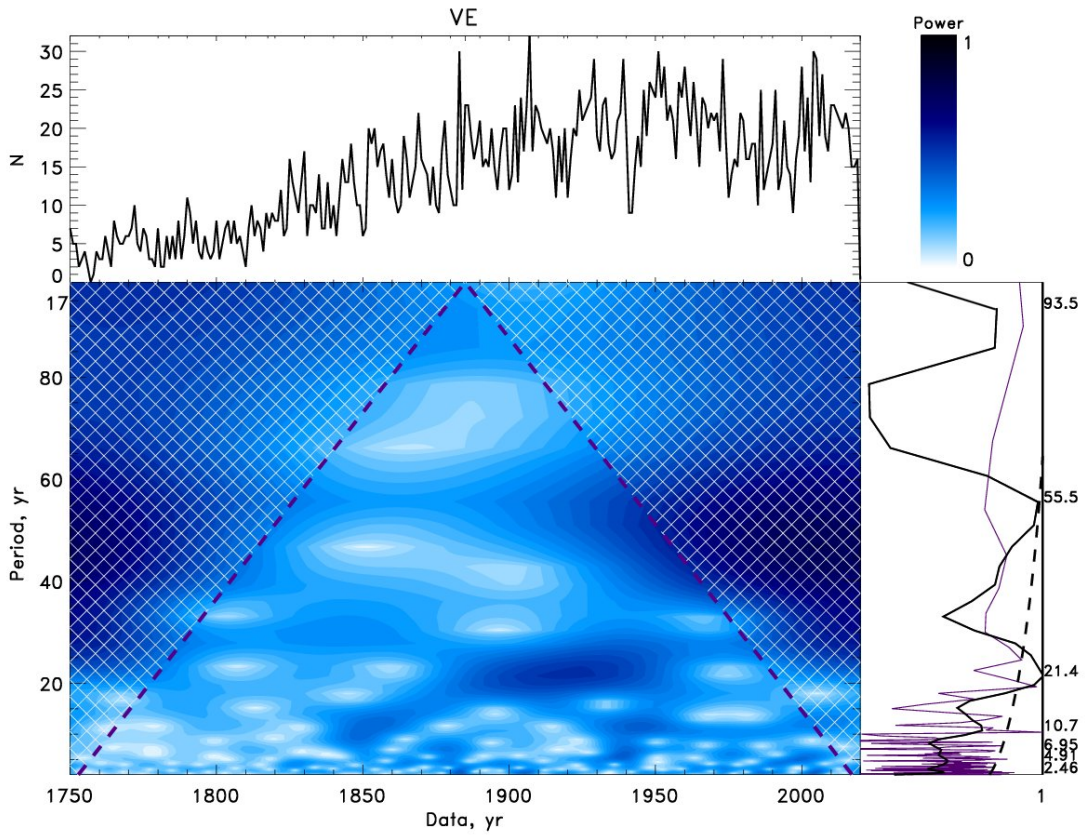

Fig. 3: Top plots: Time series of the annual volcanic eruptions in the period of 1750-2020 (top left) with the power bar for the wavelet spectrum (top right). Bottom plots: The wavelet spectrum with periods (Y-axis) derived from frequencies of volcanic eruptions (bottom left) obtained using the Morlet wavelet. The Cone of Influence (COI) marked by the black dashed line. The global wavelet spectrum (the solid black line) and Fourier spectrum (the indigo line) (bottom right). The black dashed line presents 95% confidence interval for the global wavelet spectrum (see the text in section 3.2 for details).

These two eigen vectors (EVs) were added into a summary curve and suggested as a new, additional proxy of solar activity [32]. These PCs are considered to represent the two dynamo waves in the solar background (poloidal) magnetic field generated by the dynamo mechanism from the dipole magnetic sources [32]. The PCs were described analytically by a series of a few cosine functions by applying the symbolic regression analysis based on the Hamiltonian principle [51] and deriving the mathematical formulae describing the amplitude and phase variations of the resulting waves [31, 32]. The polarity of the summary curve changes periodically from from cycle to cycle being either southern or northern one that indicates which hemisphere of the Sun is more active. The similar indication of the increased activity in a given hemisphere is often reported for each cycle in sunspots [52, 53].

This summary curve of these two PCs derived for cycles 21-23 and predicted for cycle 24-26 [31, 32] is plotted in Fig. 4 (top plot) also showing the variations of the dominant solar background magnetic field: northern for positive and southern for negative amplitudes. The prediction of the summary curve to cycles 25 and 26 presented in Fig. 4 (top plot) taken from Fig. 2, bottom plot in Zharkova et al. [32]) shows a noticeable decrease of the predicted average sunspot numbers in cycle 25 to ≈ 80% of that in cycle 24 and in cycle 26 to ≈ 40% that is linked to a reduction of the amplitudes of solar cycles and an increase of phases between the two eigen vectors of SBMF derived with PCA leading to grand solar minima (GSMs) [32, 50]. The formula for the summary curve, which has a 22 year cycle when the same polarity returns, allows us to do its prediction by thousand years backward and forward presented in Fig.3 [32]. This prediction revealed the occurrence of grand solar cycles of 330-380 years, separated by Grand Solar Minima (GSMs), whose timing reproducing reasonably well the well-known grand minima: Maunder, Wolf, Oort, Homeric and many other ones .

This summary curve was proposed by Zharkova et al. [32] as a new (additional) solar activity proxy since the module of the summary curve fits rather closely the averaged sunspot numbers currently used as a solar activity index (Fig. 4, bottom plot). A close resemblance was found between the modulus summary curve and the curves describing the averaged smoothed sunspot numbers in cycles 21-23 [32] and 21-24 [33] shown here with some small exception for the descending phase of cycle 23, which was later explained by the strongly inflated sunspot numbers used at Locarno observatory [54]. After their correction, the averaged sunspot numbers in cycle 23 fit rather closely the modulus summary curve presented in Fig. 4, bottom plot. Recently, the two PCs, and other eigen vectors of SBMF, were derived from the SBMF data for cycles 21-24 confirming the previous eigen vectors derived from cycle 21-23 [33]. Moreover, the authors demonstrated the links of the summary curve of these PCs to the averaged sunspot numbers for the whole period of sunspot observations from 1700 to 2020 [55] and also shown that other three pairs of eigen vectors are linked to the indices of a flare activity in soft X-ray and radio emission recorded for cycles 21-24 [33].

Hence, from the one hand, this modulus summary curve is found to be a good proxy of the traditional solar activity contained in the averaged sunspot numbers as recently confirmed by [55, 56]. On the other hand, this summary curve is a derivative from the principal components of SBMF with clear mathematical functionalities representing at the same time the real physical processes - poloidal field dynamo waves - generated by the solar dynamo [32]. These points motivated the authors [32] to suggest the summary curve of the two PCs as a new, or additional, proxy of solar activity representing poloidal magnetic field of the Sun, in addition to the sunspot index supposedly linked to the toroidal magnetic field [55].

The suggestion for usage for evaluation of the solar activity of the solar background magnetic field obtained from the same WSO magnetic synoptic maps reported earlier [31, 32] has been recently utilised for the prediction of solar activity in cycle 25, which is expected to have smaller activity compared to cycle 24 [37, 38]. This is in line with our prediction of the modern grand solar minimum (2020-2053) [32, 35]. Some other predictions of cycle 25 based on the analysis of the existing sunspot index in the past 370 years using Artificial Intelligence methods also confirmed the conclusions of lower activity in cycle 25-27 [36, 57].

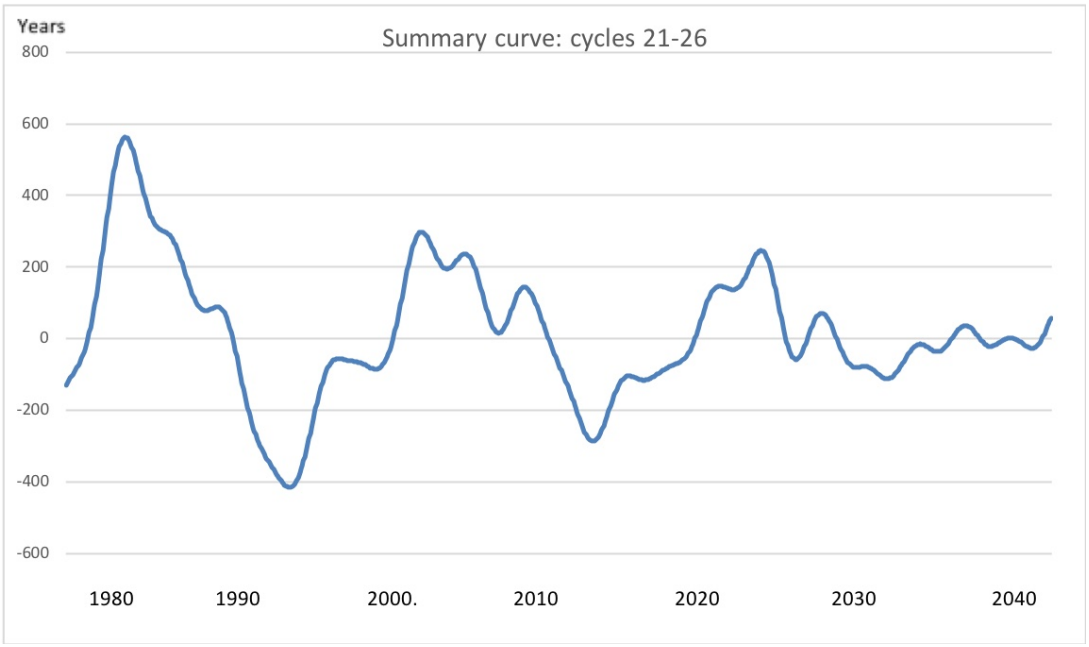

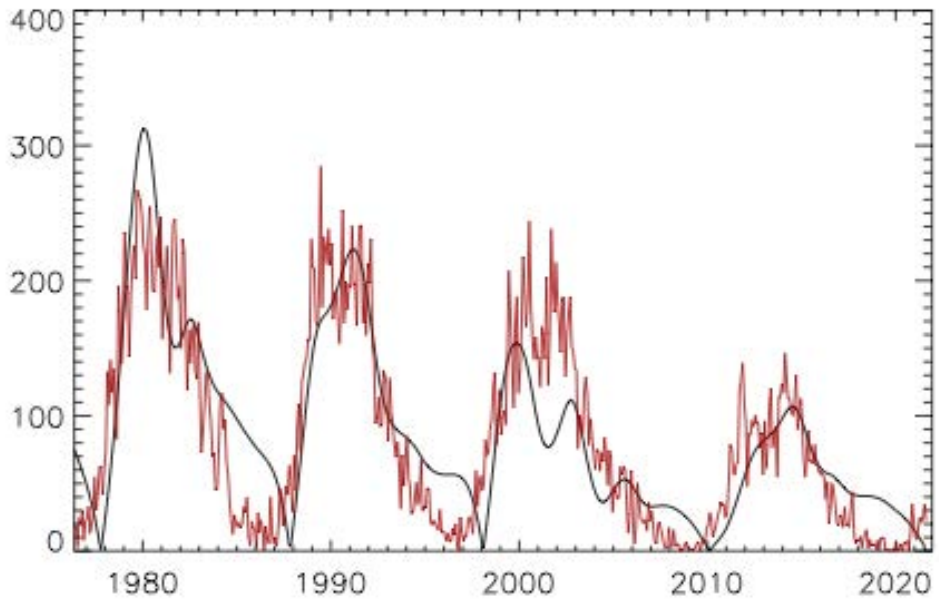

Fig. 4 : Top plot: The summary curve in arbitrary units, of EVs, or PCs, for cycles 21-26 derived from the data for cycles 21-23 and extrapolated for cycles 24, 25 and 26 (a courtesy of [32]). Bottom plot: Modulus summary curve, in arbitrary units, derived from the summary curve above for cycles 21-24 overplotted on the averaged sunspot numbers used as the current solar activity index (a courtesy of [33]) confirming the summary curve of EVs as an additional proxy of solar activity for cycles 21-24.

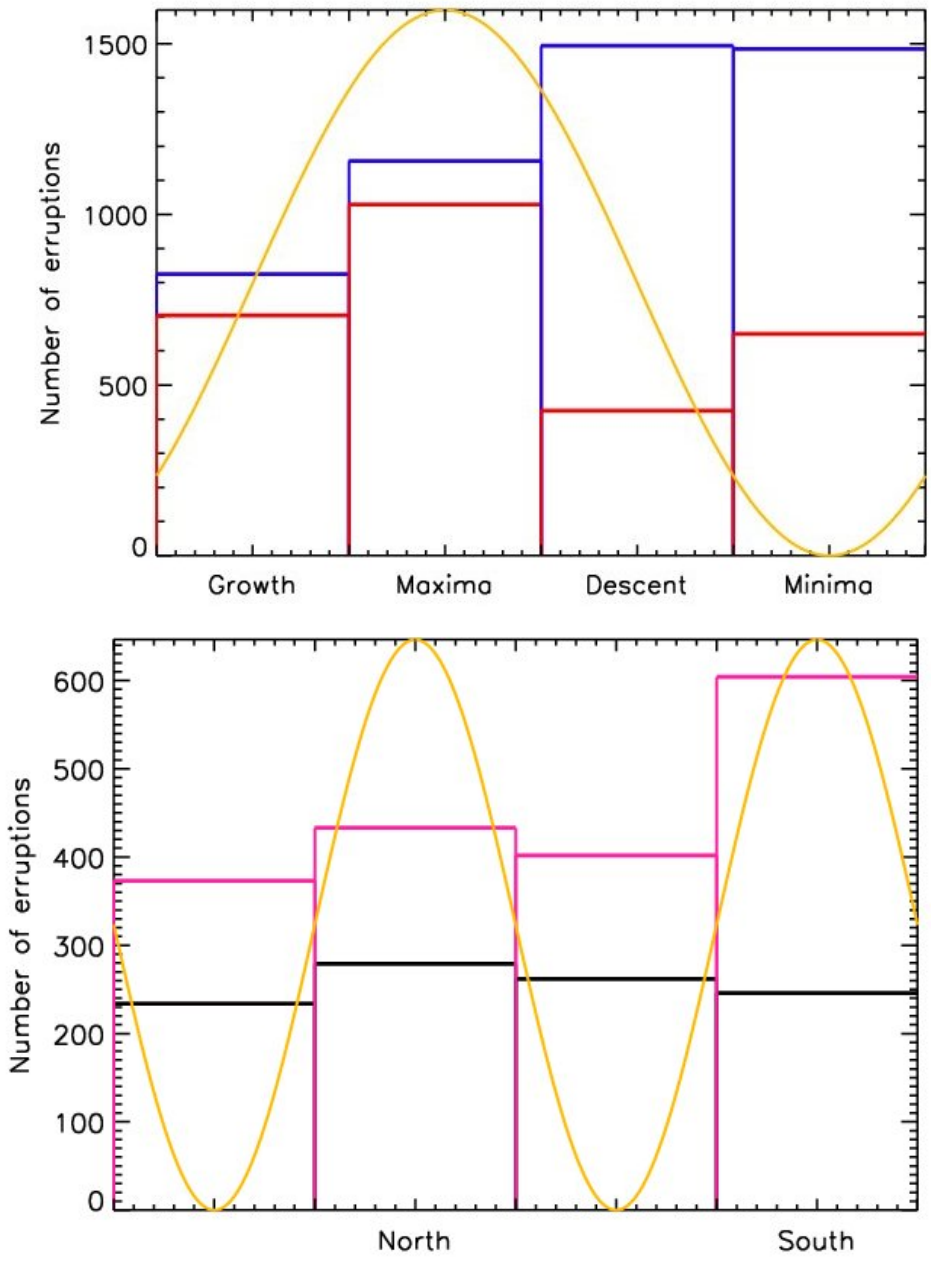

Fig. 5: Top plot: Volcanic eruption (VE) numbers added for the time intervals of four quartiles (see Table 1 and the text for details) of a symbolic 11-year solar cycle (cosine function, yellow line) for the intervals from 1750 until 2020 for the cycles defined by sunspots (blue line) and by eigen vectors, EVs (the red line). The total number of volcanic eruptions is ≈ 4960). Bottom plot - Volcanic eruption (VE) numbers counted for the times of quartiles (see the text for details) of a symbolic 22 year solar cycle (yellow line) emulating the summary curve of eigen vectors (EVs) of SBMF (see Fig. 4, top plot) for the two periods: 1750-1868, 1000 VEs (black line) and 1868-1950, 1800 VEs (magenta line). The total numbers of VEs is ≈ 2800. The leading magnetic polarities (northern and southern) of the summary curve, or the most active solar hemisphere [52, 53], are indicated below X-axis in the positions of 11 year cycle maxima.

3.4 Volcanic eruptions versus solar activity phases

In order to compare volcanic frequencies at different phases of solar cycles, let us define the quartiles of a single 11 year cycle associated with sunspot index and for double 22 year cycle associated with the eigen vectors of SBMF. For each solar cycle of 11 years having a quasi-normal distribution, the maximal and minimal numbers of sunspots are calculated, and the temporal interval between them was divided by 8 to obtain smaller intervals, so that each cycle with two minima and one maximum has 16 points. Then for the ascending (growth) and descending (descent) phases we use 4 intervals counted from the minimum but before maximum, within which a number of VEs are added. For the maximal phase we use four intervals (two from the each side from the maximum) and for the minimal phase we use the four intervals (two from the each minima occurred before and after this cycle). Therefore, each quartile covers approximately even time intervals for different phases of the cycles. The total number of volcanic eruptions was 4960 occurring over the whole time interval from 1750 until 2020.

For the eigen vector cycles of 22 years the rectangles along the time on axis X show the intervals of maxima and minima of double cycles (separating the maxima and minima by the two plus two intervals of the ascending, or descending phases of a 11 year cycle) so that the two lower points go to minimal interval and the two higher points go to the maximal interval. We also indicate for a 22 cycle the leading magnetic polarities in a given 11 year cycle (northern with a positive sign and southern with a negative one). For this case we considered only about 2800 volcanic eruptions occurred in 1750-1950 when their numbers were not potentially affected by the open air nuclear weapon testing [2]. For a comparison with EVs we also divided the total number of VEs into the two periods: 1750-1868 (1000 volcanic events, in total) and 1868-1950 (1800 VEs, in total) following the differences in their occurrences during these intervals (see section 3.5 for more details) caused by either the Earth North pole movement or by weaker solar activity, in general.

The distributions of total numbers of volcanic eruptions in the four quartiles of an 11-year solar cycle (yellow line) shown by the rectangles on the axis X: growth, maximum, descent and minimum are presented in Fig. 5 (top plot) for the whole volcanic dataset (4890 eruptions defined by the violet curve in Fig. 1 defined either by sunspots (blue line, see also Table 1) or by modulus summary curve of EVs (red line). The distributions of the VE subset recorded in 1750-1950 excluding the VEs which are likely to be affected by the open nuclear weapon testing [3] (2800 eruptions, in total, taken from the data plotted by the violet curve in Fig. 1) is shown in Fig. 5 (bottom plot). The symbolic cycle of 11 years is represented by yellow cosine function (with the Y-axis on the right) showing maximal magnitude of unity) and minimal magnitude of 0 (zero).

If 11-year solar cycles are defined by sunspots, then the largest numbers of volcanic eruptions are found to occur during the descending and minimal phases of the solar activity that agrees with the previous findings [17, 20, 27]. However, if the 11-year solar cycle is defined by the modulus summary curve (MSC) of the eigen vectors (EVs) of SBMF defining the solar activity via the complementary poloidal magnetic field [32], then the total numbers of volcanic eruptions (VEs) in the quartiles of the MSC cycles shown by the red lines in Fig. 4, top plot, are maximal during the maxima of MSC and minimal during its minima. These differences in the distributions of the numbers of VEs over the sunspot and MSC solar activity curves (blue and red rectangles, respectively) can indicate either some critical differences in the solar cycles definitions derived from sunspots and from the SBMF, occurring either permanently or during particular periods when the sunspot data availability was not very good, or point out to the real physical differences in solar activity proxies defined from toroidal (sunspots) and poloidal (background) magnetic fields [55].

Furthermore, we can consider a symbolic double cycle of solar activity of 22 years (see Fig. 5, bottom plot) comprising two 11 cycles with the opposite polarities e.g. the MSC for cycles 21 and 22 in Fig. 4, bottom plot, where cycle 21 has EVs of the northern polarity and

[2] https://www.armscontrol.org/factsheets/nucleartesttally
[3] https://www.armscontrol.org/factsheets/nucleartesttally

cycle 22 has EVs of the southern polarity. as shown in Fig. 4, top plot. The magnitudes of these symbolic 11 year cycles marked by yellow lines are shown in the right Y-axis of Fig. 5 varying from 1 (maximum) to 0 (minimum). Then the total numbers of VEs in each quartile versus double cycle of EVs are shown here (see Fig.5, bottom plot) for the selected maximal and minimal quartiles during the intervals of 1750-1868 (black curve), where the numbers of VEs are nearly constant and of 1868-1950 when the maximal numbers of VEs occurs during the maxima of 11 year cycles with southern polarity and the minima of VE numbers - during the maxima of 11 year cycles of with northern polarity of the summary curve indicating a dominant activity in the southern hemisphere of the Sun.

Indeed, in the case of 22-years, or double cycles, there is a clear indication that for the period of 1868-1950 the VE frequencies (indigo lines in Fig.5, bottom plot) are maximal during the magnetic cycle maximum in the 11-year cycles having the EVs with southern magnetic polarity (the second 11-year cycle in Fig.5) compared to the minima occurring during the maximum of magnetic 11 year-cycle with northern polarity. This finding showing the maximal frequencies of volcanic eruptions occurring during the maxima of solar magnetic field activity is closer to the other studies of volcanic and earthquake occurrences in the recent century linking the increase of a geomagnetic activity during the periods of dominant activity in the southern solar hemisphere, e.g. dominant southern polarity of the interplanetary magnetic field [23–26].

While for the earlier period of 1750-1868, the number of volcanic eruptions there is some very small or insignificant increases of VE numbers (black line) during the maxima of magnetic cycles with either northern or southern polarity. These differences between the VE numbers to be nearly constant during a solar 11 years cycle for the early years of the 17-18 centuries while revealing the maximal VE numbers during the maxima of solar 11 year activity with southern polarity in the later years (from the second half of the 19 century) can point out to some natural terrestrial phenomena (e.g. a north pole migration) causing these steady VE numbers during the early years as discussed in section 4.1 below. However, the fact that the distributions of VE numbers in the quartiles are nearly constant for all quartiles for the definition of solar activity by the eigen vectors of SBMF while reveal maximal magnitudes during the descending and minimal phases of the solar activity defined by sunspots allows us to conclude that there are some discrepancies in the solar cycle definitions related either to the objective lack of observations or their dating in the early years before the second half of the 19 century [55].

Table 1: The total number of volcanic eruptions N occurred for a given phase of a solar cycle and % from the total number of eruptions in the cycle derived for several VEI in the period of 1750-2020.

VEI	Growth		Max		Descent		Min		All
	N	%	N	%	N	%	N	%	N
1	171	15.0	269	23.6	324	28.4	375	32.9	1139
2	523	17.0	723	23.5	961	31.3	864	28.1	3071
3	99	16.4	140	23.3	169	28.1	194	32.2	602
4	27	22.4	20	15.9	37	29.4	42	33.3	126
5	5	29.4	3	17.6	2	11.8	7	41.2	17
6	0	0	2	40.0	1	20.0	2	40.0	5
7	0	0	0	0	0	0	1	100.	1
All	825	16.7	1157	23.3	1494	30.1	1485	29.9	4961

3.5 Statistical links of volcanic eruptions with the eigen vector variations

Let us explore furtherthe temporal variations of the frequencies of volcanic eruptions (VE) and variations of the summary curve of the PCs (Fig. 5, bottom plot), or the eigen vectors, EVs, of the SBMF [32] defining the solar activity during the solar cycles from 1750 to 2020.

In order to compare the frequencies of volcanic eruptions with variations of the summary curve of the PCs of SBMF, the arbitrary amplitudes of the summary curve variations were normalised by its maximal magnitude. The comparison of these two series with the frequencies of volcanic eruptions inverted from minima on the top to maxima at the bottom is shown in Fig. 5: in the top plot - for a symbolic 11 year cycle defined by averaged sunspot num-

bers and in the bottom plot - for symbolic double solar cycle defined by 22-year. e.g. two 11 cycles, of the summary curve of eigen vectors (EVs) of SBMF, one cycle with the northern and another with the southern magnetic polarity.

The volcanic eruption (VE) frequencies are presented versus a symbolic 22 year solar cycle (two cosine functions (yellow line) with the opposite polarities as shown in Fig. 5, bottom right plot), imitating two 11 year cycles of a summary curve of eigen vectors (EVs) of SBMF (Fig. 4, top plot). The summary VE frequencies were calculated for the intervals marked by rectangular, for the 2 EV cycles for the two intervals: 1750-1868 (black line) and 1868-1950 &1990-2020 (indigo line).

In the period 1868 - 1950 and 1990-2020 the total number of volcanic eruptions (see Fig. 5, right plot) reveals a clear pattern with their maxima following the maxima or descending phase of the magnetic field curve with the southern polarity and minima follow the maxima or ascending phase of the magnetic field maxima with the northern polarity. While in earlier years (1750-1868) this link is not observed, e.g. the total numbers of volcanic eruptions are nearly the same in any intervals of a 22 year cycle having either northern or southern polarities.

Let us now compare directly these two time series representing temporal evolution of the normalised summary curve of eigen vectors (EV) and the curve of volcanic eruption (VE) frequencies as plotted in Fig. 6: top plot - for real EV of SBMF and VE and bottom plot - for the inverted EV, curve EV1, multiplied by minus unity. The inversion of EV is done so that the maxima of EV1 correspond to the EV cycles with southern polarity and coincide with maxima in VEs, while the minima of VEs correspond to the EV cycles with northern polarity as shown in Fig. 6, bottom plot.

Since we found from Fig. 6 that there were two distinct temporal intervals where the volcanic frequencies show different properties: 1750-1868 and 1868-2020, let us look at the correlation coefficients of these series in Fig. 6 not only for a whole period but also for these two periods, e.g. ”by parts”. From comparing directly the curves VEs and EVs in Fig. 6, top plot, it is evident that the curve of VEs shows, indeed, different level of correspondence with the curve of EVs in the periods of 1750-1868,1868-1950, 1950-1990 and 1990-2020.

There are close correspondences in the curves during the periods of 1868-1950 and 1950-2020, while not clear links between VEs and EVs before 1868 and during the period of 1950-1990. There is a rather weak correspondence of the EV and VE curves in the early years before 1868 whose nature we need to explore. The disappearance of a link of VEs with the solar or terrestrial magnetic fields in 1950s to 1980s can be linked to the open nuclear bomb testing as the link is restored a few decades after this testing was banned and nearly stopped, so this period was omitted from the consideration.

The Spearman correlation analysis of the overall VE and EV1, or the inverted EV data, was carried out using the IBM SPSS Statistics package (v28) for a) the whole interval from 1750 until 2020, b) for the early interval 1750-1868 and c) for the later interval 1868–1950 &1990-2020. The correlation for the whole interval of the datasets VE and EV1 (1750-2020) produced a positive correlation coefficient of 0.21. This low correlation between VE ad EV1 is likely to be affected by the problems with the datasets reported for the periods before 1868 and between 1950-1990. For the period b) of volcanic eruption in 1750-1868 the correlation coefficient of VEs with EV1, or the inverted EVs, was -0.33, while for the volcanic eruptions in the period c) of 1868-1950& 1990-2020 the correlation reaches the high magnitude of 0.84. Definitely, tin the period c) from 1868 onwards (excluding 1950-1990) there is a strong correlation of volcanic eruptions VEs with EVs of the solar magnetic field when it has the southern polarity. This defines a strong correlation of VEs with the summary curve of EVs having southern polarity and minima at EVs with EVs with northern polarity.

The correlation results are also presented for the key two periods b) and c) with the scatter plots seen in Fig. 7 for 1750-1868 (top plot) and for 1868-1950 &1990-2020 (bottom plot) following the links between VE and EV demonstrated in Fig. 6 (top plot). In the plots we present the data fitting for the correlation coefficients with linear and quadratic functions which seem to be rather close. The standard deviations (STDs) from the fits are shown by the inner set of lines about the fits, while the confidence intervals for a 95% confidence level are shown by the outer lines for the both data sets revealing very close fit of the correlation

coefficient in the second period (1868-1950) and much more scattered one in the first one (1750-1868).

Hence, the volcanic eruption (VE) frequencies have maxima every 22 years during the periods when the summary curves of eigen vectors (EVs) have the southern polarity. This coincides with the period of 22 years found from the volcanic eruption frequencies in the wavelet section using the Morlet wavelet shown in Fig. 3. Also this confirms the total numbers of volcanic eruptions shown in Fig. 5 (bottom right plot) during a 22 year cycle (red line) for the period of 1750-1868 (black curve) and 1868-1950 (magenta curve) and the findings that the maximum volcanic eruptions occur during the maxima of solar activity cycles of EVs of SBMF with southern magnetic polarity. Furthermore, this link between VEs and EVs can also explains not only the short term 11/22 year periods of volcanic eruptions but also the longer period of 350 years detected in volcanic eruptions [17], which coincides with the grand solar cycle periods of 350-380 years detected in the EVs of SBMF.

Therefore, a strong correlation of 0.84 (with p value of 0.01) of the frequencies of volcanic eruptions in 1868-1950 and solar magnetic cycles with the southern magnetic polarity of the summary curve, or more active southern hemisphere of the Sun, can be understood in the terms of the accepted views that the increase of geomagnetic disturbances often correspond to an increase in the interplanetary magnetic field of the southern polarity (see, for example, [23, 58–62]). This finding is in line with the other studies showing the high speed solar wind streams during minima of solar activity or possible mass circulation during maxima caused by solar flares and energetic proton fluxes to be the likely drivers of the most powerful earthquakes [24–26] and, possibly, volcanic eruptions [5–7, 17]. A possible reason for the lower correlation in the early years of 1750-1868 is suggested in section 4.1 below.

IV. Discussion and Conclusions

4.1 Volcanic eruptions and motion of the North pole

The Carrington solar event in 1859, the largest recorded solar magnetic event, has been associated with the external field changes with the minimum -1760 nT at the Colaba magnetic Observatory in Bombay [63, 64]. Also, there is the evidence that a geomagnetic jerk has occurred around 1860 [65, 66]. The geomagnetic jerk is a relatively abrupt change in the rate of secular variations in one or more parameters of the Earth's magnetic field. One of the most powerful geomagnetic jerks was observed during of 1969-1970. Until about 1971, the northern magnetic pole moved more or less uniformly at a speed of about 10 km/year, then suddenly began to accelerate. This acceleration of the pole motion can be associated with the so-called geomagnetic jerk that occurred in 1969-1970 [65, 66].

The geomagnetic jerk, which took place around 1860, may help to explain the change in direction of the northern magnetic pole, which was suggested when considering earthquakes [4]. Another possible confirmation of the internal restructuring of the Earth in the 60s of the 19th century may be a sharp change in the direction of the motion of the Earth's magnetic pole (Fig. 8) according to model calculations [5]. The green curve defines the pole movement in 1590-1750, the blue line - in 1750-1860 and the indigo ccurve in 1860-2025 with the small arrows indicating the direction of movement.

We present in Fig. 8 the calculation of the pole movement from 1590 up to 2025 including the shift in 1590-1860 of the magnetic pole far away from it geographic position first to lower latitudes in 1590-1750 (green line), then further shift to lower latitude nearly along the parallel in 1750 - 1860 (blue line) and then turning the pole movement towards its geographical location in 1860-2025 (the indigo line), approaching in 2025 the location1 of 38°057 of the eastern longitude and 85°.778 of the northern latitude. The smaller movements are also recorded in the Southern pole not shown here.

These pole shifts can cause a reduction of the interaction of the terrestrial magnetic field with the solar magnetic field of any polarity that is likely occurred in the early years of observations of solar activity in the 16-17 centuries. Although, after 1860 the pole began returning

[4] https://earthquake.usgs.gov/earthquakes/search/
[5] https://www.ngdc.noaa.gov/geomag/GeomagneticPoles.shtml

back by rapidly approaching the geographic pole position of the Earth that simplified this interaction of the terrestrial magnetic field with the solar magnetic field. This geographical pole position was approached as close as possible in 2018, and after this time the magnetic pole kept moving away again. These dates of the pole movement coincide very well with the periods identified by us from a comparison of the number of volcanic eruptions and the SBMF variations that suggests that the pole movement in the Earth can be the reason of poor interaction of the terrestrial and solar magnetic fields that affects the tension and activity in the terrestrial crusts leading to volcanic eruptions.

4.2 Volcanic eruptions linked to a 22 year magnetic cycle

In this paper we explored the frequencies of volcanic eruptions (VEI ≥ 2, 3829 eruptions) in the past two centuries and their possible links to the variations of solar activity and solar background magnetic field. In the period 1868 - 1950 and 1990-2020 the total numbers of volcanic eruptions are maximal during the maxima or the descending phase of the magnetic field curve with the southern polarity, and minimal during the maxima or ascending phase of the magnetic field maxima with the northern polarity. While in the earlier years (1762-1868) this link disappeared, the total numbers of volcanic eruptions are nearly the same in any intervals of a cycle having either northern or southern polarities if solar activity is defined by either by sunspots or eigen vectors of solar background magnetic field.

By applying the Morlet wavelet analysis to frequencies of VEs, we detected the dominant period of volcanic eruptions to be about 21.4±1.4 years, while there is also a weaker period of 10.7 years similar to that found earlier [17]. This dominant period corresponds to the 22 year period of variations of the summary curve of eigen vectors derived from the solar magnetic field. Curiously enough, the another period of 350 years obtained from the frequency of VEs reported by Stothers [17] can be also accounted by the variations of EVs in a grand solar cycle of 350-380 years reported for SBMF variations [32]. The smaller period of about 50-62 years detected by us is loosely close to the large period of 80 years detected by Stothers [17].

In the next step a direct comparison was carried for the two time series, frequencies of volcanic eruptions, VE, with the summary curve of eigen vectors, EVs, of solar background magnetic field by running the correlation analysis with the SPSS software. During the period of 1868-1950 plus 1990-2020 we derived a rather high positive correlation 0.84 of the number of volcanic eruptions VEs with the southern polarity of the summary curve of EVs derived from the solar background magnetic field representing more active southern hemisphere of the Sun, while during the period 1750-1868 this correlation dropped to the negative one of - 0.33. These correlation coefficients are supported by the scatter plots demonstrating mean fitting curves with standard deviations marked in 95% confidence interval. The strong correlation between the VEs and the summary curve of EVs recorded for 11 cycles of EVs after 1868 suggests that possible physical mechanisms of volcanic eruptions are linked to the processes associated with the increased solar activity features in the southern hemisphere.

This strong link of volcanic eruptions with the summary curve of eigen vectors of southern polarity, or more active southern hemisphere of the Sun, is likely to include the increased electro-magnetic interaction of the solar magnetic field of southern hemisphere with the terrestrial magnetic field causing geomagnetic disturbances [23, 58–61] that can lead to shifts of the crusts, most powerful earthquakes [24] and volcanic eruptions. This can be also influenced by the perturbations of solar wind particles and waves on the Earth's air masses during minima of solar activity [17, 24] or an increase in precipitation of energetic particles during the maxima of solar activity[5–7, 17] that can lead to an increase in the tectonic/volcanic instability.

The possible reasons of a reduced correlation between the volcanic eruptions and solar activity index recorded in the period of 1750-1868 can be associated with the migration of the Earth's North pole towards lower latitudes that disrupts the interaction of the solar magnetic field of southern polarity with the terrestrial magnetic field that can affect the status of the Earth crusts and lead to volcanic eruptions. Although, some of the differences between the distributions of eruption frequencies over the phases of solar cycles of 11 years can be related to the differences in solar activity indices defined by sunspots and the eigen vectors of magnetic fields, that is related to actions different types of solar magnetic fields, toroidal and poloidal [55]. While the increase of volcanic eruptions and the lack of correlation in 1950-

1980 can be linked to the open air nuclear bomb testings that distorted natural effects of the interaction of magnetic fields of the Sun and Earth.

In summary, the increase of volcanic eruptions established during the solar activity cycles with the southern polarity of SBMF emphasises the importance of the solar-terrestrial interaction in volcanic eruptions and their effects on the terrestrial climate [30]. This link can also play an important role in the next few decades affected by the modern Grand Solar Minimum (2020-2053) [32, 35] because in cycle 26 the summary EV of the solar background magnetic field will have the southern polarity. Hence, despite the links between volcanic occurrences and solar activity become only established for 8 solar cycles in the past century and in the last four cycles of this century, the consequences of volcanic eruptions for the terrestrial atmosphere can be noticeable during cycle 26 with the southern polarity of solar magnetic field. This can affect the terrestrial atmosphere transparency [8] and can result in further reduction of the terrestrial temperature during the modern GSM (2020-2053).

Acknowledgments

The authors wish to express their many thanks to the Smithsonian Institution staff for providing the access to the GVP database containing the volcanic eruption data and the Solar Influences Data Analysis Center (SIDC) at the Royal Observatory of Belgium for providing the averaged sunspot numbers. The authors also express their deepest gratitude to the staff and directorate of Wilcox Solar Observatory, Stanford, US, for providing the coherent long-term observations of full disk synoptic maps of the solar background magnetic field.

Author contributions statement

I.V. gathered and processed the volcanic frequency data while V.Z. provided and analysed the solar background magnetic field data and carried statistical analysis of the data with the SPSS package. V.Z. and I.V. compared and analysed the results, wrote and reviewed the manuscript.

Additional information

The authors do not have any competing financial interests.

References Références Referencias

1. Stamper, R., Lockwood, M., Wild, M.N., Clark, T.D.G.: Solar causes of the long-term increase in geomagnetic activity. J. Geophys. Research 104(A12), 28325–28342 (1999) https://doi.org/10.1029/1999JA900311
2. Han, Y.Z., Guo, J.W., Ma, C.L.: Possible triggering of solar activity to big earthquakes (Ms8) in faults with near west-east strike in China. Sci. China Ser. B: Phys. Mech. Astron 47, 173–181 (2004) https://doi.org/10.1360/ 03yw0103
3. Sobolev, N.V., Demin, V.M.: Mechano-electrical Phenomena in the Earth, p. 215. Nauka, ??? (1980). https://books.google.co.uk/books?id=RcbgvwEACAAJ
4. Newhall, C., Self, S.: The Volcanic Explosivity Index (VEI): An Estimate of Explosive Magnitude for Historical Volcanism. J. Geophys. Research 87, 1231–1238 (1982) https://doi.org/10.1029/JC087iC02p01231
5. Rampino, M.R., Self, S., Stothers, R.B.: Volcanic Winters. Annual Review of Earth and Planetary Sciences 16, 73 (1988) https://doi.org/10.1146/annurev.ea.16.050188.000445
6. Robock, A.: Volcanic eruptions and climate. Reviews of Geophysics 38(2), 191–219 (2000) https://doi.org/ 10.1029/1998RG000054
7. Gray, L.J., Beer, J., Geller, M., Haigh, J.D., Lockwood, M., Matthes, K., Cubasch, U., Fleitmann, D., Harrison, G., Hood, L., Luterbacher, J., Meehl, G.A., Shindell, D., Geel, B., White, W.: Solar influences on climate. Reviews of Geophysics 48(4) (2010) https://doi.org/10.1029/2009RG000282
8. Zhu, Y., Toon, O.B., Jensen, E.J., Bardeen, C.G., Mills, M.J., Tolbert, M.A., Yu, P., Woods, S.: Persisting volcanic ash particles impact stratospheric SO2 lifetime and aerosol optical properties. Nature Communications 11, 4526 (2020) https://doi.org/10.1038/s41467-020-18352-5

9. Kluge, E.: Ueber Synchronismus und Antagonismus Yon Vulkanischen Eruptionen und die Beziehungen Derselben zu Den Sonnenfiecken und Erdmagnetischen Variationen. Engelmann, Leipzig (1863).
10. Kluge, E.: Ueber Synchronismus und Antagonismus Yon Vulkanischen Eruptionen und die Beziehungen Derselben zu Den Sonnenfiecken und Erdmagnetischen Variationen. Nabu Press, ??? (2012).
11. De Marchi, L.: Nuove Teorie Sulle Cause Dell 'Era Glaciale'. Scientia 5(9), 310 (1911).
12. Köppen, W.: Parallelismus zwischen der häufigkeit der sonnenflecken und der vulkanausbr¨uche. Himmel und Erde 8, 529–532 (1896).
13. Lyons, C.J.: Sun Spots and Hawaiian Eruptions. Monthly Weather Review 27(4), 144 (1899) https://doi.org/ 10.1175/1520-0493(1899)27[144a:SSAHE]2.0.CO;2
14. O'Reilly, J.P.: On the dates of volcanic eruptions and their concordance with the sunspot period. Proceedings of the Royal Irish Academy (1889-1901) 5, 392–432 (1898).
15. Jensen, H.I.: Possible relation between sunspot minima and volcanic eruptions. Journal and Proceedings of the Royal Society of New South Wales 36(2), 42–60 (1902)
16. Sapper, K.: Cycles of volcanic activity. Volcano Letters 302, 2–4 (1930)
17. Stothers, R.B.: Volcanic eruptions and solar activity. J. Geophys. Research 94, 17371–17381 (1989) https://doi.org/10.1029/JB094iB12p17371
18. Mazzarella, A., Palumbo, A.: Does the solar cycle modulate seismic and volcanic activity. J. Volcanology and Geothermal Research 39, 89–93 (1989)
19. Ma, L., Yin, Z.Q., Han, Y.: Possible influence of solar activity on global volcanicity. Earth Science Research 7, 110 (2018) https://doi.org/10.5539/esr.v7n1p110
20. Střeštik, J.: Possible correlation between solar and volcanic activity in a long-term scale. In: Wilson, A. (ed.) Solar Variability as an Input to the Earth's Environment. ESA Special Publication, vol. 535, pp. 393–396 (2003)
21. Schneider, S.H., Mass, C.: Volcanic Dust, Sunspots, and Temperature Trends. Science 190(4216), 741–746 (1975) https://doi.org/10.1126/science.190.4216.741
22. Herdiwijaya, D., Arif, J., Nurzaman, M.Z., Astuti, I.K.D.: On the possible relations between solar activities and global seismicity in the solar cycle 20 to 23. In: The 5th International Conference on Mathematics and Natural Sciences. American Institute of Physics Conference Series, vol. 1677, p. 050003 (2015). https://doi.org/10.1063/ 1.4930664
23. Gonzalez, W.D., Tsurutani, B.T., Cl´ua de Gonzalez, A.L.: Interplanetary origin of geomagnetic storms. Space Sci. Reviews 88, 529–562 (1999) https://doi.org/10.1023/A: 1005160129098
24. Odintsov, S., Boyarchuk, K., Georgieva, K., Atanasov, D.: Long-period trends in global seismic and geomagnetic activity and their relation to solar activity. J. Physics and Chemistry of the Earth 31, 88–93 (2006) https://doi.org/ 10.1016/j.pce.2005.03.004
25. Martichelli, V., Harabaglia, P., Troise, C., De Natale, G.: On the correlation between solar activity and large earthquakes worldwide. Scientific Reports 10, 11495 (2020) https://doi.org/10.1038/s41598-020-67860-3
26. Martichelli, V., Harabaglia, P., Troise, C., De Natale, G.: On the Long Range Clustering of Global Seismicity and its Correlation With Solar Activity: A New Perspective for Earthquake Forecasting. Front.Earth Sci 10 (2020) https://doi.org/10.3389/feart.2020.595209
27. Herdiwijaya, D., Johan, A., Nurzaman, M.Z.: On the Relation between Solar and Global Volcanic Activities. In: Proceedings of the 2014 International Conference on Physics, pp. 105–108. Atlantis Press, ??? (2014). https://doi.org/10.2991/icp-14.2014.21
28. Anderson, D.L.: Earthquakes and the Rotation of the Earth. Science 186(4158), 49–50 (1974) https://doi.org/ 10.1126/science.186.4158.49

29. Bumba, V.: Solar local magnetic fields and their relations to the background fields. Contributions of the Astronomical Observatory Skalnate Pleso 15, 495 (1986)
30. Hagen, M.-T., Azevedo, A.: Influence of volcanic activity on weather and climate change. Atmospheric and Climate Science 13, 138–158 (2023) https://doi.org/ 110.4236/acs.2023.132009
31. Shepherd, S.J., Zharkov, S.I., Zharkova, V.V.: Prediction of Solar Activity from Solar Background Magnetic Field Variations in Cycles 21-23. Astrophysical J. 795, 46 (2014) https://doi.org/10.1088/0004-637X/795/1/46
32. Zharkova, V.V., Shepherd, S.J., Popova, E., Zharkov, S.I.: Heartbeat of the Sun from Principal Component Analysis and prediction of solar activity on a millenium timescale. Scientific Reports 5, 15689 (2015) https://doi.org/10.1038/srep15689
33. Zharkova, V.V., Shepherd, S.J.: Eigen vectors of solar magnetic field in cycles 21-24 and their links to solar activity indices. Monthly Notices of Royal Astron.Soc. 512, 5085–5099 (2022) https://doi.org/10.1111/j.1365-2966.2012.21436.x
34. Eddy, J.A.: The Maunder Minimum. Science 192, 1189–1202 (1976) https://doi.org/10. 1126/science.192. 4245.1189
35. Zharkova, V.: Modern grand solar minimum will lead to terrestrial cooling. Editorial paper, Temperature 7(3), 217–222 (2020) https://doi.org/10.1080/ 23328940. 2020.1796243
36. Velasco Herrera, V.M., Soon, W., Legates, D.R.: Does Machine Learning reconstruct missing sunspots and forecast a new solar minimum? Advances in Space Research 68(3), 1485–1501 (2021) https://doi.org/10.1016/ j.asr.2021.03.023
37. Kitiashvili, I.N.: Application of Synoptic Magnetograms to Global Solar Activity Forecast. Astrophysical J. 890(1), 36 (2020) https://doi.org/10.3847/1538-4357/ab64e7arXiv:1910.00820 [astro-ph.SR
38. Obridko, V.N., Sokolo_, D.D., Pipin, V.V., Shibalvaa, A.S., Livshits, I.M.: Zonal harmonics of solar magnetic field for solar cycle forecast. Monthly Notices of Royal Astr. Soc, 4990–5000 (2021) arXiv:2108.10527 [astro-ph.SR]
39. Lean, J., Beer, J., Bradley, R.: Reconstruction of solar irradiance since 1610: Implications for climate change. Geophys. Res. Letters 22(23), 3195–3198 (1995) https://doi.org/10.1029/95GL03093
40. Easterbrook, D.J.: Evidence-based Climate Science. Elsevier, ??? (2016)
41. Parker, D.E., Jones, P.D., Folland, C.K., Bevan, A.: Interdecadal changes of surface temperature since the late nineteenth century. J. Geophys. Research: Atmospheres 99(D7), 14373–14399 (1994) https://doi.org/10.1029/ 94JD00548
42. Akasofu, S.-I.: On the recovery from the little ice age. Natural Science 2, 1211–1224 (2010) https://doi.org/ 10.1007/s11214-011-9856-y
43. Lockwood, M., Stamper, R.,Wild, M.N.: A doubling of the Sun's coronal magnetic field during the past 100 years. Nature 399(6735), 437–439 (1999) https://doi.org/ 10.1038/20867
44. Zharkova, V.V., Shepherd, S.J., Zharkov, S.I., Popova, E.: RETRACTED ARTICLE: Oscillations of the baseline of solar magnetic field and solar irradiance on a millennial timescale. Scientific Reports 9, 9197 (2019) https://doi.org/10.1038/s41598-019-45584-3
45. Zharkova, V.: Millennial Oscillations of Solar Irradiance and Magnetic Field in 600-2600. chapter in a book "Solar system planets and exoplanets", 30 (2021) https://doi.org/10.5772/intechopen.96450
46. Steinhilber, F., Beer, J., Fr¨ohlich, C.: Total solar irradiance during the Holocene. Geophys. Res. Letters 36(19), 19704 (2009) https://doi.org/10.1029/ 2009GL040142
47. Steinhilber, F., Abreu, J.A., Beer, J., Brunner, I., Christl, M., Fischer, H., Heikkila, U., Kubik, P.W., Mann, M., McCracken, K.G., Miller, H., Miyahara, H., Oerter, H., Wilhelms, F.: 9,400 years of cosmic radiation and solar activity from ice cores and tree rings. Proceedings of the National Academy of Science 109(16), 5967–5971 (2012) https://doi.org/10.1073/pnas.1118965109

48. Wolf, R.: Studies on the frequency of Sun-spots, and on their connexion with the Magnetic Declination-variation. Monthly Notices of Royal Astron. Soc. 30, 157 (1870) https://doi.org/10.1093/mnras/30.6.157
49. Global Volcanism Program, G.: Volcanoes of the World, v. 4.10.0 (14 May 2021). Downloaded June 9, 2021 (2013). https://doi.org/10.5479/si.GVP.VOTW4-2013
50. Zharkova, V.V., Shepherd, S.J., Zharkov, S.I.: Principal component analysis of background and sunspot magnetic field variations during solar cycles 21-23. Monthly Notices of Royal Astron.Soc. 424, 2943–2953 (2012) https://doi.org/10.1111/j.1365-2966.2012.21436.x
51. Schmidt, M., Lipson, H.: Distilling free-form natural laws from experimental data. Science 324(5923), 81–85 (2009) https://doi.org/10.1126/science.1165893
52. Temmer, M., Veronig, A., Hanslmeier, A.: Hemispheric Sunspot Numbers Rn and Rs: Catalogue and N-S asymmetry analysis. Astronomy ans Astrophysics 390, 707–715 (2002) https://doi.org/10.1051/0004-6361:20020758 arXiv:astro-ph/0208436[astro-ph]
53. Zharkov, S., Zharkova, V.V., Ipson, S.S.: Statistical Properties Of Sunspots In 1996 2004: I. Detection, North South Asymmetry And Area Distribution. Solar Physics 228(1-2), 377–397 (2005) https://doi.org/10.1007/s11207-005-5005-7
54. Clette, F., Svalgaard, L., Vaquero, J.M., Cliver, E.W.: Revisiting the Sunspot Number. A 400-Year Perspective on the Solar Cycle. Space Science Reviews 186, 35–103 (2014) https://doi.org/10.1007/s11214-014-0074-2
55. Zharkova, V.V., Vasilieva, I., Shepherd, S.J., Popova, E.: Comparison of solar activity proxies: eigen vectors versus averaged sunspot numbers. arXiv e-prints, 2207–147082 (2022) https://doi.org/10.48550/arXiv. 2207.14708
56. Zharkova, V.V., Vasilieva, I., Popova, E., Shepherd, S.J.: Comparison of solar activity proxies: eigen vectors versus averaged sunspot numbers. Monthly Notices of Royal Astron.Soc. in press (2023) https://doi.org/10.1093/mnras/stad1001
57. Courtillot, V., Lopes, F., Le Mou¨el, J.L.: On the Prediction of Solar Cycles. Solar Phys. 296(1), 21 (2021) https://doi.org/10.1007/s11207-020-01760-7
58. Maezawa, K.: Dependence of the magnetopause position on the southward interplanetary magnetic field. Planetary and Space Science J. 22(10), 1443–1453 (1974) https://doi.org/10.1016/0032-0633(74)90040-3
59. Perreault, P., Akasofu, S.-I.: A study of geomagnetic storms. Geophys. Journal 54, 547–573 (1978) https://doi.org/10.1111/j.1365-246X.1978.tb05494.x
60. Stauning, P.: Coupling of IMF BY variations into the polar ionospheres through interplanetary field-aligned currents. J. Geophys. Research 99(A9), 17309–17322 (1994) https://doi.org/10.1029/94JA00927
61. Stauning, P., Clauer, C.R., Rosenberg, T.J., Friis-Christensen, E., Sitar, R.: Observations of solar-wind-driven progression of interplanetary magnetic field BY -related dayside ionospheric disturbances. J. Geophys. Research 100(A5), 7567–7586 (1995) https://doi.org/10.1029/94JA01825
62. Prosovetsky, D., Myagkova, I.: The correlation between geomagnetic disturbances and topology of quasi-open structures in the solar magnetic field. Geomagnetism and Aeronomy 51 (2011) https://doi.org/10.1134/S0016793211080342
63. Cliver, E.W., Dietrich, W.F.: The 1859 space weather event revisited: limits of extreme activity. Journal of Space Weather and Space Climate 3, 31 (2013) https://doi.org/10.1051/swsc/2013053
64. Mandea, M., Chambodut, A.: Geomagnetic field processes and their implications for space weather. Surveys in Geophysics 41 (2020) https://doi.org/10.1007/s10712-020-09598-1
65. Newitt, L.R., Dawson, E.: Secular variation in North America during historical times. Geophysical Journal 78(1), 277–289 (1984) https://doi.org/10.1111/j.1365-246X.1984.tb06484.x

66. Newitt, L., Mandea, M., McKee, L., Orgeval, J.-J.: Recent acceleration of the north magnetic pole linked to magnetic jerks. EOS Transactions 83, 381 (2002) https://doi.org/10.1029/2002EO000276

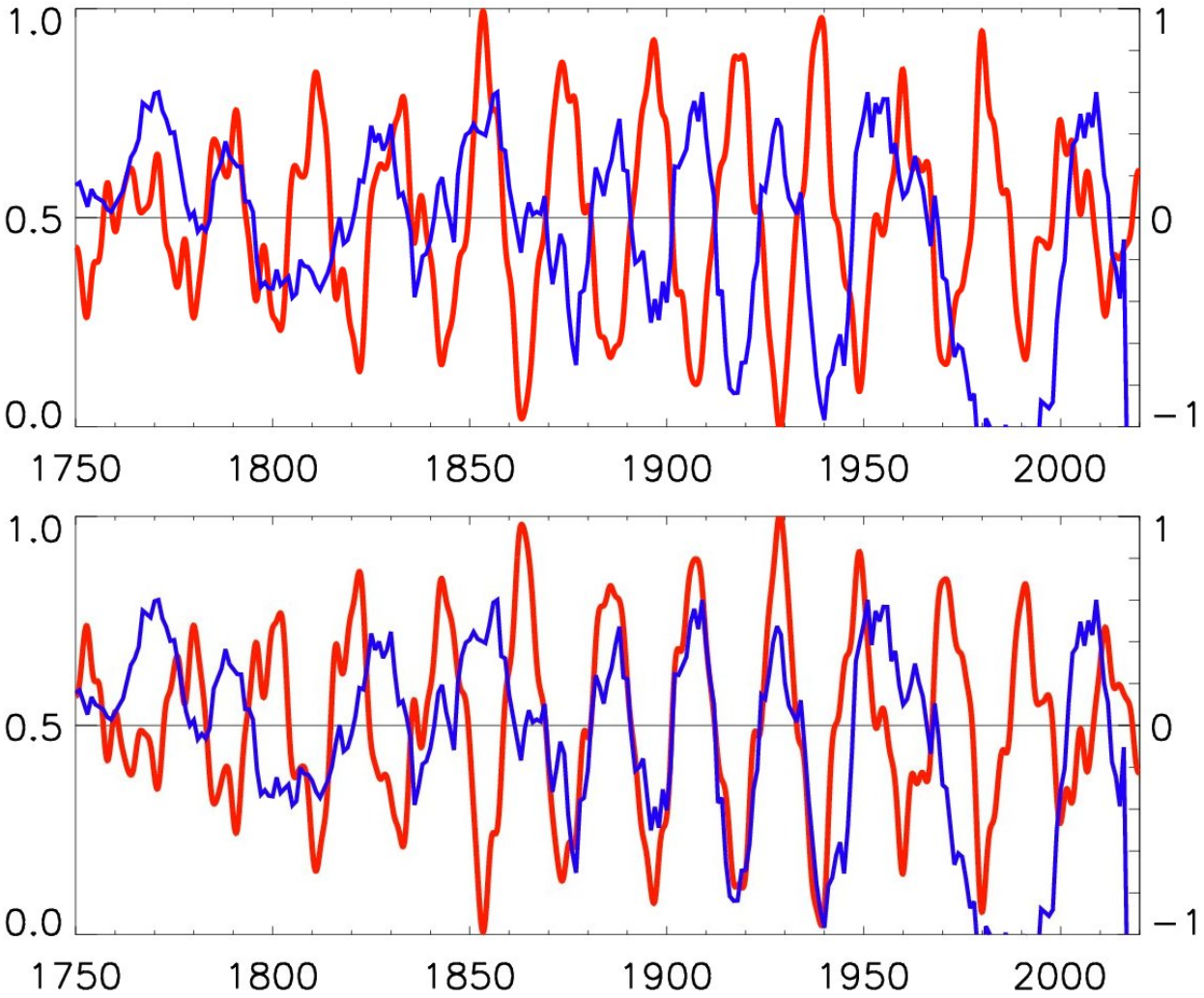

Fig. 6: Top plot: The summary curve of eigen vectors (EV) of the solar background magnetic field [32] (red curve) normalised by its maximum (the right Y-axis) versus the averaged normalised number of volcanic eruptions (VEs) (blue curve) (the left Y-axis). Positive magnitudes of the summary curve correspond to the northern polarity and negative ones to the southern polarity of SBMF. Bottom plot: the volcanic eruption (VE) numbers (left Y-axis, blue line) versus the inverted summary curve of eigen vectors (EV1) (the right Y-axis, red line) with positive magnitudes corresponding to southern polarity and negative to the northern one. For the correlation coefficients between these two curves see the text and Fig.7.

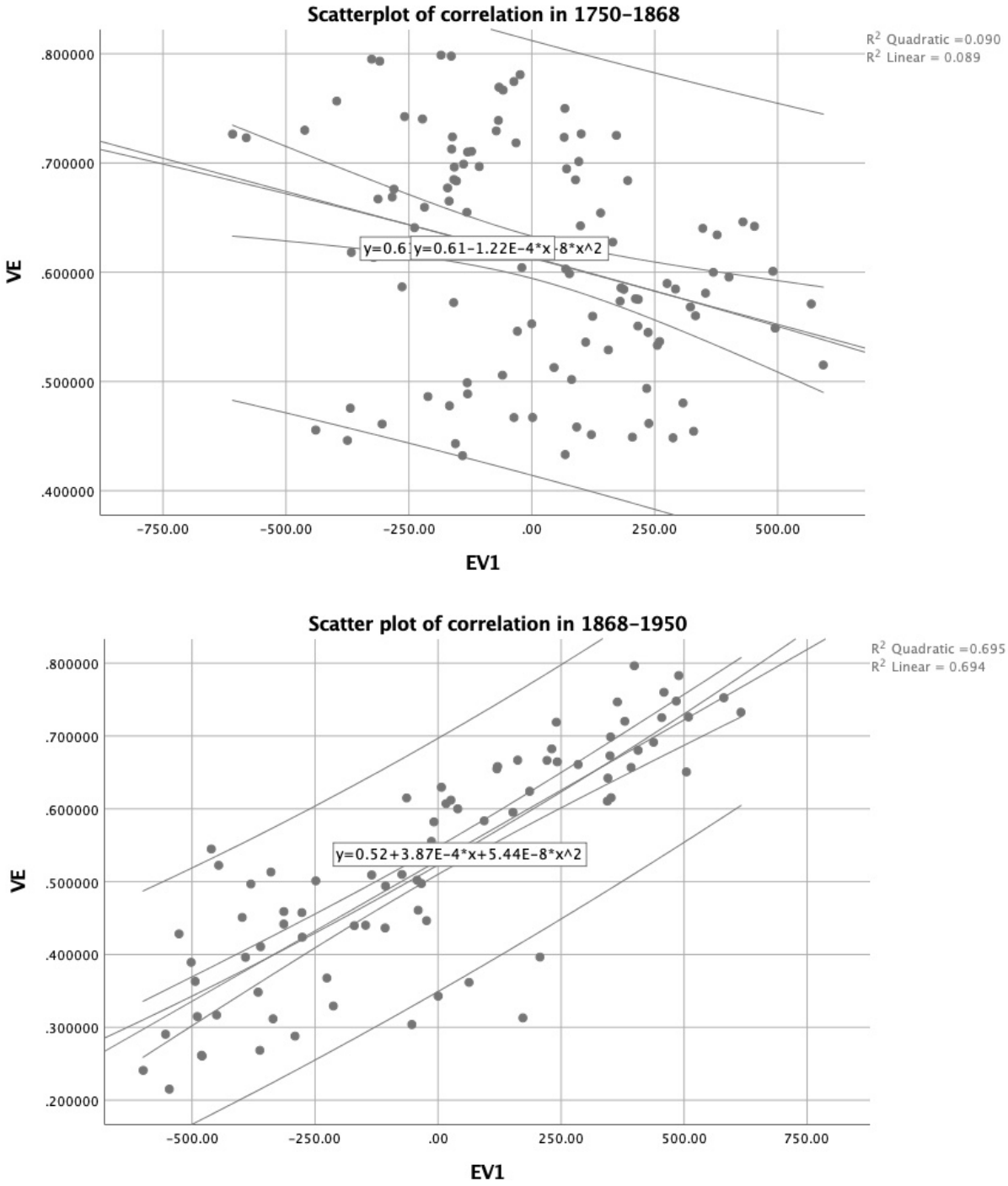

Fig. 7: Top plot: A scatter plot of correlation of the normalised volcanic eruption (VE) frequency with the inverted summary curve of eigen vectors (EV1) of SBMF for the data from 1750-1868 with Spearman correlation coefficient of -0.325., p value 0.01 Bottom plot: The scatter plot of the correlation of VE frequency with the inverted summary curve of eigen vectors (EV1) for 1868-1950 with Spearman correlation coefficient of 0.840, p value of 0.01. This defines a strong correlation of VEs with the summary curve of EVs having southern polarity and minima at EVs with EVs with northern polarity. The central lines provide the best linear and quadratic fits (with formula) of correlation coefficients, the near lines define standard deviations of the fits and the outer lines show the 95% confidence intervals for the derived correlation.

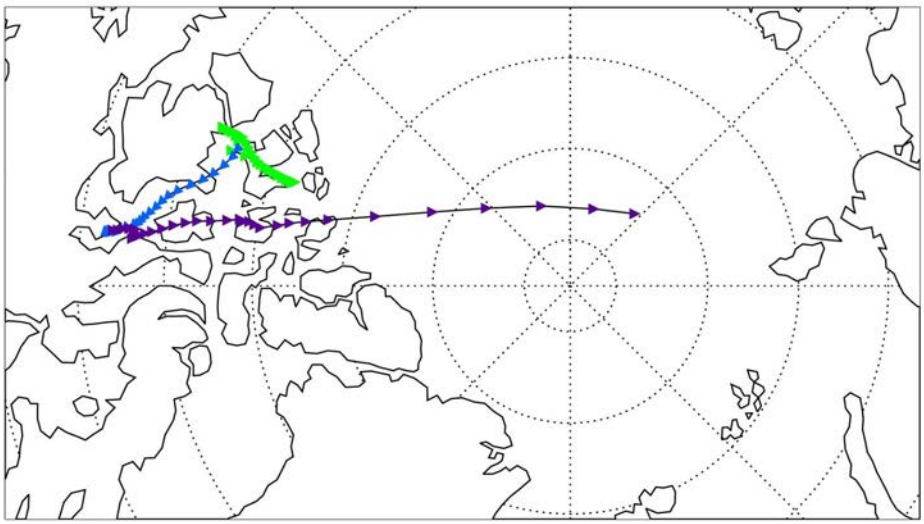

Fig. 8: Reconstructed locations of the North magnetic pole from 1590 to 2025, namely in 1590-1750 (green curve), 1750-1860 (blue curve) and 1860-2025 (violet curve) (see for details section 4.1).

This page is intentionally left blank

Global Journal of Science Frontier Research: a Physics and Space Science
Volume 23 Issue 3 Version 1.0 Year 2023
Type: Double Blind Peer Reviewed Interenational Research Journal
Publisher: Global Journals
Online ISSN: 2249-4626 & Print ISSN: 0975-5896

The Role of Poincaré Resonances in the Collapse of Quantum Waves and in the Formation of Consciousness

By Elcio Fabio Soares Pereira

The University of Utah

Abstract- He comments briefly on having shown in previous works that the factors that make possible the formation of a biological consciousness would also serve for the formation of a primary universal consciousness, including a hypothesis by Amit Goswami of the need for this primary consciousness in the solution of an intertwined hierarchy. According to his opinion, this intertwined hierarchy would appear in the collapse of quantum waves, a process that is necessary for the formation of human consciousness.

Next, he addresses the theme proposed in the title of this work, which constitutes his hypothesis that the collapse of quantum waves is caused by Poincaré Resonances. It presents and discusses aspects that justify and result from this hypothesis, showing the similarity between the behavior of these resonances and that of the synapses that occur between neurons in the human brain. It also presents an attempt to resolve the impasse of the coexistence of a conscience, supposedly immaterial, with matter in the same realm being discarded the dualism, a philosophy little accepted by the scientific community.

Keywords: *resonance, collapse, waves, consciousness.*

GJSFR-A Classification: *MSC - 81P10*

Strictly as per the compliance and regulations of:

The Role of Poincaré Resonances in the Collapse of Quantum Waves and in the Formation of Consciousness

O Papel Das Ressonâncias De Poincaré No Colapso Das Ondas Quânticas E Na Formação Da Consciência

Elcio Fabio Soares Pereira

Resumo- Comenta sucintamente ter mostrado em trabalhos anteriores que os fatores que possibilitam a formação de uma consciência biológica possibilitariam também a formação de uma consciência universal primária e apresenta uma hipótese de Amit Goswami sobre a necessidade desta consciência primária na solução de uma hierarquia entrelaçada. Conforme Goswami, esta hierarquia entrelaçada surge no colapso das ondas quânticas, processo que ele acredita ser necessário para formação da consciência humana.

Aborda a seguir o tema proposto no título deste trabalho que constitui sua hipótese de que o colapso das ondas quânticas seja causado pelas Ressonâncias de Poincaré. Apresenta e discute aspectos justificativos e decorrentes desta hipótese, mostrando a similaridade entre o comportamento destas ressonâncias com o das sinapses que ocorrem entre os neurônios no cérebro humano. Apresenta também uma tentativa para resolver o impasse da coexistência de uma consciência, suposta imaterial, com a matéria em um mesmo reino sendo descartado o dualismo, uma filosofia pouco aceita pela comunidade científica.

Finalmente expressa seu desejo de que a ponte surgida entre os seres biológicos com o universo sendo reconhecida, possa causar impacto nas pessoas que veriam que não são separadas do mundo, mas que são o mundo, que são parte do universo.

Palavras chaves: *ressonância, colapso, ondas, consciência.*

Abstract- He comments briefly on having shown in previous works that the factors that make possible the formation of a biological consciousness would also serve for the formation of a primary universal consciousness, including a hypothesis by Amit Goswami of the need for this primary consciousness in the solution of an intertwined hierarchy. According to his opinion, this intertwined hierarchy would appear in the collapse of quantum waves, a process that is necessary for the formation of human consciousness.

Next, he addresses the theme proposed in the title of this work, which constitutes his hypothesis that the collapse of quantum waves is caused by Poincaré Resonances. It presents and discusses aspects that justify and result from this hypothesis, showing the similarity between the behavior of these resonances and that of the synapses that occur between neurons in the human brain. It also presents an attempt to resolve the impasse of the coexistence of a conscience, supposedly immaterial, with matter in the same realm being discarded the dualism, a philosophy little accepted by the scientific community.

Finally, he expressed his wish that the bridge that emerged between biological beings and the universe, being recognized, could impact people who would see that they are not separate from the world but that they are the world, that they are part of the universe.

Keywords: *resonance, collapse, waves, consciousness.*

I. Introdução

Já foram discutidos em trabalhos anteriores (1,2,3), mecanismos e tópicos diversos considerados relevantes para a formação da consciência humana, realçando-se sempre a possibilidade de também serem relevantes na formação de uma possível consciência não biológica universal e primária que, existindo em todos seres biológicos, seria um elo entre estes e o universo.

Author: *Doctor of Philosophy in Metallurgy, The University of Utah – Prof. Aposentado da UFMG, Av. Uruguai, 1131 – Apto. 701 – Sion – Belo Horizonte – MG. e-mail: pereiraefsoares@yahoo.com.br*

Deve ser também considerada a intuição de místicos de várias filosofias que apregoam a existência de uma consciência universal.

Esta consciência evoluiria com a complexidade da estrutura que a comporta, expandindo-se e subdividindo-se pela incorporação das experiências vividas por cada ser, sendo tanto maior quanto maior for a complexidade desta estrutura.

Segundo Amit Goswami (4), o colapso das ondas quânticas parece ser um processo fundamental na formação da consciência e para ter-se este colapso tem-se que ter o término do processo de mensuração e para se ter este término é necessário ter-se o colapso das ondas quânticas. Isto constitui o que ele define como um processo de hierarquia entrelaçada, processo este que só poderia ser resolvido se visto de fora do sistema sendo considerado. Uma consciência primária seria então necessária para a solução do impasse surgido com a hierarquia entrelaçada no processo de formação da consciência humana.

O objetivo deste trabalho é mostrar o possível papel das Ressonâncias de Poincaré no colapso das ondas quânticas e sua influência na formação da consciência.

II. Desenvolvimento E Conclusões

Pensando-se em termos dos fundamentos da física quântica, este colapso da função de ondas ainda é uma lacuna a ser preenchida, não se sabendo ainda, na opinião do Professor Kokubum (5), como ou porque ocorre.

O autor deste trabalho formula a hipótese de que o processo do colapso das ondas quânticas seja causado pelas Ressonâncias de Poincaré, que ocasionariam a perda da coerência das suas superposições, resultando destes processos a materialização da imagem de um determinado "mapa" similar ao mapa neural formado provavelmente com a intervenção das sinapses entre neurônios no cérebro humano.

Como se sabe, estas ressonâncias podem criar, destruir ou propagar correlações (informações?) de partículas, causando divergências nos pontos onde ocorrem que, também como se sabe, constituem fenômenos não locais somente produzidos por sistemas de ondas persistentes. Ocorrem Ressonâncias de Poincaré nos pontos de interferência de duas ondas quânticas toda vez que a relação de suas freqüências seja um número inteiro, sendo este um processo quântico independente de qualquer observador e ocorrendo aleatoriamente (6).

O autor acredita que este colapso devido às Ressonâncias de Poincaré seja um processo similar ao que ocorre nas sinapses entre neurônios no cérebro humano. Ocorreriam reduções das funções de ondas formando quadros (imagens) consecutivos em intervalos de tempo devido ao fluxo de ondas persistentes, ou seja, um fluxo de ondas contínuo. Acredita também que este processo estaria relacionado com a formação da consciência universal primária do cosmos. O "como" sendo em parte respondido pelas Ressonâncias de Poincaré e o "porque", pela definição após o colapso, de uma situação que poderia ser memorizada e de certa forma sentida. Seria a definição de um dos possíveis estados superpostos que, aliado ao apregoado pelo conceito das informações relativas relevantes, forneceriam condições para formação de uma consciência universal, um processo similar ao que ocorreria na extensão da consciência humana.

Pode-se imaginar a Ressonância de Poincaré ocorrendo numa fronteira entre o intangível das ondas quânticas e o quadro materializado após o colapso das mesmas. Poderia talvez o mesmo processo até funcionar como uma fronteira entre a mente e a matéria quando e se houver criação de matéria nos pontos onde ocorrem as Ressonâncias de Poincaré.

O quadro materializado não necessariamente teria que ser formado por partículas materiais, mas também por formas imateriais, formadas nos pontos de interferência das ondas quânticas.

É bastante intrigante uma citação de Albert Einstein (7): "A mente humana tem que primeiro construir formas, independentemente, antes de poder encontrá-las nas coisas".

A teoria de Ghirardi-Rimini-Weber ou GRW (8), defende a superposição de partículas microscópicas, ou seja, que possam existir em múltiplos estados ao mesmo tempo e também que o colapso para um estado definido possa ocorrer espontaneamente e não só a partir de uma dada mensuração. De acordo com esta teoria, o colapso aconteceria de forma aleatória e com uma probabilidade fixa por partícula em uma unidade de tempo.

A comunicação não local que ocorre numa Ressonância de Poincaré daria também suporte para a existência de uma consciência universal que controlaria e gerenciaria todo o universo nos moldes da consciência

humana, que controla e gerencia todo o corpo, considerando que esta comunicação seria instantânea e não limitada no espaço.

Existindo esta consciência universal, talvez a mesma tenha servido como modelo para o processo de expansão da consciência humana assim como o modelo genético dos átomos, proposto pelo autor em trabalho anterior (9) tenha também servido de modelo para o código genético do DNA humano, sendo um elo primordial da biologia com a física quântica.

De modo similar ao da extensão da consciência humana para incorporar toda experiência captada pelos órgãos sensoriais, supõe-se ter sido formada a consciência universal primária nos primórdios dos tempos. Esta consciência universal primária assim formada consolidaria todo conhecimento existente num código de "DNA" não-biológico, cuja existência é uma hipótese formulada pelo autor (3).

Os seres biológicos, fundamentalmente formados por proteínas produzidas pelo DNA biológico, possuem em si mesmos a consciência (informação?) primária contida em seus átomos constituintes. Esta consciência primária seria expandida no processo de integração das experiências sensoriais individuais dos seres biológicos de acordo com a complexidade dos mesmos.

Na extensão e diferenciação da consciência humana tudo se passa como se a consciência primária se subdividisse nas várias consciências individuais com seus respectivos "selfs" característicos para cada ser humano. Esta diferenciação pela extensão individualizada da consciência, responderia à questão formulada por Alan Wolf em sua Introdução no livro de Amit Goswami (4) de como uma única consciência parece ser tantas consciências separadas.

Formula-se a seguir uma tentativa para explicar como uma imagem resultante de um colapso das ondas quânticas possa emergir como um pensamento (ondas quânticas?).

Esta tentativa pode ser formulada supondo-se que, nos cérebros, as ondas colapsadas formem pelas sinapses entre neurônios os mapas neurais que, após sua leitura holográfica, dêem origem a imagens na mente que seria formada pelas ondas quânticas que continuariam a fluir contendo incorporadas as informações resultantes do colapso das mesmas. Chama-se de consciência a este fluxo de informações (pensamentos?) sempre acrescido pelas imagens continuamente captadas, colapsadas e integradas.

Não é fácil explicar-se de um modo coerente a coexistência de uma consciência suposta imaterial com a matéria em um mesmo reino, hipótese decorrente quando se descarta a filosofia do dualismo, uma filosofia pouco aceita pela grande maioria dos cientistas contemporâneos. O autor acredita que esta dificuldade advém da falta de um conhecimento mais profundo da física quântica.

Resultados de pesquisas recentes feitas com o telescópio de raios gama INTEGRAL da Agência Espacial Européia (10) mostraram a existência de partículas com tamanhos da ordem de 10 exp-48 metros, menores ainda do que o tamanho de Plank que é da ordem de 10 exp -33 metros, sendo este, o suposto tamanho dos grãos do espaço proposto pela Teoria da Gravidade Quântica.

Sendo comprovada a existência de partículas com tamanhos desta ordem de grandeza e supondo-se o envolvimento das mesmas neste processo da coexistência de uma consciência imaterial com a matéria, ficaria mais aceitável sua coexistência, praticamente imaterial, com a matéria e isto sem necessidade de aceitação da filosofia do dualismo.

Talvez as partículas se comportem como ondas "imateriais" até a ocorrência do colapso quando então se "materializariam" tornando-se observáveis e sujeitando-se assim a algum processo de crescimento gerando o macro universo onde vivemos. Pensando nestes termos, fica diminuída a distância entre o espírito e a matéria.

A criação de uma ponte entre os seres biológicos com o universo devido ter sido o código do DNA copiado de um Modelo Genético do Átomo, deverá causar, se for reconhecida pela comunidade física, um enorme impacto nas pessoas que veriam sem qualquer margem de dúvida que não são separadas do mundo, mas que são o mundo e que são parte do universo.

References Références Referencias

1. Pereira, Elcio Fabio Soares. "Cosmos-Vida-Consciência II". Brazilian Journal of Development, v.7,n.10, p.99440-99445, 2021.
2. Pereira, Elcio Fabio Soares. "Cosmos-Vida-Consciência III". Brazilian Journal of Development, v.8, n.5,p. 35488-35497, 2022.
3. Pereira, Elcio Fabio Soares. "Cosmos-life-consciousness IV". Development and its Applications in Scientific Knowledge, DOI: 10.56238/sevedi76016v22023-086, 2023.
4. Goswami, Amit. "O universo autoconsciente". Tradução de Ruy Jungmann. Editora Aleph, 2007.
5. Kokubun, Fernando. https://www.fisicaseteemeia.com.br/2021.

6. Prigogine, Ilya. “O Fim das Certezas: tempo, caos e as leis da natureza. Tradução de Roberto Leal Ferreira. São Paulo: Editora UNESP, 2011.
7. Einstein, Albert. Apud “O Colapso da função de Onda. Temos o poder da manifestação?”, https://pt.linkedin.com/pulse/o-colapso-dafun%C3%A7%C3%A3o-selva-salerno.
8. SmithsonianMagazine,https://olhardigital.com.br/2020/02/06/notícias/novo-experimento-pode-resolver-o-maior-mistério-da-mecânicaquântica.
9. Pereira, Elcio Fabio Soares. “Development of a Model for Prediction of Composition and the Atomic Weights of the Elements”. Global Journal of Medical Research (K), Volume XXII, Issue 3, Version 1.0, 2022.
10. P. Laurent et al.”Constraints on Lorentz Invariance Violation using INTEGRAL/IBIS observations of GRB041219A”.Physical Review D, Vol.83, 121301 (R), June/28/2011. DOI: 10.1103/PhysRev D.83.121301.

Global Journal of Science Frontier Research: a Physics and Space Science
Volume 23 Issue 3 Version 1.0 Year 2023
Type: Double Blind Peer Reviewed Interenational Research Journal
Publisher: Global Journals
Online ISSN: 2249-4626 & Print ISSN: 0975-5896

The Characters and Mechanism Research of Hydrogen Absorption/Desorption Kinetics for Alloy Hydrogen Storage Materials

By Chuan-Zheng Yang
Shanghai University

Abstract- The characters of hydrogen absorption/ desorption kinetics for alloy hydrogen storage materials have been summarized. For searching the nature of hydrogen absorption/desorption kinetics, the experimental research results of evolution of the phase structure during hydrogen absorption/desorption processes have been summarized. It is found that hydrogen storage host is hydride for Mg system alloys and is hydrogenation solid solution for Ti and rare-earth systems. The situation of atom close packing and the number of interstitial sites as well as size of interstitial space of hydrogen storage materials were compared. The crystallographic behaviors in hydrogen absorption/ desorption processes have been expounded. The characters of hydrogen storage kinetics for alloy hydrogen storage materials were qualitatively explained from the thermodynamics of crystallographic behaviors. Under appropriate hydrogen pressure and different temperature, characters of hydrogen absorption kinetics curves are:

(1) The hydrogen absorption rate of initial stage and saturation quantity of hydrogen absorption increase with temperature increase for the materials (Mg system) that the host of hydrogen absorption is the hydride;
(2) The hydrogen absorption rate of initial stage and saturation quantity of hydrogen absorption decrease with temperature increase for the materials (Ti and rare-earth systems) that the host of hydrogen absorption is the hydrogenation solid solution.

Keywords: alloy hydrogen storage material, character of hydrogen storage kinetics, character of crystal structure for hydrogen storage material, mechanism of hydrogen absorption/desorption, hydride, hydrogenation solid solution.

GJSFR-A Classification: LCC: QD502.5.M6

The Characters and Mechanism Research of Hydrogen Absorption/Desorption Kinetics for Alloy Hydrogen Storage Materials

Chuan-Zheng Yang

Abstract- The characters of hydrogen absorption/ desorption kinetics for alloy hydrogen storage materials have been summarized. For searching the nature of hydrogen absorption/desorption kinetics, the experimental research results of evolution of the phase structure during hydrogen absorption/desorption processes have been summarized. It is found that hydrogen storage host is hydride for Mg system alloys and is hydrogenation solid solution for Ti and rare-earth systems. The situation of atom close packing and the number of interstitial sites as well as size of interstitial space of hydrogen storage materials were compared. The crystallographic behaviors in hydrogen absorption/ desorption processes have been expounded. The characters of hydrogen storage kinetics for alloy hydrogen storage materials were qualitatively explained from the thermodynamics of crystallographic behaviors. Under appropriate hydrogen pressure and different temperature, characters of hydrogen absorption kinetics curves are:

(1) The hydrogen absorption rate of initial stage and saturation quantity of hydrogen absorption increase with temperature increase for the materials (Mg system) that the host of hydrogen absorption is the hydride;
(2) The hydrogen absorption rate of initial stage and saturation quantity of hydrogen absorption decrease with temperature increase for the materials (Ti and rare-earth systems) that the host of hydrogen absorption is the hydrogenation solid solution.

Keywords: alloy hydrogen storage material, character of hydrogen storage kinetics, character of crystal structure for hydrogen storage material, mechanism of hydrogen absorption/desorption, hydride, hydrogenation solid solution.

I. Introduction

Alloy is a general term for metal materials composed of binary (multi) metals. There are mainly four important series of alloy hydrogen storage materials [1]: (1) AB type alloys, represented by TiFe and Ti ($Fe_{1-x}Mn_x$); (2) AB_2 Laves phase hydrogen storage alloys with three structures, cubic C15 type, such as $MgZn_2$; hexagonal C14 type, such as $MgCu_2$; hexagonal 36 type, such as $MgNi_2$ series alloys; (3) AB_5-type rare earth alloys, such as $LaNi_5$, M_mNi_5 (M_m is mixed rare earth metal), $LaNi_4Cu$, etc., and other AB_5 alloys of partial extraction Ni by other elements, etc; (4) Mg-based hydrogen storage alloys, such as $Mg88Y_{12}$, Mg-Cu, etc., and alloys that adds a small amount of other elements.

In addition to alloy hydrogen storage materials, there are metal coordination hydride hydrogen storage materials, such as $LiBH_4$, $NaBH_4$ and $NaAlH_4$, carbon fiber carbon nanotubes, non-carbon nanotubes, glass hydrogen storage microspheres, complex hydrogen storage materials and organic liquid hydrides, and so on. This paper focuses on the first four kinds of important alloy hydrogen storage materials.

The hydrogen storage properties of materials are characterized in many aspects [3], but the commonly used criteria for measuring the performance of hydrogen storage materials are: (1) volumetric hydrogen storage density, that is, the mass of hydrogen storage per unit volume of the system (kg/m3), and (2) mass hydrogen storage density, that is, the ratio of hydrogen storage mass of the system to the mass of the system (%). The hydrogen storage density data of the main materials in the previous three important series of the above four hydrogen storage materials are given in tables 1 and 2.

Author: Chuan-Zheng Yang, male, born in 1939, Professor, Department of Physics, Shanghai University, Shanghai 200244, China.
e-mail: yangcz1939@163.com
Research Interests: material Physics and Modern Test and Analysis of Materials.

Table 1: Bulk density and mass density of different hydrogen storage materials [1]

System name	gaseous H	liquid H	MgH_2	TiH_2	$TiFeH_{1.95}$	$LaNi_5H_{6.7}$
Volume density/cm^3	5.4×10^{19}	4.2×10^{22}	6.6×10^{22}	9.1×10^{22}	5.7×10^{22}	7.6×10^{22}
Mass density /%	100	5.4	7.66	4.04	1.84	1.58

Table 2: Mass and volume of materials required to store the same amount of (7m3) hydrogen [1]

System name	gaseous H	liquid H	MgH_2	TiH_2	$TiFeH_{1.95}$	LaNi5$H_{6.7}$
Quality/kg	0.6	0.6	8	16	34	41
Volume/L	7000	9	5.5	4.2	6.6	4.8

It can be seen from tables 1 and 2 that the hydrogen storage density of alloy hydride is 1000 times that of gaseous hydrogen (in standard state), that is, the hydrogen storage capacity of some metal materials (such as TiH2, etc.) is only half of that of liquid hydrogen storage.

From the point of view of application, not only the hydrogen absorption capacity of the material is required, but also the speed of hydrogen absorption, the speed of hydrogen desorption, the stability of hydrogen storage, the cycle performance of hydrogen absorption and desorption, as well as cost and economic benefits should be considered. In terms of basic research on the development and application of new materials, in addition to the indicators required from the application point of view, the kinetic characteristics and thermodynamic analysis of hydrogen absorption and desorption of materials are also very necessary, and it is necessary to further explore the root causes and mechanisms that affect the kinetic properties.

As we all know, "in the field of philosophy, matter determines consciousness; in the field of natural science, structure determines function." The hydrogen storage performance of alloy hydrogen storage materials is determined by the structure of alloy hydrogen storage materials.

In order to explore the hydrogen absorption and desorption mechanism of hydrogen storage materials, it is necessary to observe and study the evolution of crystal structure and microstructure of hydrogen storage materials in the process of hydrogen absorption and desorption by on-line (in situ) or quasi-dynamic real-time observation while measuring hydrogen absorption and desorption kinetic curves. Therefore, this paper summarizes the law of hydrogen absorption and desorption kinetics of four kinds of alloy hydrogen storage materials (Section 2) and the evolution of parent phase structure of hydrogen storage materials in the process of hydrogen absorption and desorption (Section 3). Through the study of the crystal structure characteristics of four kinds of alloy hydrogen storage materials and their relationship with the main body of hydrogen storage (hydride) (Section 4), the diffusion behavior and thermodynamics of hydrogen atoms in the materials are analyzed comparatively, in order to explore the hydrogen absorption and desorption mechanism of alloy hydrogen storage materials.

II. Dynamic Characteristics of Hydrogen Absorption of Typical Alloy Hydrogen Storage Materials

The method to study the kinetic characteristics of hydrogen absorption and desorption is to determine the relative amount and time of non-stop hydrogen absorption of hydrogen storage materials at a given pressure.

System curve, that is, the P-C-T curve of the relative amount of hydrogen absorbed (or released) with time at different temperatures at a given hydrogen pressure, and the curve of the relative amount of hydrogen absorbed (or released) with time at different hydrogen pressures (T-C-T) at a given temperature.

a) *Dynamic characteristics of hydrogen absorption of AB-type Ti hydrogen storage materials*

Lee, Byun and Park [4] have studied the hydrogenation kinetics of TiFe and its alloys. Figure 1 shows the plot of the hydrogenation reaction fraction F/T of TiFe at several constant pressures. it can be seen that F varies linearly with time at the beginning, which indicates that the reaction rate is constant. The slope of the straight line, that is, the reaction rate decreases gradually with the reaction process. The above phenomena show that the total reaction rate has multiple cascade control, that is, the rate control cascade varies with the reaction process.

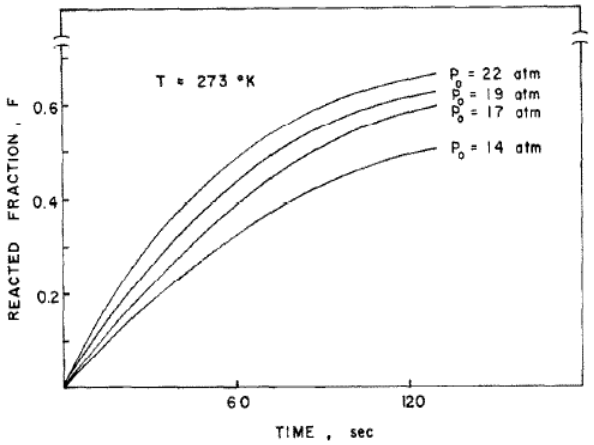

Fig. 1: Hydrogenation kinetics curve of TiFe at 273k and several hydrogen pressures [4]

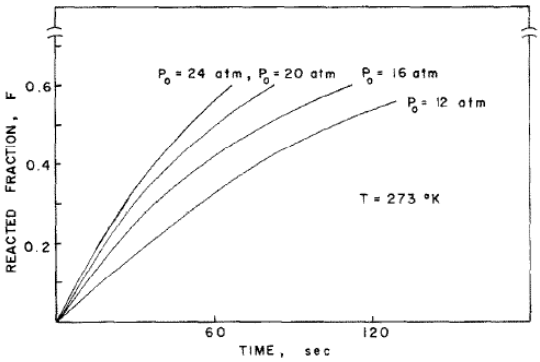

Fig. 2: TiFe0.8Mn0.2 kinetic curve at 273k and several hydrogen pressures [4]

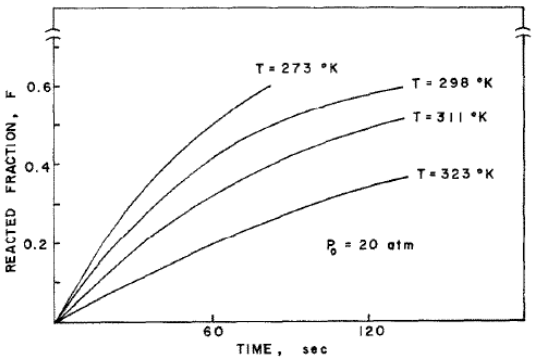

Fig. 3: Hydrogenation kinetics curve of hydrogen absorption of $TiFe_{0.8}$ $Mn_{0.2}$ at constant pressure and different temperature [4]

Figure 2 shows the diagram of the hydrogenation reaction fraction of TiFe0.8Mn0.2 at several constant pressures, which shows a behavior similar to that of TiFe. After analysis, the dynamic behavior of TiFe accords with the following two equations:

$$F = 3.5\times10^{-2}\frac{P_0 - P_{eq}}{T^{1/2}}\exp\left(-\frac{800cal/mol}{RT}\right)t \qquad F<0.25 \tag{1}$$

$$\left(1-F^*\right)^{1/3} - \left(1-F\right)^{1/3} = 5.6\times10^{-3}\exp\left[-\frac{1000cal/(mol\ H)}{RT}\right](P_0^{1/2} - P_{eq}^{1/2})(t-t^*) \tag{2}$$

The dynamic behavior of TiFe0.8Mn0.2 accords with the following two equations：

$$F = 5.0\times10^{-2}\frac{P_0 - P_{eq}}{T^{1/2}}\exp\left(-\frac{1000cal/mol}{RT}\right)t \qquad F<0.2 \tag{3}$$

$$\left(1-F^*\right)^{1/3} - \left(1-F\right)^{1/3} = 9.0\times10^{-3}\exp\left[-\frac{1500cal/(mol\ H)}{RT}\right](P_0^{1/2} - P_{eq}^{1/2})(t-t^*) \tag{4}$$

When the above four reaction rate equations are carefully evaluated, the time relationship of the reaction rate can be understood. If at constant pressure P0, the temperature increases, including the exponential term of the activation energy term increases, but the equilibrium pressure P_{eq} or driving force term decreases. As mentioned above, the activation energy is relatively small and varies sharply with temperature at constant pressure P_{eq}, and the reaction rate decreases with the increase of temperature (see figure 3). Because the driving force term is not considered in this system, the activation energy will be negative. In fact, Stakebake [5]

has reported the negative activation energy in U hydrogenation.

Wajiad et al. [6] measured the hydrogen absorption kinetics curve (hydrogen concentration time) of hydrogen storage Ti-Fe-Mn alloy partially replaced by Cu and Y under different hydrogen pressure (Fig.4 (a)) and constant pressure 2.7MPa (10°C, 30°C and 45°C), as shown in figure 4 (b). Figure 4 shows that the initial hydrogen absorption activity of pure samples is fast when exposed to hydrogen atmosphere; the hydrogen absorption capacity increases with the increase of pressure at the same temperature; at the same pressure, the hydrogen absorption capacity decreases with the increase of temperature. The maximum hydrogen absorption capacity was 1.67wt%, 1.41wt% and 1.32wt%, respectively, for 10°C

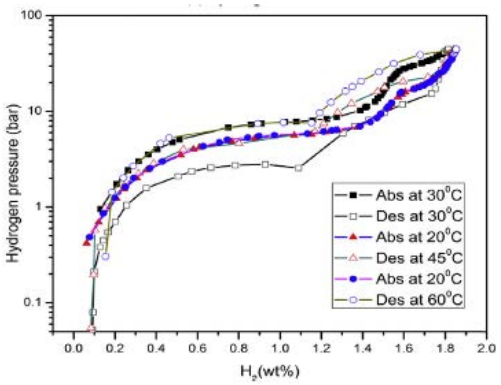

(a)

Fig.4 (a): The curve of hydrogen absorption and desorption parameters of Ti-Fe-Mn alloy replaced by Cu and Y in 20oC~60°C range [6]

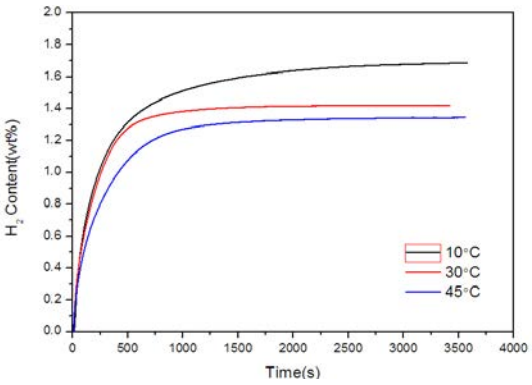

(b)

Fig. 4 (b): Kinetic curves of Ti-Fe-Mn alloy replaced by Cu and Y at 10°C, 30°C and 40°C respectively under 2.7MPa pressure [6]

750s, 30°C 250s and 45°C350s, respectively. The incubation period of hydrogen absorption is obviously short, and the dissolution reaction time reaching the saturation point is less than a few minutes. 10°C reached a higher capacity, on the contrary, the hydrogen absorption function was relatively low in 45°C, while the reaction rate was the fastest in 30°C, reaching the equilibrium point very quickly.

b) Kinetic characteristics of hydrogen absorption and desorption of Laves phase TiCr2 hydrogen storage materials

According to the binary phase diagram of Ti-Cr, $TiCr_2$ has a certain composition range and belongs to hexagonal C14 structure at high temperature, $TiCr_2$ at low temperature (<800°C), cubic C15 structure, and TiCr2 at middle temperature, which is a mixture of C14 and C15. Figure 5 shows the XRD diagram of the melted alloy at different times of ball milling. It can be seen that the newly cast alloy is a mixture of C14 and C15. It changes to BCC cubic structure after different time of ball milling, and all of them are meta-BCC after 5 hours of ball milling.

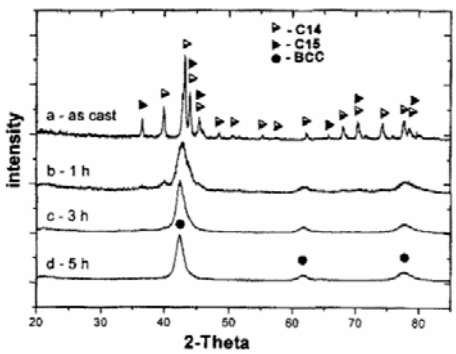

Fig. 5: XRD diagram of smelting alloy at different times of ball milling [8]

Huang Taizhong [8] in order to investigate the effect of different Cr/Ti ratios on the hydrogen absorption and desorption properties of alloys, alloys with different Cr/Ti ratios were designed and P-C-T tests were carried out. The P-C-T curves of each alloy at different temperatures show that with the increase of test temperature, the hydrogen absorption capacity of the alloy decreases and the hysteresis between hydrogen absorption and desorption weakens. At 273k, the hysteresis effect of the alloy increases with the increase

of Cr/Ti, but the hysteresis effect of each alloy is still very low. According to the P-C-T test results of each alloy, the maximum hydrogen absorption capacity and reversible hydrogen absorption capacity of each alloy at different temperatures can be obtained. The results are listed in Table 3. It can be seen from the table that both the reversible hydrogen absorption capacity and the maximum hydrogen absorption capacity of the alloy decrease with the increase of temperature, and the hydrogen absorption capacity of $TiCr_{1.8}$ is the highest at 273k, but decreases rapidly with the increase of temperature.

Table 3: Maximum and reversible hydrogen absorption capacity of TiCrx alloys with different composition at different temperatures [8]

The x value of $TiCr_x$	Maximum hydrogen absorption and hydrogen content of alloy(wt%)				Reversible hydrogen absorption of alloys(wt%)			
	Test temperature (°K)				Test temperature (°K)			
	273	303	333	353	273	303	333	353
1.6	1.415	1.102	0.955	0.857	0.945	0.636	0.548	0.522
1.80	1.449	1.005	0.881	0.811	0.979	0.606	0.534	0.504
1.85	0.341	1.028	0.855	0.811	0.889	0.633	0.524	0.492
1.90	1.295	0.943	0.819	0.755	0.858	0.563	0.493	0.455
2.00	1.281	0.891	0.762	0.721	0.867	0.525	0.466	0.455
2.20	1.180	0.876	0.755	0.690	0.770	0.537	0.464	0.443

The P-C-T test results of $TiCr_{1.8-x}Mo_x$ (x=0.2, 0.4, 0.6, 0.8, 1.0, 1.2) alloy by Huang Taizhong et al [8] also showed the above rule, that is, the hydrogen absorption capacity of the alloy decreased with the increase of test temperature.

c) *Kinetic characteristics of hydrogen absorption of AB5 rare Earth hydrogen absorption Materials*

i. *Kinetic characteristics of LaNi5 hydrogen absorption process [9]*

Lu Manqi, Qi Zhenzhong and Wu Pingsen [9] reported the kinetic curve of hydrogen absorption by LaNi5. Figure 6 shows the curve of hydrogen absorption with time when absorbing hydrogen at different temperatures under the same initial pressure. Figure 7 shows the relationship between hydrogen absorption capacity and time at the same hydrogen absorption temperature and different initial pressure. Obviously, on the diagram, each curve consists of two straight lines with different slopes. The straight line corresponding to the part with high hydrogen absorption capacity has a smaller slope. With the increase of temperature or the decrease of initial pressure, the slope difference between the two parts of each curve is so small that it is very close.

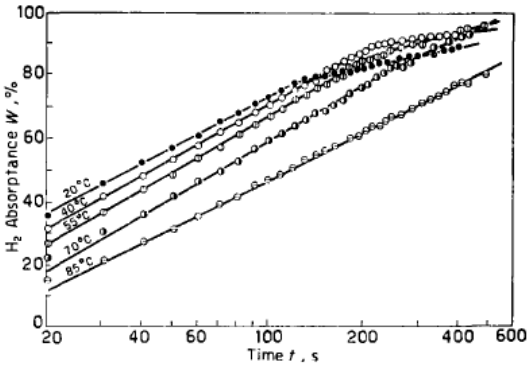

Fig. 6: The initial pressure is 30.7atm and the hydrogen absorption capacity of LaNi5 varies with time at different temperatures [9]

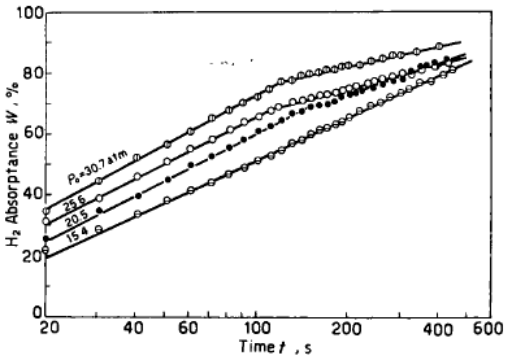

Fig. 7: Variation of hydrogen uptake of LaNi5 with time at different initial pressure [9]

In addition, the hydrogen absorption rate changes when the initial pressure decreases or the hydrogen absorption temperature changes. First discuss the first part of the line on the diagram, according to the above results, it can be expressed by the following formula:

$$W = A(T, P_0)\log t + B \quad (5)$$

Among them, A, B has nothing to do with time, T is the hydrogen absorption temperature, P_0 is the initial pressure, and the hydrogen absorption rate is obtained by time differential.

$$dW/dt = A(T, P_0)/t \quad (6)$$

That is, there is a linear relationship between the hydrogen absorption rate and the reciprocal of time. The hydrogen absorption reaction of $LaNi_5$ is:

$$LaNi_5+3H_2 \rightarrow LaNi_5H_6.$$

The hydride formation process must include the following steps: the decomposition of hydrogen into hydrogen atoms on the metal surface, that is, the surface reaction; the diffusion of hydrogen atoms into the metal; and the phase transition from intermetallic compounds to their hydrides. In this way, the hydrogen absorption rate should be controlled by the slowest of the three processes, and they are all thermal activation processes. No matter which one controls the hydrogen absorption rate, A(T,P0) can be written:

$$A = A'(T, P_0)e^{-U/RT} \tag{7}$$

In the formula, U is the activation energy of process; R is gas constant. The T is absolute temperature of hydrogen absorption, A should also include factors related to the driving force, because when the initial pressure or temperature changes, the hydrogen absorption rate is also different. It can be seen from the P-C-T diagram, that there is a corresponding equilibrium pressure $P_{Average}$ at a certain hydrogen absorption temperature. Therefore, for a certain initial pressure P_0, the equilibrium pressure corresponding to T and T_0 is P_0, so T_0-T can be used as the driving force for hydrogen absorption.

$$A = A_0(T_0\text{-}T)\, e^{-U/RT} \tag{8}$$

A_0 is a constant. So the formula (5) becomes:

$$W = A_0(T_0 - T)e^{-U/RT} \log t + B \tag{9}$$

Because when $T=T_0$ does not actually absorb hydrogen, it deduces B=0. According to the Van't-Hoff relation, there are

$$\ln P_{平} = \frac{\Delta H}{RT} - \frac{\Delta S}{R} \tag{10}$$

ΔH and ΔS are the changes of enthalpy and entropy during the formation of $LaNi_5H_6$ by $LaNi_5$, respectively. $P_{Average}$ is the equilibrium pressure corresponding to T, which can be obtained by$\ln P_{Average}$~1/T:

$$\begin{aligned} \Delta H &= -7.4 kcal/molH_2 \\ \Delta S &= -25.2 cal/^o C \cdot H \end{aligned} \tag{11}$$

Finally, the expression of hydrogen absorption rate is obtained:

$$\frac{dW}{dt} = A_0(T_0 - T)e^{-U/RT} \cdot \frac{1}{t} \tag{12}$$

The time t is in seconds, A_0=0.13, and the activation energy is 2.0 0.2kcal/molH2=8.346J±0.834J/molH2. The quantitative relationship between hydrogen absorption rate and initial pressure, temperature and time is established. When W is higher, it can also be approximated by

$$W = A_0^{'}(T_0 - T)e^{-U'/RT} \cdot \log t \tag{13}$$

U=3.2kcal/molH$_2$ =13.3824J/molH$_2$, $A_0^{'} = 0.97$。

ii. *Kinetic characteristics of hydrogen storage in LaNi5-xAlx [10d11]*

Figure 8 shows the hydrogen absorption P-C isothermal curve (P-C-T) of $LaNi_{4.25}Al_{0.75}$ alloy after initial activation at 333k, 353K, 373K and 423K, the hydrogen storage capacity of the alloy decreases systematically, and the hydrogen absorption plateau pressure increases obviously with the increase of temperature. The relation function between platform pressure (p_{eq}) and temperature is ln p_{eq}=-4820/T+12.46. At 353k is the molecular formula of saturated hydride $LaNi_{4.25}Al_{0.75}H_{4.2}$. Compared with $LaNi_5H_6$, the saturated hydrogen absorption capacity of $LaNi_{4.25}Al_{0.75}$ is reduced by nearly 30%, and the platform pressure is also significantly reduced.

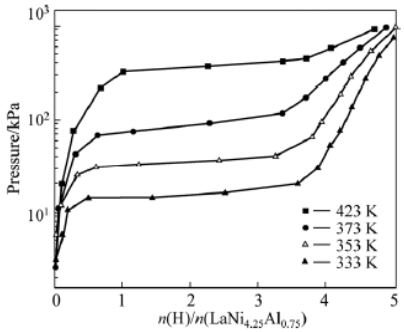

Fig. 8: PC isotherm curve of hydrogen absorption of LaNi4.25Al0.75 alloy at different initial activation temperatures.

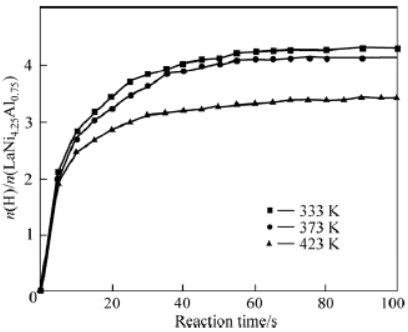

Fig. 9: Hydrogen absorption Kinetic Curve of LaNi4.25Al0.75 Alloy at different temperatures

The kinetic curve of hydrogen absorption of $LaNi_{4.25}Al_{0.75}$ alloy after 25 cycles of 1020kPa (initial pressure of hydrogen absorption vessel) is shown in figure 9. At 333k and 373K 60 seconds, one mole of $LaNi_{4.25}Al_{0.75}$ can absorb more than 4 moles of H_2, but only 3 moles of H_2 in 423K100 seconds. The hydrogen absorption rate decreases with the increase of temperature.

Zhang Ruijing, Lu Manqi and Cao Li studied the effect of x on hydrogen storage performance in $LaNi_{5-x}Al_x$ [12]. The pressure-composition isotherm (P-C-T) of $LaNi_{5-x}Al_x$ alloy at 333, 353, 373K shows that at the same temperature, the equilibrium pressure of the alloy decreases with the increase of Al content, and the platform length, namely hydrogen absorption capacity, decreases.

According to the above results, some people think that "the research results generally show that the saturated hydrogen absorption capacity of metal hydride hydrogen storage materials decreases with the increase of temperature under certain hydrogen pressure". What is the situation? is this the case for all alloy hydrogen storage materials? let's take a look at the experimental results below.

d) Kinetic characteristics of hydrogen absorption and desorption of Mg hydrogen storage alloys

i. *Hydrogen absorption-desorption kinetics of Mg88Y12 alloy [13]*

The hydrogen absorption and desorption kinetics curves of $Mg_{88}Y_{12}$ alloy obtained by Yang Yuan and Bu et al. [13] are shown in Fig. 10 (a) and (b), respectively. As can be seen from figure 10 (a), the sample with temperature ≥ 290°C shows a better kinetic curve, which is lower than 290°C, showing poor kinetic function, but it can still absorb 2.63wt% and 3.94wt% hydrogen within 60 minutes under 100°C and 150°C; the alloy shows good kinetics for hydrogen desorption at relatively high temperature, and the hydrogen energy under 380°C is completed within 10 minutes. But it is related to temperature and becomes very bad below 320°C. As shown in figure 10 (b), 290°C is completely hydrogenated for about 400min.

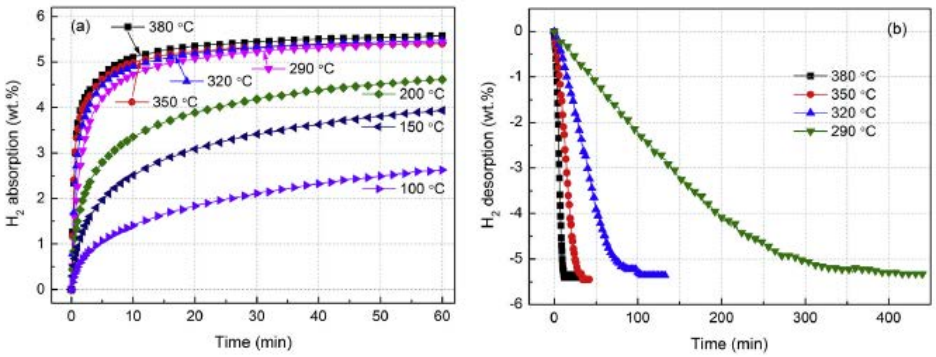

Fig. 10: Isothermal hydrogen absorption/desorption kinetics curve of Mg88Y12 alloy

(a) Absorbing hydrogen under 3MPa hydrogen pressure.

(b) Hydrogen desorption below 0.03MPa hydrogen pressure [13]

There are three models to describe the different kinetic stages of hydrogen absorption and desorption: (a) surface reaction model, (b) Johnson-Mehl-Avrami (JMA) model. (c) shrinking volume (CV). Yang gives the best results by fitting the hydrogen evolution curve with JAM model, which is used in the case of nucleation and growth during hydrogen absorption and desorption. The JMA equation is expressed as follows:

$$[-\ln(1-\alpha)]^{1/n} = kt \qquad (14)$$

Here, α is the reaction fraction, k is the rate constant and n is the reaction order. According to the fitting results, the n value of the hydrogen evolution reaction is taken as 3. Figure 11(a) shows that the hydrogen kinetics $[-\ln(1-\alpha]^{1/3}$ is plotted to t at different temperatures. It is clear that there is a good linear relationship between $[-\ln(1-\alpha]^{1/3}$ and reaction time. This shows that $Mg_{88}Y_{12}$ dehydrogenation follows a three-dimensional growth process controlled by the interface and nucleation at the same time.

In order to further understand the dehydrogenation kinetics of Mg88Y12 alloy, the activation energy E_{des} of hydrogen evolution was determined by Arrhenius equation.

$$\ln k = -\frac{E_{des}}{RT} + \ln k_0 \qquad (15)$$

Here, k is the kinetic rate constant of hydrogen evolution derived from the equation, E_{des} is the activation energy of the hydrogen evolution process, R is the gas constant, T is the absolute temperature, and k is the frequency factor. The Arrhenius of de-hydrogenation kinetics is shown in Fig. 11 (b), and the activation energy of hydrogen desorption is calculated to be

122kJ/mol. In addition, it is worth noting that the hydrogen absorption kinetic curve can not be well fitted by the above three models. As shown in figure 11(a), the hydrogenation rate is fast in the first few minutes, and then the hydrogenation rate is obviously slow, which can be explained as follows: in the initial hydrogen absorption process, the alloy quickly absorbs a lot of H_2 and forms a near-surface hydride layer, after which the hydrogenation rate will be very slow. The reason is that hydrogen diffuses very slowly in the hydride layer, which becomes the rate limiting factor in the subsequent hydrogenation process.

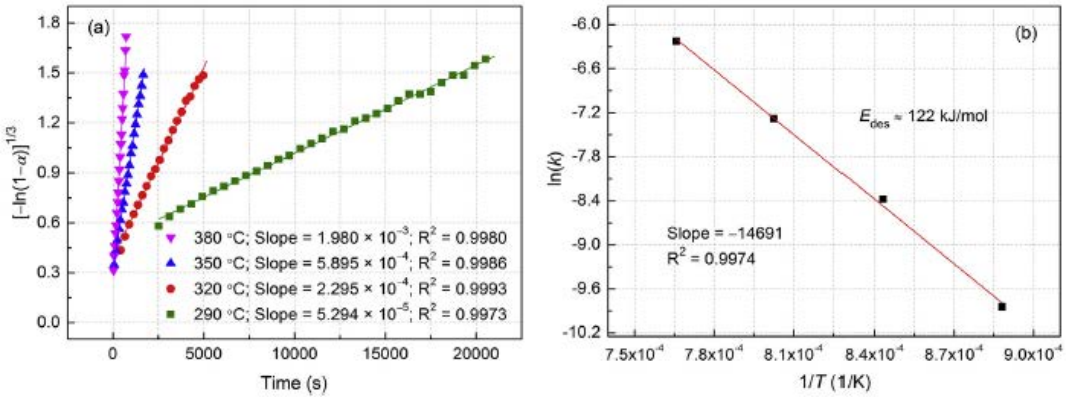

Fig. 11: (a) Drawing of hydrogen desorption kinetics $[-\ln(1-\alpha]^{1/3}$ to t of hydrogenated $Mg_{88}Y_{12}$ alloy at different temperatures. (b) Arrhenius drawing of de-hydrogenation kinetics [13]

ii. *Kinetic characteristics of hydrogen absorption and desorption of Mg-Cu alloy [14]*

Wu, Li and Zhang[14] reported that the kinetic curve of hydrogen absorption of undoped, Y-doped and Ni-doped Mg_2Cu alloy under 4Mpa pressure is shown in figure 12. it can be seen that the hydrogen absorption rate of undoped samples becomes faster when the hydrogenation temperature is increased to 300°C, and the full hydrogen absorption energy is completed in 5 minutes, as shown in figure 12 (a). For Y-doped and Ni-doped samples, the full hydrogen absorption is completed in 10 minutes and 300°C2 minutes, as shown in figure 12 (b). This means that both nanostructured Mg_2Cu alloy and YH_2/YH_3 embedded in Mg_2Cu matrix have good catalytic effect on Mg_2Cu disequilibrium reaction.

In order to understand the hydrogen evolution characteristics of undoped Mg_2Cu and Y-doped and Ni-doped samples, the isothermal dehydrogenation curve is needed, as shown in figure 13. It can be seen that the hydrogen de-absorption is slower than absorption at 300°C in kinetics. When the de-hydrogenation temperature increases to 350°C, Mg_2Cu and Y-doped and Ni samples are 0.99%

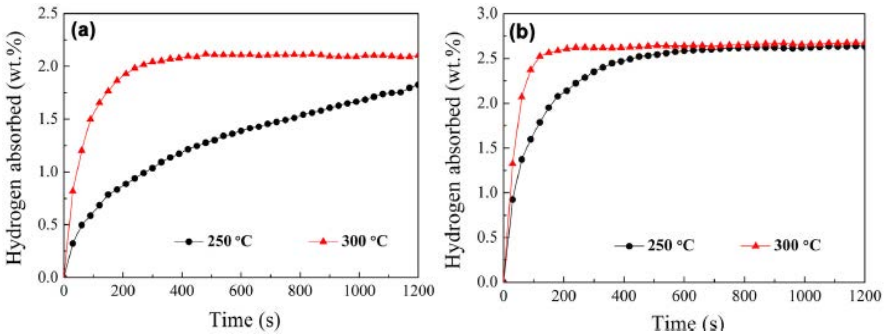

Fig. 12: Hydrogen storage and absorption time curve of Mg alloy [14],

(a) undoped Mg2Cu sample (b) Y, Ni doped sample

and 1.93% hydrogen respectively within 3 minutes, indicating that the Mg_2Cu samples doped with Y and Ni have better hydrogen desorption kinetics than the undoped samples. As mentioned above, $MgCu_2$ and MgH_2 exist together with Mg_2NiH_4, YH_2 and YH_3 in the hydrogenated, Y-doped and Ni-doped $MgCu_2$ samples, so the nanostructured Mg_2NiH_4 and YH_2/YH_3 also have catalytic effects on the reverse reaction.

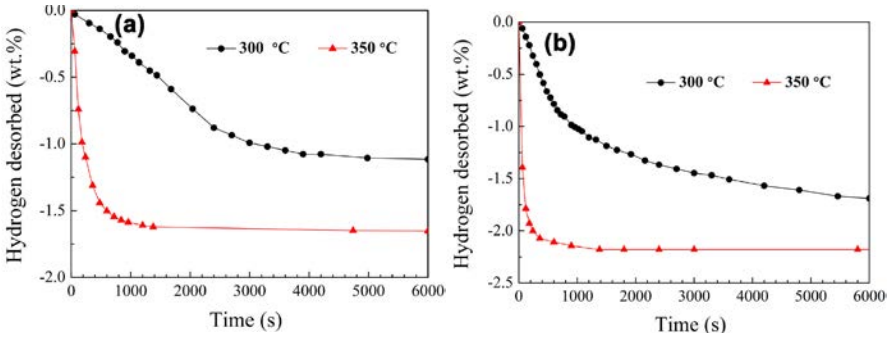

Fig. 13: Isothermal desorption hydrogenation curve of dehydrogenated materials [14], (a) unmixed Mg_2Cu samples, (b) Mg_2Cu samples doped with Y and Ni

iii. *Kinetic characteristics of hydrogen absorption and desorption of Mg hydrogen storage alloy catalyzed by 1 mol% Nb_2O_5 [15]*

Fig. 14 shows the hydrogen absorption curve of Mg hydrogen storage alloy catalyzed by 1 mol% Nb_2O_5 [15]. At lower hydrogen pressure (0.2Mpa), the initial hydrogen absorption rate and saturated hydrogen absorption capacity increase with the increase of temperature. However, when the hydrogen pressure is 1.0Mpa, the initial hydrogen absorption rate and hydrogen absorption capacity of 250°C are lower than that of 150°C (before 30 seconds), and when the hydrogen pressure is 3.0Mpa, there is a cross scenario. The initial hydrogen absorption rate (before 30 seconds) is lower than that of 150°C. The cross scenario occurs when the hydrogen pressure is in 3.0Mpa.

e) Summary

The contents of this section are summarized as follows:

1. At constant temperature and different hydrogen pressure, the initial hydrogen absorption rate increases with the increase of hydrogen pressure, and the hydrogen saturation increases with the increase of hydrogen pressure. The four types of alloy hydrogen storage materials all conform to this law, and the "initial hydrogen absorption rate" mentioned here is known from the slope of the initial kinetic curve.

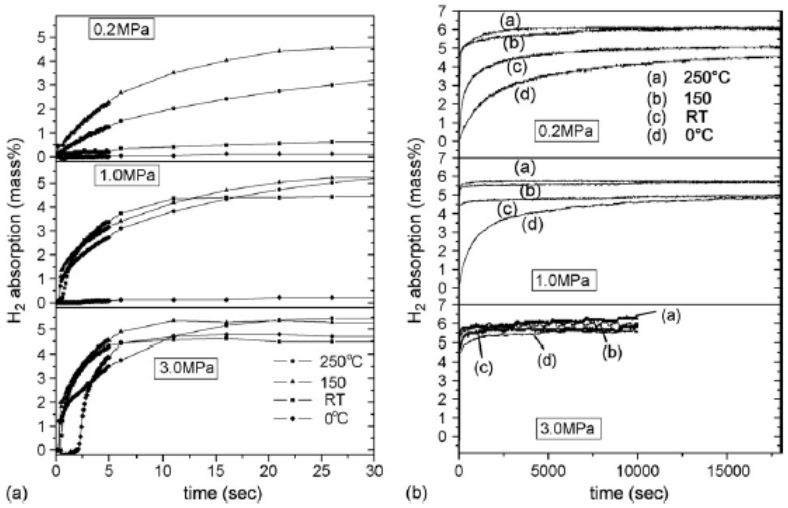

Fig. 14: Hydrogen absorption curve of Mg alloy catalyzed by Nb_2O_5 [15], at 0, 20, 150, 250°C and at 0.2, 1.0, 3.0MPa hydrogen pressure. (a) reaction time to 30 seconds; (b) 0.2 and 1.0Mpa reaction time to 18000 seconds; 3.0Mpa time to 10000 seconds

2. At constant hydrogen pressure and different temperature, there are two opposite situations of initial hydrogen absorption rate and hydrogen saturation with temperature: (i) the initial hydrogen absorption rate and hydrogen saturation decrease with the increase of temperature. AB-type TiFe, AB_2-Laves and AB_5-type rare earth hydrogen storage materials accord with this situation, but Mg hydrogen storage materials do not conform to this law. (ii) the initial hydrogen absorption rate and hydrogen saturation increase with the increase of temperature, Mg series hydrogen storage materials accord with this situation, but AB type TiFe system, AB2 type Laves phase and AB5 type rare earth series hydrogen storage materials do not.

The two opposing laws in point (2) seem to be very contradictory and difficult to understand, but these are experimental facts and cannot be questioned. This

may show the characteristics of two kinds of alloy hydrogen storage materials, which is the problem to be studied in this chapter.

III. Structural Evolution of Hydrogen Storage Materials During Hydrogen Absorption and Desorption

In the books and literature "hydrogen storage materials" [16], "Properties and applications of metal hydrides"[17] and "Hydrogen in Intermetallic Compounds" [18], it is often referred to as "metal hydride" hydrogen storage. Therefore, the products of metals and their alloys after hydrogen absorption are metal/alloy hydrogen compounds. Is it true that all alloy hydrogen absorbing materials are "hydrogen compounds" after absorbing hydrogen? It is worthy of experimental study and analysis. In order to study this problem, we must start with the crystal structure evolution of hydrogen storage materials in the process of hydrogen absorption and desorption.

In order to study the structural evolution of hydrogen storage materials in the process of hydrogen absorption and desorption, the key is to correctly identify and judge the intermediate products and final products in the process of hydrogen absorption and desorption.

For the convenience of the following discussion, two concepts of "metal hydride" and "alloy hydrogenated solid solution" are introduced. The crystal structure of the hydrogenated solid solution of the alloy is the same as that of the parent phase, which is not only the same space group, but also the same crystal structure. Because hydrogen is the first element in the periodic table, and the atomic radius is much smaller than that of the metal atom, the hydrogen atom may only occupy the interstitial position of the parent phase, forming an alloy interstitial solid solution, resulting in only a small change in the lattice parameters of the parent phase. and the change of lattice parameters is related to the concentration of hydrogen absorption and desorption. The structure of the hydride phase is different from that of the parent phase, because the hydrogen atom may not occupy the interstitial position, but occupy a certain crystallographic lattice position, and the diffraction pattern different from the parent phase should be given, so it is easier to determine whether it is a hydride or not.

If during the formation of the hydride phase, the hydrogen atom occupies the interstitial hole position of the original parent phase and forms the hydride, then the crystal structure of the hydride keeps the structure of the parent phase unchanged, which is called interstitial hydride, and its essence is hydrogenated solid solution.

The X-ray diffraction patterns of polycrystalline materials, like human fingerprints, can make a correct judgment of the phase. It is based on the standard data in the powder diffraction file (PDF) databasePCPDFwin of the International Center of diffraction data (ICDD)-[19]. Its method is introduced in detail in the relevant chapters of "Phase diffraction Analysis" [20] and "Ray diffraction and scattering Analysis of material"[21]. According to the methods introduced in Chapter 12 of this book: 1) search/match and judge the diffraction patterns of the analytical samples; 2) when the crystal structure data of each hydride phase (crystal system, space group, lattice parameters and the position and occupation probability of each atom in the cell) are known, the analytical patterns can be fitted by Reitveld full spectrum fitting-refinement. However, the key is the experimental means and methods of observation of alloy hydrogen storage materials in the process of hydrogen absorption and desorption. An on-line (in situ) diffraction device for laboratory X-ray source and synchrotron radiation X-ray has been developed both at home and abroad, which can make real-time dynamic observation and analysis of hydrogen storage materials in the process of hydrogen absorption and desorption. Another important problem is that it is better to have the participation of diffraction analysis experts.

a) Structural evolution of Ti alloys during hydrogen absorption and desorption [6]

Fig. 15(a) shows the XRD pattern of the newly synthesized Ti-Fe-Mn samples replaced by Cu and Y by Wajid Ali et al. From the diagram, it can be seen that the main diffraction peaks belong to the TiFe phase with CsCl ordered structure, but no other phases are found. The Rietveld analysis results are shown in figure 14(b) and listed in Table 4.

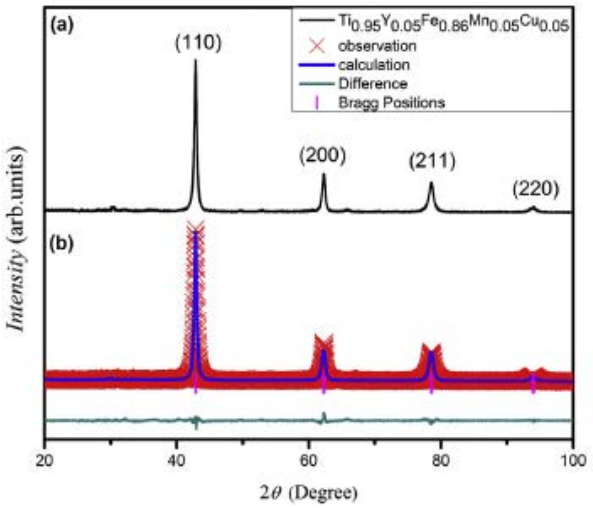

Fig. 15: (a) substituting Cu and Y for XRD patterns of synthetic Ti-Fe-Mn samples, (b) Rietveld refinement results [6]

Table 4: Analytical results of synthetic and hydrogenated Ti-Fe-Mn samples replaced by Cu and Y [6]

Samples	Structure type	Latticeparameter (nm)	Density. (g/cm^3)	Volume ($10^{-6}pm^{-3}$)
TiFe	CsCl-type	0.2976	6.53	30.40
Fresh casting Ti-Fe-Mnalloy	CsCltype	0.2983	6.89	30.54
After absorbing hydrogen	CsCl-type	0.2990	6.47	30.73

It can be seen from Fig. 15 and Table 4 that the crystal structure of the sample does not change, only the lattice parameters and cell volume increase, regardless of hydrogen absorption or desorption. This shows that the hydrogen absorption process is the formation of hydrogenated solid solution TiFe-H_n, and the hydrogen desorption process is the decomposition of hydrogenated solid solution TiFe-H_n. It is believed that the hydrogenation behavior of TiFe alloy has undergone a process from $TiFe_5$ (cubic crystal) to $TiFeH_{1.04}$ (tetragonal intermediate hydride phase) and then to $TiFeH_{1.95}$ (cubic crystal, saturated hydride phase). However, the diffraction cards of the two phases can not be found in the PCPDFwin database, maybe the $TiFeH_{1.04}$ and $TiFeH_{1.95}$ are hydrogenated solid solutions TiFe-$H_{1.04}$ and TiFe-$H_{1.95}$.

b) *Structural evolution of Laves phase $TiCr_2$ hydrogen storage alloy during hydrogen absorption and desorption*

In order to further study the hydrogen absorption nature of $TiCr_2$ Laves phase BCC phase, the XRD patterns of samples before and after hydrogen absorption and desorption are shown in figure 16. From figure 16, it can be seen that the two samples prepared by mechanical alloying (MA) and mechanical grinding (MG) maintain the BCC structure. Because the hydrogen atom enters the interstitial position of BCC, which leads to the increase of lattice parameters, so the spectral lines of both samples shift to low angle. This shows that the hydrogen absorption mode of this BCC structure is mainly alloy interstitial solid solution, and there is no phase transformation. Because the hydrogen absorption capacity of the sample prepared by mechanical alloying is larger than that of the mechanical grinding sample, the maximum hydrogen absorption capacity is 1wt%, and the displacement of the former is larger than that of the latter before and after hydrogen absorption. However, the shift of the diffraction peak to the low angle of the mechanically ground sample is larger in figure 16, which may be due to the large hydrogen release of the mechanically alloyed sample, and the remaining hydrogen content of the mechanically alloyed sample is lower than that of the mechanically ground sample, so the low angle displacement of the latter is larger.

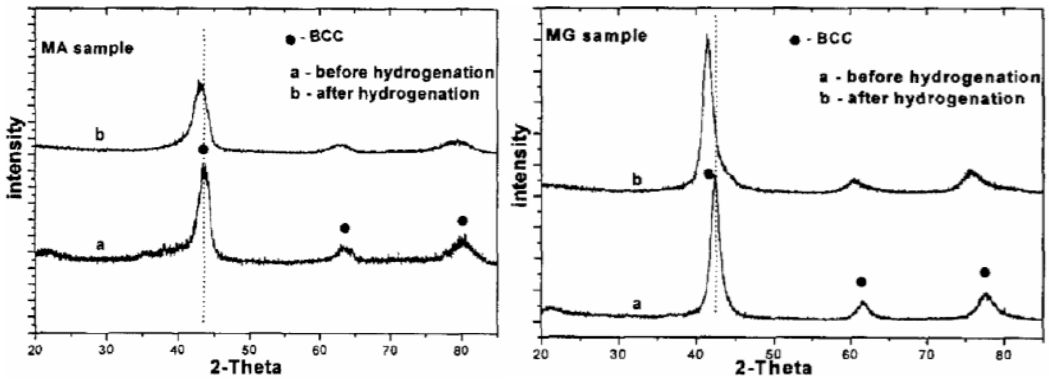

Fig. 16: Diffraction pattern of before and after hydrogen absorption for cubic TiCr2 alloy prepared by mechanical alloying (MA) and mechanical grinding (MG)[28]

In addition, the results of the study of AB_2 Laves phase listed in Table 5[29] . From the above results, it is known that the hydrogen absorption of Laves phase hydrogen storage alloy is larger than that of hydrogen storage alloy. The multi-structure does not change and the parent phase interstitial solid solution is formed.

Table 5: Study on the evolution of hydrogen absorption and desorption process of some AB2 Laves phase hydrogen storage materials [29]

AB_2 Intermetallic compound Laves phase	Available data of hydride	Reference
ZrM_2(M=V,Cr,Mn,Co,Mo)	The compound is the solid solution of the parent phase	[30]
$Zr(CoxM1\text{-}x)_2$,M=V,CrMn, 0＜x＜1	There is no evidence of phase transition, so it is a solid solution.	[31]，[32]
$Zr(V_xFe_{1-x})_2$,$Zr(Mn_xFe_{1-x})_2$, $Ti(V_xFe_{1-x})_2$, $Ti(Mn_xFe_{1-x})_2$	No structural study has been carried out	Brookhaven National Lab., 1977, 1978, 1979
$TiCr_2$	the $TiCr_{1.8}H_{2.1}$～$TiCr_{1.8}H_{3.6}$composition range is orthogonal structure.	[33]
$Zr(Al_xFe_{1-x})_2$和$Zr(Al_xCo_{1-x})_2$ 0＜x＜1	No structural change was observed.	[34]
$ZrMn_2$	Maintain hexagonal (C14) structure, deuterium atom occupies6h(1)、6h(2)、22kand 24l， The occupancy probability is respectively0.052、0.312、0.376and0.179	[35]
ZrV_2	Maintain cubic (C14) structure, deuterium atom occupies8b、32e and 96g，occupancy probability is respectively0.002，0.387，0.249	[36]

c) *Structural evolution of AB5 type rare earth alloys during hydrogen absorption and desorption*

i. *In situ X-ray diffraction study on the hydrogen absorption and desorption process of $LaNi_{4.83}Sn_{0.314}$ [37 ~ 38]*

Yuan Zhiqing, Lu Guanglie, Zeng Yuewu et al. In situ X-ray diffraction study on hydrogen absorption and desorption process of over stoichiometric rapid solidification alloy $LaNi_{4.83}Sn_{0.314}$. The XRD patterns and Rievteld structure refinement results of the main stages in the hydrogen charging and desorption process are shown in figure 17. It can be found from Fig. 17 that there are $\alpha + \beta$ two phases in hydrogen absorption to x=2.0, only one phase in x=4.0, and two phases in hydrogen desorption to x=1.5. Therefore, $LaNi_{4.83}Sn0._{314}$. The phase transition of the alloy during hydrogen charging and desorption shows a typic $\alpha \rightarrow \alpha + \beta \rightarrow \beta$ process, but the phase transition is pseudo-phase transition, that is, the crystal structure remains unchanged, as shown as shown in figure 17 (a) and (c), but the lines are obviously shifted to a low angle. α and β phases exist at the same time, indicating that both hydrogen absorption and hydrogen desorption have a process from the surface of the particles to the interior of the particles. With the deepening of the hydrogen charging process, the α phase content decreases and β phase increases, while

this change of phase content in the process of hydrogen evolution is the opposite.

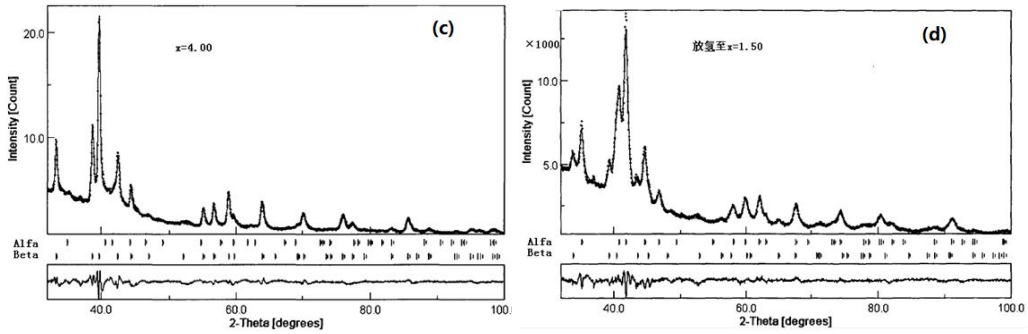

Fig. 17: XRD Pattern and Reiveld finishing results [37, 38] during hydrogen absorption of $LaNi_{4.83}Sn_{0.314}$alloy, (a) in the original sample (x= 0.0); (b)2.0; (c) 4.0 and (d) then desorption to x=1.5

ii. *Quasi-dynamic XRD study on the charge and discharge process of Ni-MH battery*

The XRD spectrum of the negative electrode active material AB_5 in several stages of charge and discharge of Ni-MH battery is shown in figure 18. On the whole, the structure of AB_5 alloy has no obvious change during charging, but the fine structure and microstructure have change. The lattice parameters a and c of AB_5 alloy increase with the increase of charging depth, and the micro-strain ε increases with the increase of charging depth. The discharge situation is just the opposite, but it returns to the original state, which indicates that there are some irreversible factors in the charge-discharge process. The results show that the crystal structure of $LaNi_5$ remains unchanged during the hydrogen absorption and discharge process of Ni-MH battery, but the microstructure parameters change accordingly. In other words, the process of hydrogen absorption and desorption is the formation and decomposition of interstitial solid solution of $LaNi_5$ alloy.

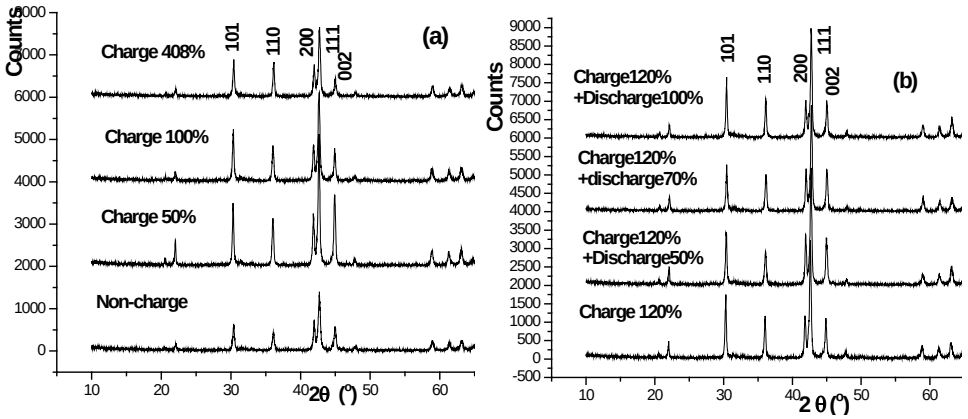

Fig.18: XRD pattern of negative electrode active material AB_5 alloy at several stages of charge (a) discharge (b) [39jue 40]

iii. *Experimental study on $LaNi_5$, $LaNi_{5-x}Al_x$, $LaNi_{5-x}Mn_x$ and their deuteride structures [42]*

LaNi5's experimental neutron diffraction pattern is given in figure 19, and the coarse looks very different, but after careful indexing and analysis, it is found that: 1) the position distribution of the diffraction lines is the same, and only the diffraction lines of deuteride are systematically shifted to a low angle, indicating that the crystal structures of the two are the same; 2) the diffraction lines of deuteride are obviously broadened and many lines have seriously overlapped. 3) the relative intensity of the line also changes obviously, which indicates that the deuterium atom participates in the diffraction after entering the gap position, which contributes to the diffraction intensity.

The refinement parameters of the Reitveld method are given to Table 6 and the refinement results are given to Table 7. It can be seen that the simulation results of the five-site model are more complex with the reality, indicating that the crystal structure of deuteride in $LaNi_5$ is the same as that of the parent phase, only because the deuterium atoms in the interstitial position participate in the diffraction, which makes the diffraction line system shift to the low angle direction and the line broadens, which is attributed to grain refinement and micro-strain. It is also known that Mn replaces 2c and 3g site of Ni, while Al only replaces 3G site of Ni.

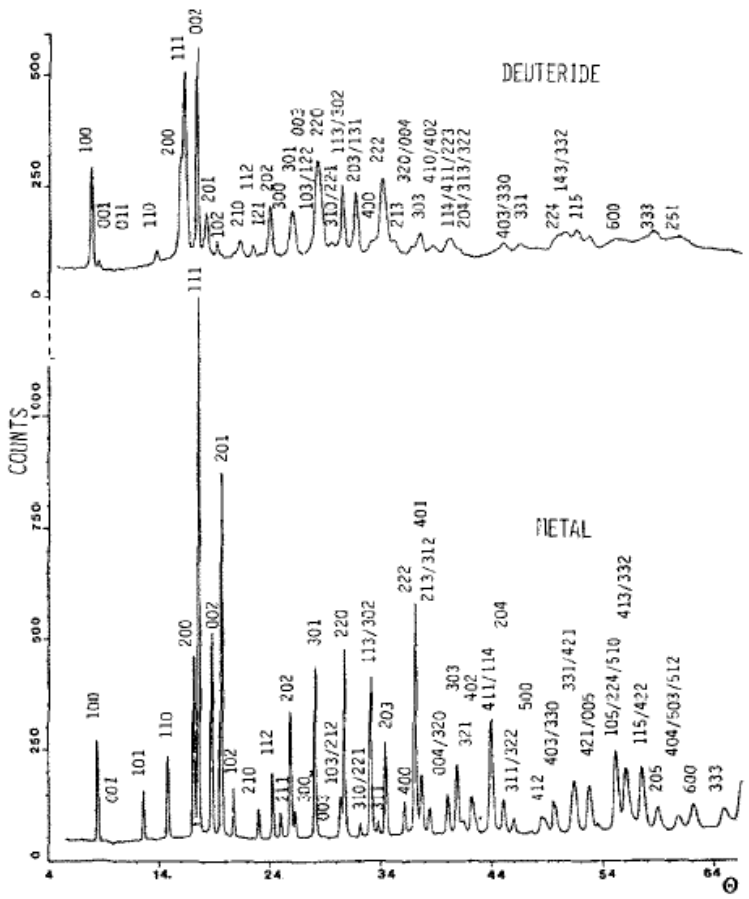

Fig. 19: Experimental neutron diffraction pattern of $LaNi_5$ (top) and its deuteride (bottom) [42], λ = 0.128nm

Table 6: Refining factor parameters of intermetallic compound $LaNi_5$-xMx (M-Mn,Al) [42]

Nominal component	$La_{1-s}Ni_{5+2s}$	$LaNi_{4.5}Mn_{0.5}$	$LaNi_4Mn$	$LaNi_3Mn_2$	$LaNi_4Al$
a (Å)Neutron	5.017	5.047	5.086	5.174	5.064
X-ray	5.016	5.045	5.089	5.174	5.069
C(Å)Neutron	3.986	4.019	4.085	4.145	4.070
X-ray	3.983	4.022	4.082	4.145	4.074
s(La)	0.017	0.011	0.005	0.017	0.007
s1(z=0)		0.059	0.128	0.155	0.00
s2(z=0.50		0.256	0.779	1.643	0.938
x(Ni-III)	0.287	0.285	0.283	0.278	0.283
z(Ni-IV)	0.313	0.310	0.305	0.301	0.305
Refined element La	0.983(3)	0.989(3)	0.995	0.983	0.993
Ni	5.03(3)	4.71(4)	4.10	3.24	4.08
M		0.32(3)	0.91	1.80	0.94
Normalized component	$LaNi_{5.12}$	$LaNi_{4.76}Mn_{0.92}$	$LaNi_{4.12}Mn_{0.91}$	$LaNi_{3.29}Mn_{1.83}$	$LaNi_{4.10}Al_{0.94}$
Refined Rfactor (%)	4.41	5.0	6.41	5.98	5.84

Table 7: Comparison of refinement of LaNi5 deuteride with two-site model and five-site model

Atom	Position	x	y	z	B	N
Two-position model, P31m, No.157, Hexagonal system, R=16.11%						
La	1a	0	0	0	2.05	0.98
Ni1	2h	1/3	2/3	0.93	1.63	1.90
Ni2	3c	0.74	0	0.46	2.32	3.0
Ni3	6d	0.27	0.54	0.02	1.63	0.10
Ni4	1a	0	0	0.29	1.63	0.04
D1	3c	0.49	0	0.06	1.83	3.0
D2	6d	0.17	0.83	0.50	1.65	3.5
Five-position model, P6/mmm No.191, Hexagonal system, R=7.3%						
La	1a	0	0	0	3.97	0.98
Ni1	2c	1/3	2/3	0	1.81	1.90
Ni2	3g	1/2	0	1/2	0.99	3
Ni3	6l	0.287	0.574	0	1.81	0.102
Ni4	2e	0	0	0.313	1.81	0.034
D1	3f	1/2	0	0	5.75	0.64
D2	4h	1/3	2/3	0.369	0.72	0.52
D3	6m	0.136	0.272	1/2	2.31	1.91
D4	12n	0.455	0	0.117	1.29	2.14
D5	12o	0.204	0.408	0.354	1.91	1.29

Endo et al. [43] studied the change of crystal structure of AB_5 type alloy by in situ XRD and Rietveld full spectrum fitting method. The phase structure of RTNi4.30Al0.30Mn0.40 is P6/mmm close packed hexagonal lattice before and after hydrogen absorption, while $RTNi_{3.55}Co_{0.75}Al_{0.30}Mn_{0.40}$ changes from Cmmm (No.65) orthorhombic lattice to P6/mmm close packed hexagonal lattice after hydrogen absorption. Nakanura et al. [44] used neutron diffraction technique to monitor the hydrogen absorption and desorption process of the alloy. The results show that the hydrogen absorption capacity of $LaNi_{5-x}Al_x$ alloy is related to its Al content. With the increase of Al content, the crystal structure of P63mc alloy changes from P63mc to P6mm and then to P6/mmm ($x \geq 0.5$). For this structural change, it is necessary to further determine the number of H atoms in the hydride phase and the crystallographic location of H.

d) Structural evolution of hydrogen storage materials during hydrogen absorption and desorption of magnesium system

i. Structural evolution of hydrogen absorption and desorption of $Mg_{88}Y_{12}$ alloy [13]

Wu and Zhang et al. [13] studied the hydrogen absorption and desorption process of $Mg_{88}Y_{12}$ alloy. Figure 20 shows the X-ray diffraction pattern of freshly cast $Mg_{88}Y_{12}$ alloy. It can be seen that there are main phase $Mg_{24}Y_5$ intermetallic phase and a small amount of Mg in the sample, and the relative contents of the two phases are calculated to be 75.9 wt.% ($Mg_{24}Y_5$) and 30.1 wt.% (Mg), respectively. $Mg_{24}Y_5$ has α-Mn structure, space group I43m nm;Mg 1.1240 is hexagonal, space group P63/mmc, a=0.3228 nm, c=0.5222 nm, c/a=1.6177. The lattice parameters of Mg phase in $Mg_{88}Y_{12}$ alloy are larger than those of pure Mg (a=0.3209 nm, c=0.5211 nm), but the lattice parameters of Mg phase are smaller than those of pure Mg (c/a=1.6239). The above results show that Y and Mg atoms are solid soluble in Mg and $Mg_{24}Y_5$ phases.

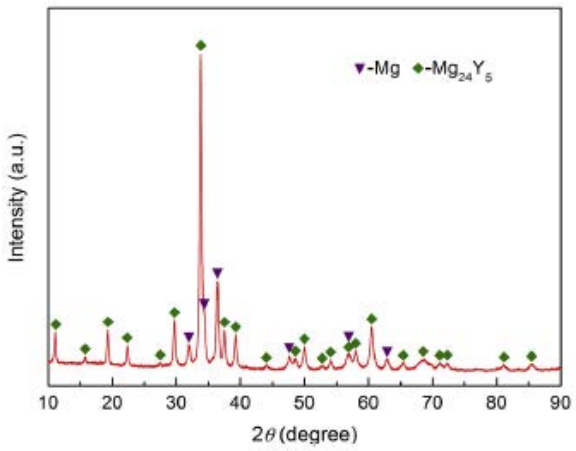

Fig. 20: X-ray diffraction pattern of freshly cast $Mg_{88}Y_{12}$ alloy [13]

The first hydrogenation (activation) curve of $Mg_{88}Y_{12}$ alloy at 380°C, 3MPa pressure is shown in figure 21 (a). It is clear that the first hydrogenation process is very slow. In the first 5 minutes, the hydrogen absorption capacity increases relatively fast, and then slowly increases, reaching the saturated maximum hydrogenation capacity of 6.479% after about 550min. Fig. 21 (b) shows the XRD pattern of $Mg_{88}Y_{12}$ alloy at different hydrogenation stages. After about 15% of the saturated hydrogen absorption capacity, the diffraction peak of $Mg_{24}Y_5$ phase almost disappears, while the diffraction peak of YH_2 appears, and the diffraction peak of Mg is high. During further hydrogenation, the MgH_2 diffraction peak appears with the decrease of Mg peak and increases slowly. When

the saturated 70% YH_3 has a small weak peak, it indicates that a small amount of YH_2 is transformed into YH_3. All hydrogenated alloys contain MgH_2, YH_2 and YH_3 phases. Therefore, the first hydrogenation process consists of the following two reactions:

1) Unbalanced reaction $Mg_{24}Y_5 + H2 \rightarrow Mg + YH_2$
2) Initial hydrogenation and MgH_2 formation: $Mg + H_2 \rightarrow MgH_2$;

Partial hydrogenation of YH_2 formed: $YH_2 + H_2 \rightarrow YH_3$

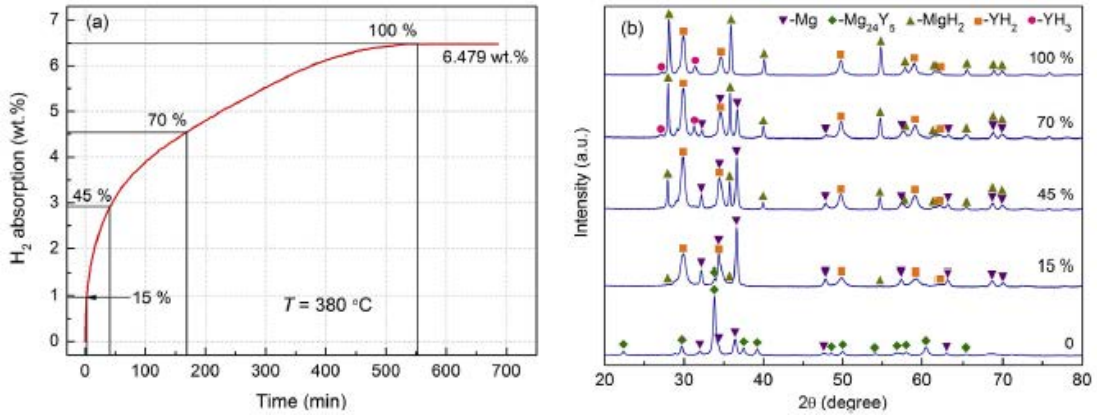

Fig. 21: (a) hydrogen absorption curve of first hydrogenation of $Mg_{88}Y_{12}$ alloy, (b)XRD pattern of alloy at different hydrogen absorption stages [13].

Table 8: Phase structure of $Mg_{88}Y_{12}$ alloy before and after hydrogen absorption and desorption [13]

	Phase %	Crystal system	Space group No.	PDFNo.	Z	Lattice parameter (nm)	
						a	c
before absorption	$Mg_{24}Y_5$75.9	Cubic	I43mNo. 217	31-0817	2	1.1204	
	Mg 30.1	Hexagonal	P63/mmc No.194	35-0821	2	0.32093	0.52112
After absorption	$YH_2$70%	Cubic	Fm-3mNo.225	12-0388	4	0.52077	
	MgH_2	Tetragonal	P42/mnmNo.136	12-697	2	0.4517	0.30205
	YH_3	Hexagonal	P-3c1 No.165	12-0385	6	0.6358	0.662

ii. *Structural evolution of Mg-Cu series alloys during hydrogen absorption and desorption [14,15]*

Fig. 22 (a) (b) shows that the Mg_2Cu samples without Y and Ni are XRD patterns and Rietveld finishing results before hydrogen absorption, respectively, as shown in Table 9. The Mg_2Cu sample without Y and Ni is the XRD pattern before hydrogen absorption and desorption and the results of Rietveld finishing are shown in figure 23, which is shown in Table 10. A comprehensive comparison of figure 22 and figure 23 and Table 9 and Table 10 shows the fact that hydrogen absorption produces a variety of hydrides and relies on hydrides for hydrogen storage, while hydrogen desorption is the release of hydrogen by hydride decomposition. The hydride phase of Mg-Cu alloy doped with Y and Ni after hydrogen absorption needs to be further studied.

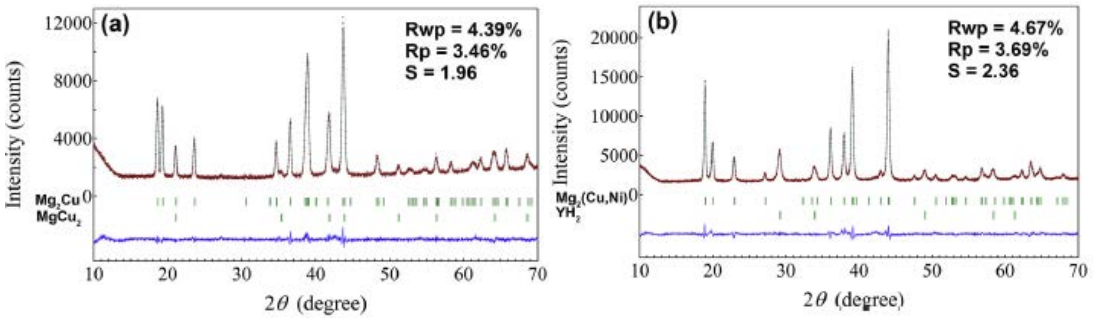

Fig. 22: XRD pattern and Rietveld refinement without hydrogen absorption, (a) undoped Mg_2Cu, (b) Mg_2Cu doped with Y and Ni

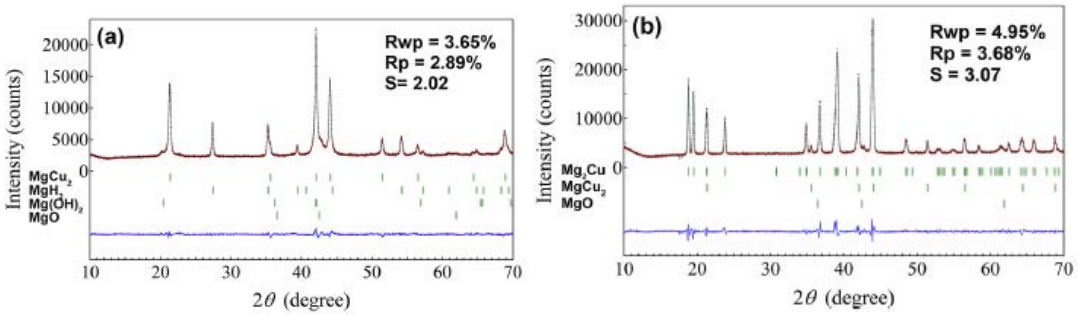

Fig. 23: XRD pattern and Rietveld refinement of undoped Mg_2Cu samples after hydrogen absorption and desorption, (a) hydrogenation of 300°C for 1h, (b) after hydrogen absorption. Dehydrogenation for 10 h at 300°C

Table 9: XRD pattern and Rietveld finishing results without Mg-Cu hydrogen absorption and desorption

Sample	Phase%	Space groupNo.PDF Z			点阵参数(nm)		
					a	b	c
Mg-Cu Alloy	Mg_2Cu 3	Fddd	70	13-0504 16	0.52753	0.90665	1.8332
	$MgCu_2$ 47	Fd-3m	227	01-1226 8	0.70429		
Absorption H_2 1h at 300°C	Mg_2Cu 70	Fddd	70	13-0504 16	0.79390		
	MgH_2 27	P42/mnm	136	12-0697 2	0.45116	0.30186	
	MgO 2	Fm-3m	225		0.4204		
	$Mg(OH)_2$ 1	P-3m1	164		0.2852	0.4254	
desorptionH_2 1h at 300°C	Mg_2Cu 82	Fddd	70	13-0504 16	0.52672	0.90830	1.8330
	$MgCu_2$ 13	Fd-3m	227	01-1226 8	0.70396		
	MgO 2	Fm-3m	225		0.4210		

Table 10: XRD patterns and Rietveld refinement results of Mg-Cu samples doped with Y and Ni after hydrogen absorption and desorption

Sample	phase %	Space group No. PDF Z			点阵参数 (nm)			
					a	b	c	β
Mg-Cualloy	$Mg_2(Cu,Ni)$ 92	$P6_222$			0.52474	1.3605		
	YH_2 8	Fm3m	225	12-0388 4	0.51980			
absorption $H_2$1h at300°C	$MgCu_2$ 46	Fd3m	227	01-1226 8	0.7038			
	MgH_2 23	P42/mnm	136	12-0697 2	0.4517	0.3022		
	Mg_2NiH_4 20	C2/C		15	1.4986	0.6279	0.9779	113.6
	YH_3 2	P-3c1	165	12-0385 6	0.6373	0.6589		
	YH_2 6	Fm-3m	225	12-0388	0.5242			
	MgO 1	Fm-3m	225		0.4143			
	$Mg(OH)_2$ 2	P-3m1	164		0.2814	0.4299		
Desorption $H_2$1h at 300°C	$MgCu_2$ 74	Fd3m	227	01-1226 8	0.5273	0.9071	1.8179	
	Mg_2Ni 17	P6222	180		0.5206	1.3166		
	YH_3 1	P-3c1	165	12-0385 6	0.6342	0.6602		
	YH_2 8	Fm-3m	225	12-0388 4	0.5219			

iii. *Study on on-line synchrotron radiation X-ray diffraction of $Mg_{90}Ni_{10}$, $Mg_{80}Ni_{10}Y_{10}$ and $Mg_{85}Cu_5Ni_5Y_5$ [44~46]*

Fig. 24 shows the crystalline phases of $Mg_{90}Ni_{10}$, $Mg_{80}Ni_{10}Y_{10}$ and $Mg_{85}Cu_5Ni_5Y_5$ samples identified by synchrotron radiation-XRD analysis after activation and hydrogenation-dehydrogenation cycle 11.5 cycles. The results are listed in table 11.

Table 11: Phases of three alloys after 11.5 cycles of activation and hydrogenation-dehydrogenation

Alloy	$Mg_{90}Ni_{10}$	$Mg_{80}Ni_{10}Y_{10}$	$Mg_{85}Cu_5Ni_5Y_5$
Phases of the alloy after 11.5 cycles of activation and hydrogenation-dehydrogenation	MgH_2 Mg $Mg_2NiH_{0.3}$ LT-Mg_2NiH_4 HT-Mg_2NiH_4	MgH_2 YH_3 YH_2 $MgCu_2$ $Mg_2NiH_{0.3}$	MgH_2 YH_3 LT-Mg_2NiH_4 HT-Mg_2NiH_4 Mg

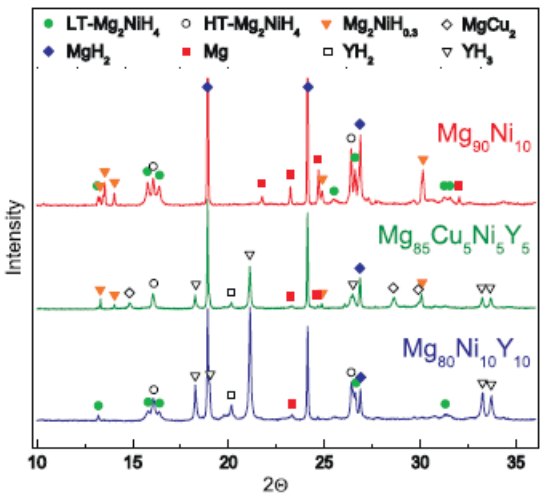

Fig. 24: Synchrotron radiation X-ray diffraction patterns of hydrogenated $Mg_{90}Ni_{10}$, $Mg_{80}Ni_{10}Y_{10}$ and $Mg_{85}Cu_5Ni_5Y_5$

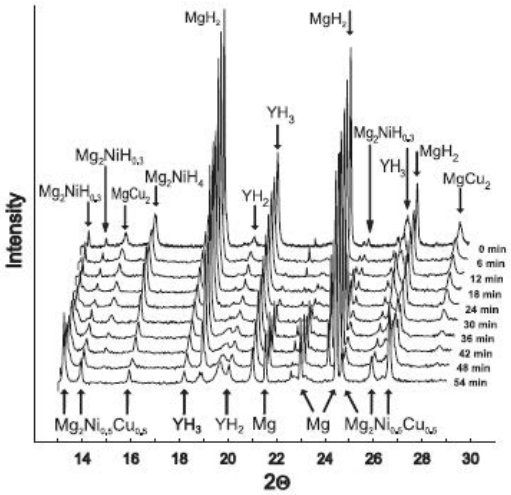

Fig. 25: Evolution of on-line synchrotron radiation XRD spectra of hydrogenated $Mg_{85}Cu_5Ni_5Y_5$ alloy under 10^{-2}mbar H_2 pressure and200°C isothermal dehydrogenation

This shows that the hydrogen desorption of $Mg_{90}Ni_{10}$ is divided into the following three steps:

1) Mg_2NiH_4 dehydrogenation, that is, Mg_2NiH_4 dehydrogenation $Mg_2NiH_{0.3}$;
2) in the prese;
3) $Mg_2NiH_{0.3}$ dehydrogenation, that is, $Mg_2NiH_{0.3}$ dehydrogenation Mg_2Ni.

Fig. 25 shows the evolution of on-line synchrotron radiation XRD spectra of hydrogenated $Mg_{85}Cu_5Ni_5Y_5$ alloy under 10^{-2}mbarH_2 pressure and 200°C isothermal dehydrogenation process, indicating that $Mg_{85}Cu_5Ni_5Y_5$ dehydrogenation is also divided into four steps:

1) $MgH_2 \rightarrow Mg + H_2$
2) $Mg_2NiH_4 \rightarrow Mg_2NiH_{0.3} + 1.85H_2$
3) $Mg_2NiH_{0.3} \rightarrow Mg_2Ni + 0.15H_2$
4) $2YH_3 \rightarrow 2YH_2 + H_2$

Similarly, the hydrogenation of Mg-Ni alloy without Cu and Y adulteration during the hydrogen absorption and desorption cycle of 11.5 periods is also worthy of further study.

e) Summary

From the research results of 3.1 to 3.4, it can be concluded that in the process of hydrogen absorption of Ti system, Laves phase and LaNi5 rare earth system hydrogen storage materials gradually enter the interstitial position of the alloy to form a solid solution and keep the crystal structure unchanged. Hydrogen storage is realized by this kind of hydrogenated solid solution, that is, the main body of hydrogen absorption is alloy interstitial hydrogenated solid solution. However, the situation of multi-component substituted LaNi5 alloy is more complex, and the structure of the parent phase changes. It can be seen from section 3.4 that in the process of hydrogen absorption, Mg hydrogen storage materials first decompose the alloy parent phase, and then gradually precipitate hydride, and hydrogen storage is realized by hydride, in other words, the main body of hydrogen absorption is metal hydride. However, besides MgH_2, YH_2 and YH_3, the hydride of Mg-Cu alloy doped with Y and Ni and Mg-Ni alloy doped with Y and Cu is an exception, which is worthy of further study.

Mg_2Ni belongs to hexagonal structure, P6222 $Mg_2NiH_{0.3}$ No.188 space group, Mg_2NiH_4 belongs to monoclinic structure, c/2c (No. 15) space group, then the hydrogenation process of Mg_2Ni is $Mg_2Ni \rightarrow Mg_2NiH_{0.3} \rightarrow Mg_2NiH_4$. Two kinds of intermediate phases, Mg_2Ni and $MgNi_2$, are found in the Mg-Ni binary phase diagram, and the weight percentages of Ni are about 55% and 83%, respectively. It is suggested that it is best to configure Mg_2Ni single-phase alloy samples, carry out hydrogen absorption and desorption tests, and track and determine the phase structure and lattice parameters of the parent phase and intermediate products as well as the final products after full hydrogen absorption, so as to judge whether the above results are correct and whether there is alloy hydride Mg_2NiH_4.

IV. Crystal Structure Characteristics Of Parent Material And Hydride Of Typical Hydrogen Storage Alloy

a) Space utilization, size and number of gaps in typical dense metal lattices [47]

There are three kinds of stacking structures in metals, the crystals of Mg and Be are dense hexagonal (CPH), Cu, Ag and Au are face-centered cubic (FCC), and the third common packing type is body-centered cubic (BCC), For example K, Na and-Tiet al. The calculation results of some important structural parameters and space utilization (%) of the three kinds of dense metals are listed in Table 12.

Table 12: Some important structural parameters of three close-packed metals [47]

Crystal structure	CPH	FCC	BCC
The space group and No.	P63/mmc No.194	Fm-3m No.225	Im-3m No.229
Metal example	Be, Mg、α-Ti, Y	Ni、Cu、Al	β-Ti，K、Na
Atomic stacking space utilization /%	74.05	74.05	68.02
Coordination number	12	12	8
The number of atoms in a unit cell	2	4	2
Atomic coordinates	1a000 1d 2/3,1/3,1/2	4a000; 1/2,1/2,0; 1/2,0,1/2; 0,1/2,1/2	2a000; 1/2,1/2,1/2
The relationship between unit cell parameters and atomic radius R	$a=b=2R$ $c=\frac{4}{3}\sqrt{6}R$	$a=2\sqrt{2}R$	$a=\frac{4}{\sqrt{3}}R$
The number of tetrahedral gaps. Can accommodate the maximum atomic radius	8 0.225R	4 0.225R	8 0.291R
The number of octahedral gaps Can accommodate the maximum atomic radius	4 0.414R	2 0.414R	6 0.154R

b) Characteristics of parent structure and hydride structure of TiFe

The most studied Ti alloy is TiFe, which belongs to CsCl structure. Some people think that the hydrogenation behavior of TiFe alloy goes through the process from TiFe (cubic crystal) to $TiFeH_{1.04}$ (tetragonal intermediate hydride phase) and then to $TiFeH_{1.95}$ (cubic crystal, saturated hydride phase).

Enter the keyword "hydride of TiFe hydrogen storage alloy" on the network, and it is also found that there are $TiFeH_{1.04}$ and $TiFeH_{1.95}$ statements. What is the credibility of these data? First of all, the hydrides of TiFe with CsCl structure in the process of hydrogen absorption and desorption are $TiFeH_{1.04}$ and $TiFeH_{1.95}$, but there is a lack of experimental evidence, and the card of this compound can not be found in PCPDF win database. However, Wajid, Ali et al. [6] retained the ordered BCC structure after hydrogen absorption by Cu and Y-substituted Ti-Fe-Mn alloys. It can be seen from Table 12 that there are 8 tetrahedral gaps and 6 octahedral gaps in the unit cell of BCC structure, The gap dimensions are 0.291R and 0.154R, respectively. The atomic radius of Ti is 0.145 nm, 0.145×0.291=0.0423nm. Because the atomic radius of Fe is smaller than that of Ti, only 0.135nm, and the actual gap radius is larger than 0.0423nm, the tetrahedral gap can accommodate H atoms with radius 0.045nm.

c) Crystal structure and interstitial position of Laves phase hydrogen storage alloy

Type C15 is typical of $MgZn_2$ with cubic structure, the stacking order of atomic plane is ABCABC, space group Fd3m; C14 is typical of $MgCu_2$ with hexagonal structure, the stacking order of atomic surface is ABABAB and space group is $P6_3/mmc$, and type C36 is typical of $MgNi_2$ with hexagonal structure, stacking order of atomic plane is ABACABAC and space group is $P6_3/mmc$. The crystal structure parameters and interstitial positions of three Laves phase hydrogen storage alloys are given in Table 13.

Table 13: Crystal structure parameters and interstitial holes in three AB_2 Laves phase hydrogen storage alloys [29]

Performance	Cubic Lavesphase (C15)	HexagonalLaves phase (C14)	HexagonalLavesphase (C36)
Structure type	MgCu type	$MgZn_2$type	$MgNi_2$
Spacegroup	Fd3m No.227	P63/mmc (No.194)	P63/mmc 194
The number of AB_2 in a unit cell	8	4	8
Ideal stacking condition	$R_A=\sqrt{3}a/8$ $R_B=\sqrt{2}a/8$ $d_{AB}=\sqrt{11}a/8$	$c=(2\sqrt{2}a)/\sqrt{3}$ $R_A=9\sqrt{6}a)/8$ R_B=a/4 $d_{AB}=(\sqrt{22}a)/8$	
Equivalent position	(000);(01/21/2); (1/201/2);(1/21/20)+ A 8a 1/8,1/8,1/8; 7/83/83/8 B 16d 1/2,1/2,1/2; 1/43/40; 3/401/4; 01/43/4	A 4f 1/3,2/3,z; z=1/16 B1 2a 0,0,0; 0,0,1/2 B2 6h z,2x,1/4;	A1 4e 0 0 z1 A2 4f 1/3 2/3 z2 B1 6g 1/2 0 0 B2 6h x 2x 1/4 B3 6f 1/3 2/3 1/8
Number of tetrahedral holes in B4 position Radius(nm)	8 8b Rs=0.0039780a	4 4c 0,0,z; 0,0,z+1/2; 0,0,-z; 0,0,-z+1/2 z=5/16 Rs=0.0056186a	
AB3 tetrahedral hole Number Position Number Position Radius(nm)	 32 32e x,x,x x=0.84891 Rs=0.004866a	I-type 4 4f 1/3,2/3,z z=0.66714 II-type 12 12k x,2x,z x=0.1292, z=0.1390 Rs=0.00688a	
Number of A2B2 tetrahedral holes position Radius (nm)	96 96g x,x,z x=0.19029 z=−0.005579 Rs=0.005266a	Total48 6h16 x,2x,1/2 x=0.4639 6h26 x,2x,1/2 x=0.2027 12k12 x,2x,z x=0.4565, z=0.6306 24/24 x,y,z x=0.04353, y=0.3259, z=0.5653 All A2B2 holes have the same radius Rs=0.0074475a	
The total number of tetrahedral holes	There are 17 holes in each AB2 unit, and there are 8 AB2 molecules in the unit cell, so there are a total of 136 holes.	There are 17 holes in each AB2 unit, and there are 4 molecules in the unit cell, so there are a total of 68 holes.	

The schematic diagram of the phase structure of cubic and hexagonal Laves is shown in figure 26. According to the hard sphere packing model, the ideal atomic radius ratio (rA/rB) of Laves phase is1.225 . However, in many binary or quasi-binary Laves phase alloys, the atomic radius ratio of rA and rB deviates from 1.225, and the radius ratio can vary in the range of 1.05 ～ 1.68. In addition to the atomic size, the phase structure of Laves also depends on the electron density. The statistical results show that the electron concentration (valence electron / atom) of Laves phase structure is 2.0 for C14 type, 1.7 for C15 type and 1.90 for C36 type.

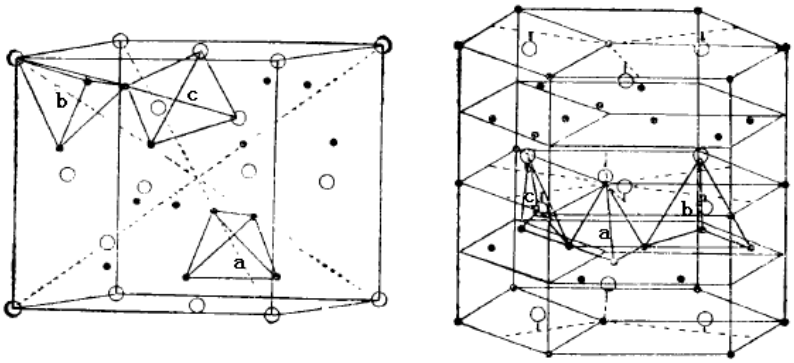

Fig. 26: Schematic diagram of Laves phase structure of cubic and hexagonal structure and three types of gaps in crystal cell

O is A atom ● is B atom, a is B4 closed gap, b is AB3 gap, c is AB2 gap.

All the cell gaps of Laves phase alloys are tetrahedral gaps. There are three types of tetrahedral gaps, namely, AB2, AB3 and B4 (see figure 26). The total number of tetrahedral gaps per unit cell is 17, in which A2B2 is 12, AB3 is 4, B4 is I. When the Laves phase alloy absorbs hydrogen, the hydrogen occupies the tetrahedral gap, which makes the cell volume expand, but the crystal form does not change. In the hydrogenated solid solution of Laves phase alloy, not all tetrahedral gaps are occupied by hydrogen atoms, but some of the gaps can be occupied by hydrogen atoms, which is mainly due to electrostatic restrictions.

d) Characteristics of parent structure and hydride structure of $LaNi_5$ alloy [48,51]

i. *The research results of Magee and Liu on $LaNi_5$ phase hydrogen storage alloy [48]*

$LaNi_5$ crystal belongs to $CaCu_5$ type structure and belongs to hexagonal system with space group P6/mmm (No.191). Its crystal structure model is shown in Fig. 27. As early as 1981, Magee and Liu [48] published the research results on the number, size, location and symmetry of tetrahedral interstitial holes in four families of intermetallic compounds under the topic of "the relationship between the structure of intermetallic compounds and hydride formation". Table 14 shows the $LaNi_5$ gap position and related parameters.

Table 14: Interstitial holes in the structure of AB_5 intermetallic compounds [58]

AB_5 intermetallic compound	Ideal stacking condition	Equivalent position	Number of tetrahedral holes in B4	AB_3 tetrahedral hole	A_2B_2 tetrahedral hole	The total number of AB_5hedron holes
CaCu5type P6/mmm No.191	$c=(\sqrt{2}/\sqrt{3})a$ R_B=a/4 R_A= $(1/\sqrt{3})a-a/4$	A 1a 0 0 0 B1 2c 1/3,2/3,0 ; 2/3,1/3 0 B2 3g 1/2,0,1/2; 0,1/2,1/2; 1/2,1/2,1/2	4h 4 1/3,2/3,z; 2/3,1/3.z; 2/3,1/3,-z; 1/3,2/3,-z z=5/8 Rs=0.05619a	I-type 12o 12 x,2x,z x=0.1949; z=0.2712 Rs=0.07636a II-type 12n12 x,0,z x =0.3896, z=1/6 Rs=0.07546a	6m 6 x,2x,1/2 x=0.0971 Rs=0.1142a	There are 34 holes per AB5 unit.

ii. *LaNi5H x < 6.0interstitial hole*

After $LaNi_5$ hydrogen absorption, the crystal system and space group remain unchanged, the crystal cell expands, and the lattice constant changes greatly. The voids in the lattice can be composed of the same metal atoms or a mixture of different metal atoms, so there are many types, the most important of which are tetrahedral voids and octahedral voids. In a $LaNi_5$ cell, there are 37 voids of five types, namely, 6 voids of 6m type, 12 voids of 12n type, 12 voids of 12o type, 4

voids of 4h type and 3 voids of 3f type. Fig. 28 shows a three-dimensional diagram of the five voids in the LaNi5 cell. Figure 29 shows the interstitial positions in the five-site model of the hydride phase.

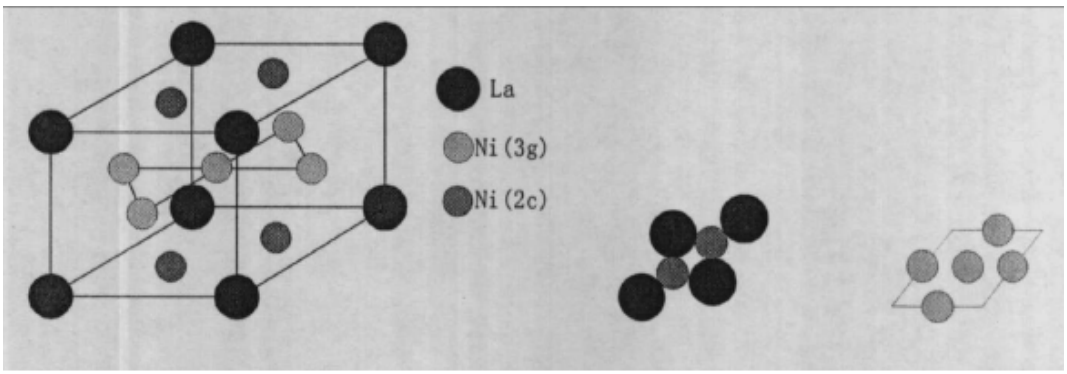

Fig. 27: A schematic diagram of the crystal structure of $LaNi_5$ alloy

a) LaNi5 structure model; b) the arrangement of atoms on the bottom surface; c) the arrangement of atoms on the c-axis of 1pm

Table 15: Changes of lattice parameters and cell volume of LaNi5 before and after hydrogen absorption

	a/nm	b/nm	c/nm	V/nm^3(each cell)	ΔV/nm^3(each H atom)	
$LaNi_5$	0.5014		0.3892	84.7×10^{-3}		
$LaNi5H_{6.5}$	0.5399		0.4290	108.30×10^{-3}	2.36×10^{-3}	27.86%

Cao and Chen et al. [49] think that there are mainly four kinds of interstitial positions: tetrahedron, hexahedron, octahedron and dodecahedron. The important parameters are shown in Table 16, and the interstitial positions in the five positions of hydride phase are also listed in Table 16 (see figure 29).

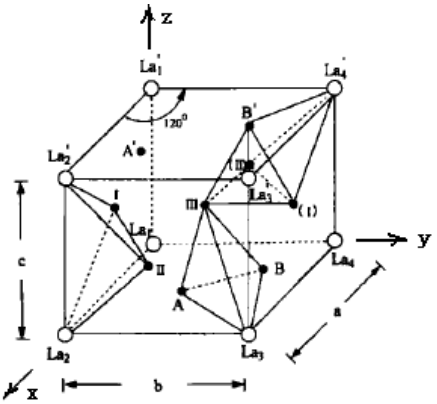

Fig. 28: Stereoscopic diagram of five gap positions of LaNi5 species

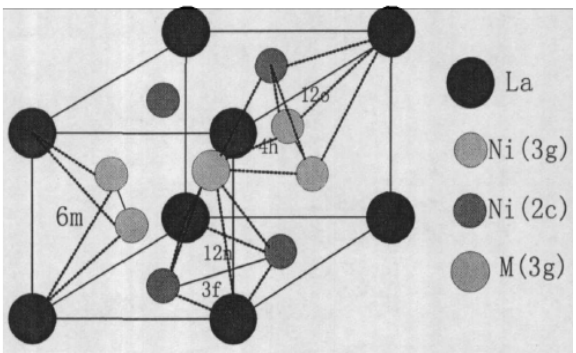

Fig. 29: The interstitial position in the five-site model of hydride phase

Table 16: Gap position in $LaNi_5$ structure [51]

Gap location name	Gap space radius (nm)	Number	Five-sites model of β-hydride		
			Gap position	Gap structure	Gap space radius
Tetrahedron	0.043	36	12o	AB_3	0.5548
Hexahedron	0.068	6	12n	AB_3	0.4482
Octahedron	0.106	9	6m	A_2B	0.4333
Dodecahedron	0.146	3	4h	B_4	0.3927
			3f	A_2B_4	0.3126

Wang Hong and Liu Zuyan [51] in the paper "crystallographic Analysis of the maximum hydrogen Storage capacity of $LaNi_5$", according to the atomic radius of hydrogen is 0.045nm (or 0.078nm), theoretically, a $LaNi_5$ cell can hold 18 hydrogen atoms, and one La atom and 5 Ni atoms in one cell, the mass fraction of maximum hydrogen storage can be calculated. This is basically consistent with the measured hydrogen storage mass fraction of 1.35-1.38% [50-51]

e) *Crystal structure and microstructure of $LaNi_5$ type hydrogen storage materials for hydrogen absorption and desorption*

There are mainly three viewpoints in the literature, namely: phase two-phase model and phase five-bit model.

i. *β Phase two-positions model*

Bowmna et al. [52] believe that during the hydrogen charging process, the spatial symmetry of the compound changes from P6/mmm (No.191) to P3lm (No.162), and the 3c (z=1) position is completely occupied by hydrogen, and hydrogen occupies part of the 6d position (z = 0.5). However, in the P31m (No.162) space group, although La occupies 1a (000) site, Ni (1) occupies 2c (1/2, 2/3, 0), and Ni (2) occupies 3G (1/2,0,1/2) (1/2,0,1/2), there are no 3c and 6d bits, Therefore, it is worth discussing.

Yartis et al. [53] think that hydrogen occupies the positions of 6g1(x, y, z=0.1) and 6g2(x, y, z=0.5), so there are 6 subordinate gaps of 6g, 12n-type12voids, 12 12o-type 12 voids, 4h-type4 voids and 3f-type 3 voids in the space group. Figure 28 shows a three-dimensional diagram of the five voids in the LaNi5 cell. Figure 29 shows the interstitial position in the five-site model of the hydride phase. In the transition from P6/mmm (No.191) to P321 (No.150), La atom occupies 1a (000) position and Ni (1) occupies 2d(1/3, 2/3, z=0) in P321 space group. Ni (2) occupies 3f (x=1/2, 0, 1/2) position.

ii. *β Phase five-positions model*

Perchron-Guigan [54] et al used different space groups to calculate the crystal structure of hydride. After comparing the results, it was found that the space group of the compound did not change before and after desorption and it was still P6/mmm. Based on this, they proposed a five-bit model, that is, hydrogen atoms occupy at 3f, 4h (z=0.5), 6m, 12n and 12o sites, respectively.

The studies of Latroche [55] and Chartouni et al. [56] have confirmed that for some alloys with specific composition, there is another hydride phase $AB_5H_{x=3}$ in the platform stage, which also belongs to hexagonal system, but the formation mechanism is not clear and the crystal structure is questionable. However, The existence of this phase can greatly reduce the discontinuous lattice expansion from α phase to β phase.

For γ phase hydride ($LaNi_5D_{x=6.0\sim7.0}$), the consistent view is that the order of the compound changes in the super lattice in the c-axis direction. The hydrogen absorption positions in P6/mmm are 4h (1/3,2/3,z=0.37), 6m(1/3,2/3,1/2), 2o(x,2x,z=0.35), and 12n (0.46,0,z=0.2) in P63mc (No.186), 2b(l/3,2/3, =0.8), 6cl(x,2x,z=1/4), 6c2(x,2x, z=0.3) as well as 12d(x,0,z=0.06)0.06 in the No.186 space group, respectively. No La occupies 1a (000) and Ni (1) occupies 2c(1/3,2/3,0) and Ni (2) occupies 3g (1/2,0,1/2. Therefore, the latter statement is worthy of negotiation.

f) *Parent structure and hydride structure of Mg-based hydrogen storage alloy*

The parent phases of $Mg_{88}Y_{12}$ are $Mg_{24}Y_5$ and Mg, and the hydrides are MgH_2, YH_2 and YH_3, which are obviously formed by the decomposition of $Mg_{24}Y_5$. The parent phases of Mg_2Cu without Y and Ni are Mg_2Cu and $MgCu_2$, the products after hydrogen absorption are $MgCu_2$ and MgH_2, and only MgH_2 is hydride, indicating that Mg_2Cu is decomposed into $MgCu_2$ and Mg, Mg to form hydrides with H, while the parent phases of alloys doped with Y and Ni are Mg_2 (Cu, Ni) and YH, and the hydrides formed after hydrogen absorption are MgH_2, Mg_2NiH_4, YH_3 and YH_2, indicating that Mg_2(Cu, Ni) has been decomposed.

The formation of hydride phases such as MgH_2, Mg_2NiH_4, YH_3 and YH_2 is discussed as follows. There are two possibilities: 1) decomposition products of parent phase. When the crystalline phase is not formed, the atomic states of Mg and Y react with H to form MgH_2, YH_2 and YH_3; 2) the parent phase decomposition products Mg and Y react with H after the crystalline phase has been formed. Because both Mg and Y belong to the hexagonal structure of A3-type density, the space groups P63/mmc and No.194 have two atoms in the unit cell, and their positions are: 0,0,0; 1/3,2/3,1/2. While MgH_2 belongs to $P4_2/mnn$, No.136; YH_2 and YH_3 belong to Fm-3m,No.225 and P-3c1, No.165respectively. They belong to different structural types, which shows that the first is more likely.

Mg_2Ni is the decomposition product of Mg_2(Cu,Ni) phase, which belongs to hexagonal structure, space group P6222, No.180, while Mg_2NiH_4 is monoclinic, C2/c, No.15, Mg_2NiH_4 is the product of solid-gas reaction, which belongs to the second case.

g) *Microstructure study on the process of hydrogen absorption and desorption*

Except for the microstructure (lattice parameters, micro-strain) mentioned in the charge and discharge process of Ni-MH battery, few of the above discussions do not involve the mother in the process of hydrogen absorption and desorption.

Phase harmony and microstructure of hydride. In fact, in the process of hydrogen absorption and desorption, whether it is the formation of alloy interstitial solid solution or the formation of hydride phase, the microstructure of the phase involved (grain refinement, micro-stress, lattice parameters and defects) may change with the process of hydrogen absorption and desorption. There are few reports except for some studies carried out by Professor Lu Guanglie's research group of Zhejiang University[37,38]. The changes of microstructure parameters (strain) of $LaNi_{3.75}Co_{0.75}Mn_{0.3}A1_{0.2}$ alloy in each stage of hydrogen absorption and desorption process are described below.

Fig. 30 shows the lattice strain of α phase (a) and β phase (b) along (001) and (110) crystal plane direction of $LaNi_{3.75}Co_{0.75}Mn_{0.3}A1_{0.2}$ alloy during hydrogen charging and desorption, respectively. A considerable number of lattice defects will be formed in the hydride phase in the hydrogen charging stage, mainly dislocations. These dislocations form small-angle grain boundaries, which are equivalent to grain refinement. In the hydrogen desorption stage, due to the gradual decrease of hydrogen content in the hydride phase, the direction of lattice elastic distortion is opposite to that of hydrogen charging, so dislocation reaction and dislocation aggregation occur, and the total number of dislocations decreases gradually. the small grains blocked by small angle grain boundaries re-aggregate into large grains.

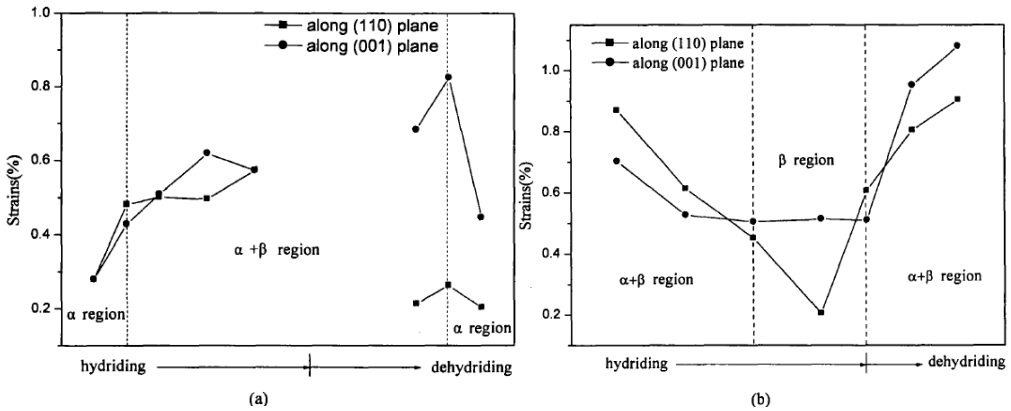

Fig. 30: During each stage of hydrogen absorption and desorption process, each phase of $LaNi_{3.75}Co_{0.75}Mn_{0.3}A1_{0.2}$ alloy follows (001). Lattice strain in the direction of the crystal (100) and (110) plane [37,38]. (a) α phase; (b) β phase.

V. Dynamic Mechanism of Hydrogen Absorption and Desorption of Alloy Hydrogen Storage Materials

Based on the comprehensive analysis of the contents described in Section 2-4, this section discusses the mechanisms of hydrogen absorption, hydrogen desorption and hydrogen storage of hydrogen storage materials. Because the alloy hydrogen storage material is crystalline, its hydrogen absorption and desorption process and hydrogen storage capacity are closely related to the crystal structure change and stability of the crystalline hydrogen storage material. Let's discuss the kinetic mechanism of hydrogen storage.

a) Surface reaction-adsorption and desorption [3P 57] and H diffusion in hydrogen storage materials

Hydrogen molecules and dissociated hydrogen atoms will react with the surface of hydrogen storage materials, including physical adsorption, chemical adsorption, and then permeate to the surface of the materials. In addition, there is also desorption phenomenon. The adsorption and desorption are related to the hydrogen pressure and temperature when absorbing hydrogen, and to the kinds of hydrogen absorbing materials.

At the initial stage, the hydrogen atoms that reach the surface of the material spread inward through various paths. Generally speaking, there is diffusion along the grain boundary and within the grain. From the introduction to Section 4.

The space utilization of different dense stack structures is different, the number of gap positions and the size of gap space are different, which seriously affects the intragranular diffusion of H in hydrogen storage alloys. In addition, the number and distribution of crystal defects in hydrogen storage materials will also affect the intragranular diffusion of H in hydrogen storage alloys. If the grains are fine, there are many grain boundaries, and the diffusion rate is relatively fast, so the nanocrystalline materials have better diffusion properties.

If the surface concentration is constant, the function of the weight change caused by the diffusion of hydrogen to the spherical particles with radius an is as follows:

$$\frac{M_t}{M_\infty} = 1 - \frac{6}{\pi^2}\sum_{n=1}^{\infty}\frac{1}{n^2}\exp\left(\frac{Dn^2\pi^2 t}{a^2}\right) \quad (16)$$

In the formula, M_t is the amount of hydrogen entering the sphere in time t; M_∞ is the amount of hydrogen after an infinitely long time; and D is the diffusion coefficient. The formula is suitable for the case of equal hydrogen pressure.

b) Hydrogen storage mechanism of alloy hydrogen storage materials

i. *General description*

It is generally believed that metal or alloy (represented by M) reacts with hydrogen to form metal (alloy) hydride (MHn). The reaction equation is as follows:

$$M + nH = MH_n + \triangle H$$

△H is heat of formation.

The reaction is a reversible process. In the forward reaction, the metal material absorbs hydrogen and gives off heat; in the reverse reaction, the metal hydride releases hydrogen and absorbs heat. In this way, the reaction can be repeated in the positive or reverse direction only by changing the temperature and pressure. To achieve the purpose of hydrogen storage or release of metal (alloy).

The energy change of hydrogen storage process can be divided into three parts: 1) Hydrogen dissociates from gaseous molecules to atomic state requires energy $\triangle H_1$, that is, hydrogen dissociation energy−4.75eV; 2) after hydrogen enters the metal crystal, it interacts with the metal, that is, the energy change $\triangle H_2$ produced by bonding.

$$H_2 \rightarrow 2H \qquad (\triangle H_1 = -4.75eV)$$

$$6.5H + M \rightarrow MH_{6.5} \qquad (\triangle H_2)$$

So there is

$$\frac{6.5}{2}H_2 + M \rightarrow MH_{6.5} \quad (\triangle H = \triangle H_1 + \triangle H_2)$$

The step of $H_2 \rightarrow 2H$ can be considered to be the same for any hydrogen storage material at the same temperature and hydrogen pressure. The problem is that the $6.5H+M \rightarrow MH_{6.5}$ step, due to the wide variety of M, varies greatly for different alloy hydrogen storage materials, and may even be divided into many different small steps. What is M? What is $MH_{6.5}$? All of them need to be tested and studied.

ii. *The interstitial position of hydrogen atom entering the parent phase-the formation of hydrogenated solid solution*

From the discussion of the number, size and position of interstitial holes in the parent phase structure of TiFe alloy, $LaNi_5$ and Laves phase, when the interstitial hole radius is greater than or equal to the radius of hydrogen atom, the interstitial position of hydrogen atom entering the main lattice of alloy hydrogen storage material changes from less to more, until saturated, but the crystal structure of the main body of alloy hydrogen storage material remains unchanged, but its microstructure and fine structure will change. This is the formation process of hydrogenated solid solution.

In this way, it is obviously inappropriate to regard LaNi5H6.5 as an alloy hydride, but a hydrogenated solid solution, and it is more scientific and reasonable to write the general formula as $LaNi_5$-Hn.

The value of n is different in different stages of hydrogen absorption. As we know from Section4.2, the maximum theory of n can reach 18. Hydrogen evolution is a reversible process, that is, the hydrogenated solid solution decomposes step by step and releases hydrogen.

iii. *Decomposition of parent phase and precipitation and formation of hydride in hydrogen storage materials*

There are also a variety of alloy hydrogen storage materials, and their crystal structure, composition and composition are different. From the introduction of sections 2 and 3, it can be seen that the alloy hydrogen storage materials may be single-phase or multiphase, and their crystal structures will be different. For example, $Mg_{88}Y_{12}$ is composed of $Mg_{24}Y_5$ with α-Mn structure, space group I43m,a=1.1240nm and hexagonal Mg. The structural evolution of Mg series hydrogen storage materials during hydrogen absorption and desorption is introduced from sections 3.4 and 4.4. The results of XRD analysis show that $Mg_{88}Y_{12}$ alloy is first hydrogenated (activated) at 380°C~3MPa pressure, and the hydrogen absorption capacity increases relatively fast in the first 5 minutes, and then increases slowly. The maximum hydrogenation capacity of 6.479% was reached after about 550 minutes. Fig. 21 (b) shows the XRD pattern of $Mg_{88}Y_{12}$ alloy at different hydrogenation stages. After about 15% of the saturated hydrogen absorption capacity, the diffraction peak of $Mg_{24}Y_5$ phase almost disappears, while the diffraction peak of YH_2 appears, and the diffraction peak of Mg is high. During further hydrogenation, the MgH_2 diffraction peak appears with the decrease of Mg peak and increases slowly. When the saturated 70% YH_3 has a small weak peak, it indicates that a small amount of YH_2 is transformed into YH_3. All hydrogenated alloys contain the formation of MgH_2, YH_2 and YH_3 phases. Now write: 45% hydrogen absorption

$$Mg_{88}Y_{12}\ (Mg_{24}Y_5 + Mg) \rightarrow Mg + YH_2 + YH_3$$

It is obvious that the parent phase $Mg_{24}Y_5$ of hydrogen storage materials disappears, and hydrogen storage phases YH_2 and YH_3 are precipitated, but Mg phase still exists. And after 100% hydrogen absorption,

$$Mg_{88}Y_{12}\ (Mg_{24}Y_5 + Mg) \rightarrow MgH_2 + YH_2 + YH_3$$

All the parent phase disappears and the hydrogen absorption phase is all formed, so the hydrogen absorption of hydrogen storage materials is accompanied by the decomposition of the parent phase and the precipitation/formation of the hydride phase, which includes the nucleation and growth of the new phase. The hydrogen evolution process is the gradual decomposition of the hydride hydrogen storage phase and the release of hydrogen. This obviously shows that the hydride of alloy $Mg_{88}Y_{12}$can not be written as $Mg_{88}Y_{12}H_n$, because Mg88Y12 alloy includes two phases of $Mg_{24}Y_5$+Mg, and the hydride can not be written as $(Mg_{24}Y_5+Mg)H_n$ or $(Mg_{24}Y_5H_n+MgH_n)$, but there is a process, namely $Mg_{24}Y_5$+Mg $\rightarrow YH_2+MgH_2 \rightarrow MgH_2+YH_2+YH_3$.

Similarly, for the Mg-Cu system

Parent phase%Main phase after The main phase after

hydrogen absorption%hydrogen desorption%

Mg_2Cu	83	$MgCu_2$	76	Mg_2Cu	82
$MgCu_2$	17	MgH_2	27	$MgCu_2$	16

It can be seen that the parent phase Mg_2Cu is decomposed and MgH_2 is formed. As for the MgCu2 in the parent phase, which is the Laves phase with Fd3m structure, whether the hydrogenated solid solution $MgCu_2$-H_n is formed in the process of hydrogen absorption and desorption remains to be further studied. The method is to configure the sample of single-phase $MgCu_2$, carry out the hydrogen absorption and desorption test, and at the same time track the process of hydrogen absorption and desorption to determine the crystal structure of the parent phase, the intermediate phase and the final phase and accurately determine the lattice parameters.

For Mg-Cu alloy doped with Y and Ni and Mg-Ni alloy doped with Y and Cu, except for MgH_2, YH_2 and YH_3, Mg_2NiH_4 alloy hydride appears to be an exception.

Mg_2Ni belongs to hexagonal structure, P6222 $Mg_2NiH_{0.3}$ No. 188 space group, Mg_2NiH_4 belongs to monoclinic structure, c2/c (No.15) space group, then the hydrogenation process of Mg_2Ni is$Mg_2Ni \rightarrow Mg_2NiH_{0.3} \rightarrow Mg_2NiH_4$. Two kinds of intermediate phases, Mg_2Ni and $MgNi_2$, are found in the Mg-Ni binary phase diagram, and the weight percentages of Ni are about 55% and 83%, respectively. It is suggested that it is best to configure Mg_2Ni single-phase alloy samples, carry out hydrogen absorption and desorption tests, and track and determine the phase structure and lattice parameters of the parent phase and intermediate products as well as the final products after full hydrogen absorption, so as to judge whether the above results are correct and whether there is alloy hydride Mg_2NiH_4.

VI. Comprehensive Analysis and Conclusions and Prospects [59]

a) Comprehensive analysis

According to the introduction of section 2 to section 34.5 of this article, a comprehensive analysis of the related problems is as follows.

i. *Thermo-dynamic analysis of the mechanism of hydrogen absorption and desorption*

Zhang Xiulan, Huang Zhuan, Chen Bo et al. [58] have made a thermodynamic analysis of the hydrogen storage process of $LiNi_5$. According to the thermodynamic function in the equilibrium state, the ability to finish is derived. The equilibrium formula of P-C-T relation in the whole experimental range is described. The variation curves of equilibrium pressure and hydrogen storage capacity at different temperatures are fitted and analyzed by using P-C-T equilibrium formula, and the thermodynamic function of equilibrium reaction in hydrogen storage process is calculated and discussed. The following is only a qualitative discussion.

Considering the crystal structure characteristics of alloy hydrogen storage materials, it can be divided into two types: 1) The crystal structure is dense or close to ideal dense stacking, and it is easy to form Hydride compound with H.For example, pure Mg is closest to ideal dense stack (c/a=1.633) ; 2) The second kind is that the utilization of atoms in lattice space is low, there are many interstitial positions, and the radius of interstitial space is larger than radius of H atom, so it is easy to form hydrogenated solid solution.

From the point of view of the real hydrogen storage body of alloy hydrogen storage materials, it can also be divided into two categories:

1) one is hydride, in other words, the hydrogen absorption process is the parent phase decomposition and subsequent formation of hydride ;and hydrogen desorption is the decomposition process of hydride;
2) The process of hydrogen absorption is the diffusion of H atom into the interstitial hole in the crystal of hydrogen storage material, and the dilute solid solution containing hydrogen is gradually formed. until the saturated/ supersaturated solid solution is formed, hydrogen desorption is the decomposition of hydrogenated solid solution and hydrogen release.

Compared with hydrogenated solid solution, the main body of hydrogen storage belongs to hydride, which is very different in the diffusion mechanism and the formation process of hydrogen storage body. For

former, hydrogen atom mainly diffuses along the grain boundary, and the decomposition of the parent phase and the formation of the new phase first occur at the grain boundary, and then expand into the grain, while for latter, hydrogen atom mainly diffuses into the interstitial position of the parent phase of the hydrogen storage material, and the formation of hydrogenated solid solution also begins inside the grain.

The formation processes of the two types of hydrogen storage bodies are different, and their thermodynamic processes should also be obviously different. For example, the energy required for diffusion along the grain boundary is lower, and the embedding into interstitial position in the grain needs to overcome a higher potential barrier; relatively speaking, the energy of hydride nucleation and flower growth is relatively small, while the formation of hydrogenated solid solution takes more energy.

At a certain hydrogen pressure, when the temperature increases, the parent phase is easier to decompose and the hydride is easier to form, so the hydrogen absorption and desorption kinetics of this kind of hydrogen storage material is characteristic.

The results show that the hydrogen absorption rate and hydrogen absorption capacity increase with the increase of temperature; on the contrary, the increase of temperature has little effect on the diffusion of hydrogen atoms into the matrix of the alloy. therefore, the hydrogen absorption kinetics of hydrogen storage materials whose hydrogen storage body is hydrogenated solid solution shows that the hydrogen absorption rate and hydrogen absorption capacity decrease with the increase of temperature.

When the hydride and the hydrogenated solid solution are formed, it needs to be restored to the equilibrium state, and the energy released by the material whose hydrogen storage body is hydride when it returns to the equilibrium state.

The quantity (heat) is much lower, and the material whose main body of hydrogen absorption is hydrogenated solid solution releases a large amount of energy (heat) when the equilibrium is restored. Therefore, it is not comprehensive to say that hydrogen absorption is an exothermic process and hydrogen desorption is an endothermic process. In fact, hydrogen desorption is achieved through the decomposition of hydride or hydrogenated solid solution of hydrogen storage, which of course needs to absorb heat, but after hydrogen desorption, the system needs to release heat to restore to equilibrium state. On the whole, whether it is the hydrogen absorption process or the hydrogen release process, the endothermic and exothermic processes cross each other, that is, some regions are endothermic while others are exothermic.

ii. *On the volume expansion in the process of hydrogen absorption*

For the alloy with hydrogenated solid solution as the main body of hydrogen absorption, the lattice parameters and cell volume always increase because the hydrogen atom enters the interstitial position of the parent phase lattice, so the hydrogen absorption process is accompanied by a certain volume expansion. therefore, the hydrogen storage container should have enough space to avoid explosion during hydrogen absorption.

For the alloy with hydride as the main body of hydrogen absorption, the situation is more complicated, which depends on the difference between the total volume of various hydride and non-hydride phases formed after hydrogen absorption of the original hydrogen storage alloy and that of the parent alloy. Therefore, it is difficult to speculate whether there is volume expansion or contraction.

iii. *On the pulverization in the process of hydrogen absorption/desorption*

For the alloy with hydrogenated solid solution as the main body of hydrogen absorption, because the hydrogen atom enters the interstitial position of the parent phase lattice, the matrix will introduce micro-stress (micro-strain) and macroscopic strain. If the sum of the two strains exceeds the yield stress of the original hydrogen storage material, the original grains will be refined and the original particles will be pulverized. This refinement and pulverization become more serious with the increase of hydrogen absorption and desorption cycle.

For the alloy with hydride as the main body of hydrogen absorption, the situation is more complicated. The parent phase of the original alloy is decomposed and the multiphase hydride phase is formed, and their grain size and particle size are closely related to the temperature of hydrogen absorption. Generally speaking, the higher the temperature is, the faster the hydride nucleation is, and the grains and particles are relatively small. Similarly, the refinement and pulverization become more and more serious with the increase of hydrogen absorption and desorption cycle.

b) Conclusion

Through the introduction of the above section 2-5 and the above comprehensive analysis, the following conclusions are drawn:

(1) At lower temperature, the hydrogen absorption kinetics curves of the two kinds of materials at different hydrogen pressure show that the initial hydrogen absorption rate and saturated hydrogen absorption capacity increase with the increase of hydrogen pressure.

However, when the temperature is too high, the hydrogen storage materials that store hydrogen by

hydride will still show the above situation, while the hydrogen storage materials that store hydrogen by hydrogenated solid solution may seriously affect the exothermic effect of hydrogenated solid solution because of too high temperature. will not fully show the above.

(2) The kinetic curve of hydrogen absorption at different temperatures at lower hydrogen pressure, the hydrogen storage materials with hydride as the main body show that the initial hydrogen absorption rate and saturated hydrogen absorption capacity increase with the increase of temperature, while the materials with hydrogenated solid solution hydrogen storage show that the initial hydrogen absorption rate and saturated hydrogen absorption capacity decrease with the increase of temperature, which is due to the serious influence of high temperature on the exothermic effect of the system. Similarly, when the hydrogen pressure is too high, the two kinds of hydrogen storage materials may have cross scenarios. Fig. 14 shows the hydrogen absorption curve of Mg hydrogen storage alloy catalyzed by 1 mol% Nb_2O_5 [14]. At lower hydrogen pressure (0.2Mpa), the initial hydrogen absorption rate and saturated hydrogen absorption capacity increase with the increase of temperature. However, when the hydrogen pressure is 1.0Mpa, the initial hydrogen absorption rate and hydrogen absorption capacity of 250°C are lower than that of 150°C (30 seconds ago), and when the hydrogen pressure is 3.0Mpa, there is a cross scenario.

With the emergence of new alloy hydrogen storage materials, the two kinds of alloy materials with hydride as hydrogen storage body and hydrogenated solid solution as hydrogen storage body will have new development, and there may be mixed hydrogen storage materials with both of them, just like the aforementioned Mg-Cu hydrogen storage alloy, in which Mg_2Cu phase decomposes and then forms MgH_3, while $MgCu_2$ phase belongs to Laves phase, which may form hydrogenated solid solution in the process of hydrogen absorption.

In addition, hydrogen storage materials with surface adsorbed hydrogen as the main body, such as microporous / mesoporous hydrogen storage materials, may appear.

It is suggested that attention should be paid to the test and analysis of the newly developed hydrogen storage materials in the following aspects:

(1) Carry out the identification of the existing phases of the original hydrogen storage materials, analyze and study the crystal structure characteristics of these phases, and search the PCPDFw in database for the existence of related hydride and its diffraction data.

(2) When studying the kinetics and thermodynamics of hydrogen absorption and desorption of materials, special attention should be paid to the structural evolution and microstructure changes of the original phase of hydrogen storage materials in the process of hydrogen absorption and desorption. From the XRD analysis experiment introduced in section 3, it can be seen that the XRD analysis sample did not do any special treatment. It seems that when the contribution of surface adsorption to hydrogen storage can be ignored, it is not necessary to make on-line (in situ) XRD analysis, but can be sampled in each stage of hydrogen absorption and desorption, because the hydride and hydrogenated solid solution are quite stable, and when the experimental results show that there is no phase transition, special attention should be paid to the displacement, broadening and relative strength of the diffraction lines. When carrying out this kind of test and analysis, if there are conditions, it is best to use neutron diffraction technology, because the scattering factor of X-ray of H and metal is very different, and the contribution of H atom to X-ray diffraction intensity is very little. On the other hand, there is a small difference in the scattering factor between H and metal, which can show the contribution of H atom to the diffraction intensity.

(3) The performance of hydrogen absorption-desorption cycle is very important. The 2015 hydrogen storage target of the United States Department of Energy stipulates that it should have the capacity of 1500 cycles of hydrogen absorption and desorption cycle. While studying the cycle performance and cycle performance attenuation, attention should be paid to the test, analysis and study of the changes of crystal structure, fine structure and microstructure parameters of hydrogen storage materials with the cycle cycle according to the methods introduced in chapters 14 and 15 of this book. in order to explore the reasons for the decline of cycle performance and provide ideas for improving the cycle performance of alloy hydrogen storage materials.

The above recommendations also seem to be necessary for developed/applied hydrogen storage materials, especially for typical hydrogen storage materials.

References Références Referencias

1. Fan Shifeng, Research Progress of Metal hydrogen Storage Materials, Chemical propellants and Polymer Materials, 2019; Inner Mongolia rare Aoko hydrogen Storage Alloy Co., Ltd., Metal hydrogen Storage Materials and their applications, 2010.
2. Zhu Min, Editor in Chief, introduction to Advanced hydrogen Storage Materials, Science Press, 2015.6.
3. Darren P. Broom, translated by Liu Yongfeng, etc., hydrogen storage materials: characterization of

hydrogen storage properties, Machinery Industry Press, 2013, p.107.

4. Jai Young Lee, S. M. Byun, C. N. Park and J. K. Park, A Study of the Hydriding kinetics of TiFe and its alloys, *Journal of the Less-Common Metals, 87* (1982) 149 – *164*
5. J. L. Stakebake, *J. Electrochem. Sot., 126* (1979) 495.
6. Wajid Ali, Mingyang Li, Pengyue Gao et. al., Hydrogenation properties of Ti-Fe-Mn Alloy with Cu and Y as additives, International J. Hydrogen energy, 2016.
7. Huang Taizhong, hydrogen storage properties and phase structure of TiCr-based alloys, doctoral thesis of Shanghai Institute of Microsystems and Information Technology, Chinese Academy of Sciences, 2005.
8. Huang Taizhong, Wu Zhu, Xu Naixin, Structure and properties of TiCrMo ternary hydrogen storage alloys, Chinese Journal of Nonferrous Metals, 2006 jue 16 (11):1855-1860
9. Lu Manqi, Qi Zhenzhong, Wu Pingsen, study on the kinetics of hydrogen absorption process of LaNi5, Acta Metallica Sinica, 1980 pr 16 (1): 65 Jun 71
10. Cao Da-li, Chen De-min2, Liu Yi, Ma Lei, Lu Man-qi, Yang Ke, Structure and hydrogen storage performance of $LaNi_{4.25}Al_{0.75}$ alloy, Trans. Nonforrous. Met. Soc.,China, 2011,21:517～522 ;
11. Percheron-Gueganan A., Latigue C. and Achard J.C. et al, Neutron and X-ray diffraction Profile Analysis and Structure of $LaNi_5$,, $LaNi_{5-x}Al_x$, AND $LaNi_{5-x}Mn_x$Intermetallics and Their Hydrides (Deuterides), J. Less-Common Metals, 1980,74: 1 – 12.
12. Effect of Al content of Zhang Ruijing, LV Manqi, Cao Li, Chen Demin, Yang Ke and LaNi5-xAlx alloys on hydrogen absorption capacity and equilibrium hydrogen pressure, Rare Metals, 2004. 28 (4): 678. 682.
13. Tai Yang, Zeming Yuan, Wengang Bu, et al., Evolution of the phase structure and hydrogen storage thermodynamics and kinetics of $Mg_{88}Y_{12}$ binary alloy, International J. Hydrogen Energy, 2016, 41(4):2689～2699.
14. Z.W.Wu, Y.T. Li, Q. A. Zhang,et.al., Catalytic effet on nanostructured Mg_2Ni and YH2/YH3 on hydrogen absorption-desorption kinetics of Mg-Cu-H system, J. Alloy and Compounds,2016,685:639～644.
15. Nobuko Hanada1, Takayuki Ichikawa , Hironobu Fujii, Hydrogen absorption kinetics of the catalyzed MgH_2 by niobium oxide, Journal of Alloys and Compounds 446–447 (2007) 67–71.
16. Edited by Hu Zilong, hydrogen Storage Materials, Chemical Industry Press, 2002.
17. DajiaoTaizhang, translated by Wu Yongkuan, Properties and applications of Metal hydrides, Chemical Industry Press, 1990.
18. L.Schlapbach (*ed*.), Hydrogen in Intermetallic Compounds (I and II), Springer- Verlag, Berlin, Herderberg, New York, 1988 and 1992.
19. International committee of Diffraction Data (ICDD), Powder Diffraction file(PDF), USA.
20. Yang Chuanzheng, XieDacai, Chen Guizun, Zhong Fumin, Phase diffraction Analysis, Metallurgical Industry Press, 1989.
21. Jiang Chuanhai, Yang Chuanzheng, X-ray diffraction and scattering Analysis of Materials, higher Education Press, 2010.
22. Huang Xiaoping, Pang Yanrong, Yang Liying, "Progress in non-destructive testing of hydrogen storage alloys during hydrogen absorption and desorption", rare metals and cemented carbide. 2013, 41 (2): 4952
23. E.MacA. Gray*, C.J. Webb, In-situ diffraction techniques for studying hydrogen storage materials under high hydrogen pressure, International J. hydrogen energy, 2012, 37:10182～10195
24. Cheng Honghui, Li Kang, Han Xingbo, a testing device of in situ synchrotron radiation X-ray diffraction for hydrogen storage alloy during hydrogen absorption and desorption, 2013 patent.
25. Roman V Denys, Andrey A. Poletaev, Jan PetterMaehlen et al, Nanostructured rapidly solidified $LaMg_{11}Ni$ alloy. II. In situ synchrotron X-ray diffraction studies of hydrogen absorptione-desorption behaviours, Inter. J. Hydrogen Energy, 2012, 37: 5710～5722.
26. Kalinichenka S, Rontzsch L, Baehtz C, et al, Hydrogen desorption properties of melt-spun and hydrogened Mg-based alloys using synchrotron X-ray and TGA, J. Alloys Compounds, 2011, 509(S2): 629～632.
27. Kalinichenka S, RontzschbL, Baechtz C, et al, Hydrogen desorption kinetics of melt-spun and hydrogenated$Mg_{90}Ni_{10}$ and $Mg_{80}Ni_{10}Y_{10}$ using synchrotron, X-ray diffraction and thermogravimetry, Journal of Alloys and Compounds 496 (2010) 608–613.
28. Hu Yeqi, preparation and Hydrogenation behavior of mg-based and TiCr2 hydrogen Storage Materials, Ph. D. thesis, Institute of Metals, Chinese Academy of Sciences, 2004.
29. C. Stana, K. Asanob, K. Sakakib, et al, In situ XRD for pseudo Laves phases hydrides highlighting the remained cubic structure, Inter. J. Hydrogen Energy, 2009, 34: 3038 – 3043
30. Pebler A. and Gulbransen E. A., 'I'runs. AIME, 239 (1967) 1593.
31. Shaltiel D., Jacob I. and Davidov D., J. Less-Common Met., 53 (1977) 117 - 131.

32. Jacob I., Shaltiel D., Davidov D. and Miloslavski I., Solid State Commun., 23 (1977)672.
33. Johnson J. R. and Reilly J. J., Inorg. Chem., 17 (1978) 3103.
34. Jacob I. and Shaltiel D., Solid State Commun., 27 (1978) 175.
35. J Didisheim. J., Yvon K., Shaltiel D., Fischer P., Bujard P. and Walker E., Solid State Commun., 31 (1979) 47.
36. J Didisheim. J., Yvon K., Shaltiel D., Fischer P., Bujard P. and Walker E., Solid State Commun., 32 (1979) 1087.
37. Yuan Zhiqing, "study on the microstructure of AB5 type hydrogen storage alloy and its hydride by X-ray diffraction", doctoral thesis of Zhejiang University, 2004.
38. Yuan Zhiqing, Lu Guanglie, Zeng Yuewu et al., study on crystal structure and microstructure of ternary hydrogen storage alloy La (Ni,Sn) 5hydx (xylene 0.1-0.3), metalJournal, 2004, 40 (8):
39. Li Yuxia, Yang Chuanzheng, Lou Yuwan, Xia Baojia, study on the physical mechanism of conductivity in the charge-discharge process of MH/Ni batteries, Journal of Chemistry, 2009.67 (9): 901-909.
40. Yang Chuanzheng, Lou Yuwan, Xia Baojia, Chemical and physical phenomena and Mechanism of Ni-MH Battery during charge and discharge, Jishou University Journal (Natural Science Edition), 2009.30 (6): 54 / 58.
41. Yang Chuanzheng, Lou Yuwan, Zhang Jian, XieXiaohua, Xia Baojia, material characterization and electrode process mechanism of green secondary battery, Science Press, 2015; Materials and Working Mechanism of Secondary Batteries, Springernature, and Science Press Beijing, 2023
42. Percheron-Gueganan A., Lartigue C. and Achard J. C., et al, Neutron and X-ray Diffraction Profile Analysis and Structure of $LaNi_5$,$LaNi_{5-x}$Alx and $LaNi_{5-x}Mn_x$Intermetallics and Their Hydrides (Deuteides) J. Less-Common Metals, 1980,74: 1 – 12
43. Endo D, Sakaki K, Akiba E, Lattice expansion for $RTNi_{4.30-x}Co_xAl_{0.30}Mn_{0.40}$(x=0,0.75) studies by in situ X-ray diffraction, Intert. J. Hydrogen Energy, 2007, 32(15):3 435～3 441
44. Nakamura Y, Nakamura J, Iwase K, Distribution of hydrogen in metal hydrides studies by in situ powder neutron diffraction, Nucleon Instrument and Methods in Physics Research A, 2009, 600: 297～300
45. Siarhei Kalinichenkaa, Lars Rontzschb,, Carsten Baehtzc, et al, Bernd Kiebacka, Hydrogen desorption kinetics of melt-spun and hydrogenated $Mg_{90}Ni_{10}$ and $Mg_{80}Ni_{10}Y_{10}$ using in situ synchrotron, X-ray diffraction and thermogravimetry, J. Alloys and Compounds, 2010, 496 : 608–613
46. SiarheiKalinichenkaa, Lars Rontzschb, Carsten Baehtzc, et al, Hydrogen desorption properties of melt-spun and hydrogenated Mg-based alloys using in situ synchrotron X-ray diffraction and TGA,J. Alloys and Compounds, 2011, 509S: S629–S632.
47. Zhang Taiping, calculation of the utilization rate of the densest packing space of three types of metal crystals, Journal of higher correspondence (Natural Science Edition), 2003, 16 (6): 30～32.
48. Charles B. Magee, James Liu and Charles E. Lundin, Relationships Between Intermetallic Compound Structure and Hydride Formations, Journal of the Less-Common Metals, 1981,78: 119～138
49. Cao Da-li, Chen De-min2, Liu Yi, Ma Lei, Lu Man-qi, Yang Ke, Structure and hydrogen storage performance of $LaNi_{4.25}Al_{0.75}$ alloy, Trans. Nonforrous. Met. Soc.,China, 2011, 21:517～522;
50. Yuan Manxue, Han Jianwen, Lai Chengming, theoretical study of hydrogen storage state in LaNi5 hydrogen storage materials, Journal of Nankai University (Natural Science), 1998, 31(1): 840089.
51. Wang Hong, Liu Zuyan, crystallographic Analysis of maximum hydrogen Storage capacity of LaNi5, rare Metal Materials and Engineering, 2004.
52. Bowman A L.,Anderson J L,Merson N G. Proc. 10th Rare Earth Reseach Conf., Carefree,AR,1973:485.
53. Yartis V A., Burnasheva V VSemenko K N et al, Int. J. Hydrogen Energy, 1982, 7:957.
54. Percheron-Gguegan A., Lartigue C and Achard J C., J. Alloys Comp.,1980,74:1 .
55. Latroche M, et al., J. Alloys Comp.,1999, 293-295: 637.
56. Chartouni D, Kuriyama N, Otto A,et al., J. Alloys Comp., 1999, 285-295:637.
57. Davenport J.M., Dienes G. J., Johnson R. A., Surface effects on the kinetics of hydrogen absorption by metals ,Phys. Rev.,1982, 25(4):2165～2147.
58. Zhang Xiulan, Huang Zhi, Chen Bo, et al., Thermodynamic Analysis of LaNi5 hydrogen Storage process, Journal of Physics, 2007 ,56 (7): 4039 04043.

Global Journal of Science Frontier Research: a Physics and Space Science
Volume 23 Issue 3 Version 1.0 Year 2023
Type: Double Blind Peer Reviewed Interenational Research Journal
Publisher: Global Journals
Online ISSN: 2249-4626 & Print ISSN: 0975-5896

Effect of Wind Velocity on Transport and Distribution of Co_2 Fluxes at a Tropical Location, Ile-Ife, Southwest Nigeria

By Adewale I. Ajao, Oluseyi E. Akinola & Olawale E. Abiye

Obafemi Awolowo University

Abstract- This study investigated effect of wind velocity on CO_2 fluxes at a tropical location, Ile-Ife, southwest Nigeria. Half-hourly averaged flux data acquired by eddy covariance measurements conducted for a complete two-year period (2017-2018) over a grass-covered surface at Obafemi Awolowo University, Ile-Ife, Nigeria was analyzed. The results showed that CO_2 fluxes increased rapidly from sunset to sunrise due to stable boundary layer and nighttime soil respiration. Large transport of CO_2 fluxes was very prominent in the early morning when winds were strong and large air-masses leaving the site. Consequently, CO_2 concentration dropped as convective activities kicked off, enhancing photosynthesis. CO_2 flux and concentration exhibited good linear relationships with relative humidity but strong inverse correlations with temperatures and radiations at the site. The dominant wind flow in the area, southwesterly was largely responsible for transport and distribution of fluxes. The study concluded that wind velocity has little or no significant influence on the transport and distribution of CO_2 fluxes, particularly at nighttime. This may be attributed majorly to low frequency distribution of winds in the area.

Keywords: *CO_2 fluxes; wind velocity; frequency distribution; southwesterly; tropical location.*

GJSFR-A Classification: *LCC: QC879.7 .N6*

Strictly as per the compliance and regulations of:

Effect of Wind Velocity on Transport and Distribution of Co_2 Fluxes at a Tropical Location, Ile-Ife, Southwest Nigeria

Adewale I. Ajao [α], Oluseyi E. Akinola [σ] & Olawale E. Abiye [ρ]

Abstract- This study investigated effect of wind velocity on CO_2 fluxes at a tropical location, Ile-Ife, southwest Nigeria. Half-hourly averaged flux data acquired by eddy covariance measurements conducted for a complete two-year period (2017-2018) over a grass-covered surface at Obafemi Awolowo University, Ile-Ife, Nigeria was analyzed. The results showed that CO_2fluxes increased rapidly from sunset to sunrise due to stable boundary layer and nighttime soil respiration. Large transport of CO_2 fluxes was very prominent in the early morning when winds were strong and large air-masses leaving the site. Consequently, CO_2concentration dropped as convective activities kicked off, enhancing photosynthesis. CO_2flux and concentration exhibited good linear relationships with relative humidity but strong inverse correlations with temperatures and radiations at the site. The dominant wind flow in the area, south westerly was largely responsible for transport and distribution of fluxes. The study concluded that wind velocity has little or no significant influence on the transport and distribution of CO_2 fluxes, particularly at nighttime. This may be attributed majorly to low frequency distribution of winds in the area.

Keywords: CO_2 fluxes; wind velocity; frequency distribution; southwesterly; tropical location.

I. Introduction

Carbon dioxide (CO_2) is a trace gas in the atmosphere (≈ 0.04 %) which primarily comes from natural processes such as volcanic eruptions, forest fires, decayed organic matter etc. Its continuous emissions have increased largely as a result of unstoppable anthropogenic activities such as burning of fossil fuels, deforestation and energy consumption leading to increase in its concentration and eventually result to global warming across the nations of the world (IPCC 2001; IPCC 2006; Dietz et al., 2009; Rahaman et al., 2011;Van Den Hende et al., 2012; Cheah et al., 2014; Wilbanks and Fernandez, 2014).The concentration of atmospheric CO_2 has increased to an annual average of 407 ppm reported for 2018 (NOAA, 2019).

Transport and distribution of such emissions to short-and long-range distances, therefore depend on the prevailing atmospheric conditions at any location on the surface of the earth (Ncipha et al., 2020).Turbulent transport of a major greenhouse gas such as CO_2 both on spatial and temporal scales determines to a large extent, its mixing and distribution to various parts of the environment where it can be utilized (Smallman et al., 2014; Liu et al., 2017; Zhao et al., 2018). Its distribution in turn determines and influences the climatic conditions which directly or indirectly affect organisms inhabiting in such environment (IPCC, 2007; Stoy et al., 2009; Jung et al., 2011; Vasumathi et al., 2017). Many Organisms on land, in the sea or in the atmosphere survive much better in weather-friendly environments than they do in harsh environmental conditions. Existence and survival of such organisms, particularly photo auto trophstherefore depend solely on availability and distribution of $CO_2$for the regulation of plants' metabolic activities as well as the environment which they rely on for survival(Houghton, 2000; Malhi and Grace, 2000; Bubier et al., 2003; Canadell et al., 2007; IPCC, 2007; Lindroth et al., 2007; Nithiya et al., 2017).

Studies have been conducted in the temperate region, both in the rural and urban are as to check the alarming rate of production, transport and distribution of CO_2emissions as it contributes immensely to global warming and measures are being put in place to check it, but little efforts have been made so far in the tropics in ensuring safety of lives from the effects of the menace which are posed on the important creatures in the region (van Gorsel et al., 2007; Schimel et al., 2008, Kosugi et al., 2008; van Gorsel et al., 2009; Rebmann et al., 2009; Hernández-Paniagua et al., 2015). This is due to the absence of meteorological/FLUXNET stations dedicated to measuring accurate and consistent flux exchanges of mass of CO_2, water vapour and energy between the biosphere and the atmosphere (Baldocchi et al., 2001; Baldocchi, 2008; Novick et al., 2017; Villa et al., 2019). Moreover, the circumstance is attributed to non-availability/inadequacy of measuring devices for mass and energy fluxes, prohibitive costs of procurement of the devices and low expertise in the analysis of such fluxes data (Chiemeka, 2008; Ayoola et al., 2014; Soneye et al., 2019; Ajao et al., 2020).An integrative approach to measure CO_2 in vertical and horizontal soil profiles over a semiarid ecosystem at a shrubland plateau in southeast Spain by Sánchez-Cañete et al. (2016) showed that wind increased CO_2

Author α σ: Department of Physics and Engineering Physics, Obafemi Awolowo University, Ile-Ife, Nigeria. e-mails: a.ajao@oauife.edu.ng, iyiolamercy2005@yahoo.com
Author ρ: Center for Energy Research and Development, Obafemi Awolowo University, Ile-Ife, Nigeria.

concentration underneath plant soil and induced its depletion on bare soil. The study further revealed that wind is capable of inducing CO_2 transport in the surface soil and bedrock but not in subsurface. Temporal variability of carbon dioxide fluxes investigated in the city center of Arnhem, Netherlands by Kleingeld et al. (2018) revealed that CO_2 emissions from space heating dominated winter period while emissions from traffic dominated summer period in the area. A study on seasonal and diurnal variation of CO_2 in a mountainous area in Seoul, South Korea investigated by Ghosh et al. (2010) showed that many meteorological variables exhibited inverse correlation with CO_2 concentration but wind speed and direction are found to have less impact on the concentration in the area. Continuous measurements of CO_2 fluxes at the former radio tower in Beromünster, Switzerland by Satar et al. (2016) showed that CO_2 mixing ratios decreased with sunrise due to its uptake by plants for photosynthesis, and disappearance of nocturnal boundary layer as the conditions became unstable while the mixing ratio increases when convective activity ceases resulting in surface cooling. The study further revealed that CO_2 seasonal variation could be associated with biological activity in the area. Eddy covariance measurements of mass flux of CO_2 and its concentration over a leguminous plant (Cowpea) at an agricultural site in Ile-Ife, Nigeria by Ajao and Jegede (2019) identified photo synthetically active radiation (PAR) among other atmospheric variables as the dominant factor regulating CO_2 exchange at the site, particularly during the day. This paper investigates diurnal variation of wind speed and direction, and CO_2flux with its associated concentration over a grass-covered surface at an agricultural site located on the campus of Obafemi Awolowo University, Ile-Ife, Nigeria. The primary objective of the study is to establish whether there is a significant correlation between wind velocity and fluxes of $CO_2$with its associated concentrations in the area.

II. Materials and Method

a) Site description

The experimental site (OAU Met-station), shown in the Fig. 1, is situated within the Teaching and Research Farm of Obafemi Awolowo University (TRF-OAU) in Ile-Ife, southwest Nigeria (7.52°N; 4.52°E; 298 m a.m.s.l). The research farm is 7 km in the northeastern direction from the main campus, and covers about 5 hectares. It is surrounded by low hills to the eastern and southern part of the campus. It is located in the tropical rainforest zone and characterized by two major alternating seasons which are wet and dry respectively. The wet season spans from April to October while the dry season comprises December, January and February. March and November are referred to as transition months. The former is the transition from dry-to-wet season while the latter is from wet-to-dry season. The annual precipitation for Ile-Ife is between 1000 and 1500 mm. The soil type in the area is sandy-clay-loamy from the top to the bottom (0 – 0.1 m). Portions of the farmland are planted with food crops of different kinds cultivated by research students and staff of the Faculty of Agriculture. A few scattered trees including palm trees are also planted. Some portions are allotted as project sites to the International Institute of Tropical Agriculture (I. I. T. A.) and Institute of Agricultural Research and Training (I. A. R & T) for yearly planting of maize and other arable crops. Offices for staff members and other facility buildings (stores and warehouses)are available at the farm site. There are also lecture theatres for the use of students in their final year, where lectures, seminars and other academic activities apart from farm work are observed. The experimental site is a clear open field and it appears relatively homogeneous. The surface is grass-covered and mown once every two weeks to ensure homogeneous conditions (see Fig. 2). Additionally, in a bid to ensure constant fetch, particularly for a measurement of this nature, the site is situated in a secure and an undisturbed location that is distant away from the farm center and forested region within the farm to prevent any obstruction to surface flow. The mean surface wind at the site is low and the direction is almost constant throughout the year. As such, the flux footprint does not really change over time as a result of almost constant frequency distribution of wind in the area. Meteorological facilities were installed within the experimental site which is 18 square meters in area. The area was fenced using open-wire net to prevent any unnecessary intrusion, especially by rodents from destroying the sensors' cables. Aside electricity supply to the site, alternative power supplies from a 2.5 KVA inverter and a 6.5 KW gasoline-engine generator were made available to ensure constant running of the meteorological station. From 2004 to date, the meteorological station (OAU Met-station) is maintained by members of the Atmospheric Physics Research Group (APRG) at the department of Physics and Engineering of Obafemi Awolowo University, Ile-Ife, Nigeria.

b) Eddy Covariance (EC)measurements at T&R Farm, OAU, Ile-Ife

Eddy covariance (EC) technique was employed to acquire turbulent flux data in this study as it allows direct, continuous, long-term and local-scale measurement of land-surface atmosphere flux exchanges of mass (CO_2), momentum and energy on spatial and temporal scales respectively by deriving the covariance between the vertical wind speed and the mixing ratios of other flux parameters (Aubinet et al., 2000; Baldocchi, 2003; Järvi et al., 2012; Kotthaus and Grimmond, 2012; Liu et al., 2012, 2014; Christen, 2014; Weissert et al., 2014; Goulden et al., 2006; Hong et al.,

2008). The instrumentation at the study site comprises: a three-dimensional ultra-sonic anemometer (CSAT3; Campbell Scientific Inc. Logan, Utah, USA) to measure high frequency wind velocity components (i.e., *u*, *v*, and *w*) and an open path infrared gas analyzer (LI 7500; LiCor Inc., Lincoln, Nebraska, USA) to measure high frequency signals of water vapor density and CO_2 flux. The EC system set up shown in the Fig. 2 was mounted at 1.8 m on a 2.2 m tall mast above the ground surface (a.g.l). Incorporated in the EC system was a temperature-humidity probe (Vaisala HMP60; Campbell Scientific Inc. Logan, Utah, USA) to measure air temperature and relative humidity respectively at the site. Turbulent fluxes of mass (CO_2), momentum and energy were recorded at a sampling rate of 10 Hz and averaged over 30 mins periods by the EC system. The raw dataset was subjected to Quality Assurance and Quality Control (QA/QC) protocol. Stationarity test was performed on the data following the procedure by Foken and Wichura (1996). All turbulent fluxes were computed using Loggernet software and reduced to 30-min averages for the purpose of analysis. The data acquisition software (DAS) from Campbell Scientific Inc. (Campbell Scientific 2010) contains flags which identify and remove spurious/bad data values. Incorporated in the software are the Webb-Pearman-Leuning correction, frequency response correction, crosswind contamination correction, correction for cosine response and others. Additionally, cases of missing data values of fluxes and concentrations of $CO_2$and other turbulent parameters constituted less than 2 % of the overall datasets and as such, no serious data jumps were observed in the whole time series (Ajao et al., 2020). Interpolation approach was used where necessary to fill the limited missing data points which were observed in the datasets. Two Campbell Scientific programmable data loggers (model CR1000) were used to retrieve data from the sensors, and downloading of data was done twice a week via USB-to-Serial cable connection to a dedicated laptop computer. The downloaded data were subsequently transferred to a desktop computer for storage/archiving and further analysis. Microsoft Excel and MicroCal origin (version 2018) were used in reducing further the dataset for the purpose of analysis. From the reduced dataset, daily patterns of CO_2 fluxes and concentration, wind speed and direction and some other meteorological variables were plotted and examined for possible correlations.

c) Ancillary measurements at T & R Farm, OAU, Ile-Ife

Aside EC measurements, supporting meteorological variables of relevance to the study: global and net radiation, air and soil temperatures, relative humidity, soil heat flux, soil moisture and rainfall were acquired at the site. A four-component net radiometer (model NR01, Campbell Scientific Inc. Logan, Utah, USA) which measures radiation components and an integrated net radiometer (NR-LITE, Campbell Scientific Inc. Logan, Utah, USA) were placed side by side for comparison purposes on a 1.7 m tall mast. Additionally, on a 6 m mast were other sensors; cup anemometer (model A100L2; Vector Instr., USA)and wind-vane (model W200P) placed at 5.8 m above the surface for measuring wind speed and wind direction respectively, and a pyranometer (model CMR1, Kipp and Zonen, Holland) placed at 2.05 m height for measuring global radiation. Five soil temperature probes (model 108; Campbell Scientific Inc. Logan, Utah, USA) were buried at 0.02 m, 0.05 m, 0.10 m, 0.30 m and 0.50 m for soil temperatures respectively. Two soil heat flux plates (model HFP01; Hukseflux Inc. Logan, Utah, USA) were also buried at 0.05 m and 0.10 m for measuring soil heat fluxes. A water content reflectometer (model CS616; Campbell Scientific Inc. Logan, Utah, USA) was inserted in the soil for measuring volumetric soil moisture content and a rainguage (model TE525,Tipping bucket) to measure the amount of rainfall at the study site. The slow-response sensors' data were sampled at 10 s and averaged every 1-min. They were subsequently reduced to 30-min. averages for the purpose of analyses.

III. Results and Discussion

a) Diurnal variation of CO_2 flux and concentration at the study location

Figures 3 and 4 show the diurnal patterns of CO_2 flux and concentration respectively covering the period of observation; January 2017 to December, 2018 at the study location. From the two figures, it is evident that in the daytime from about 7:30 AM local time (Local time, LT = GMT+1) when surface condition is changing and convective activities are kicking off, air temperature and global radiation increase at the location. This results in a sharp drop in the amount of CO_2 fluxes from about 0.09 $mgm^{-2}s^{-1}$to about −0.52 $mgm^{-2}s^{-1}$recorded around 11:00 AM, which is the minimum flux value observed for the day. The concentration in turn fell from about 803.3 mgm^{-3} in the early morning to about 628.8 mgm^{-3}, being the minimum value recorded around 5:30 PM LT. The drop in the fluxes and concentration values of CO_2 is attributed majorly to distribution and uptake of CO_2 by plant for photosynthesis. From 11:00 PM when minimum fluxes were recorded, the values were almost constant until around 2:30 PM when there was a sudden rise in the amount of the fluxes to about – 0.46 $mgm^{-2}s^{-1}$. The sudden rise in the fluxes may be attributed to intermittent convective cloud drift which blocked out solar radiation reaching the surface, thereby lowering photosynthetic activities. The value continued to rise until around 9:00 PM when the fluxes peaked, about 0.21 $mgm^{-2}s^{-1}$ observed and recorded at the site. Around 6:00 PM LT, the level of CO_2 concentration rose from about 632.0 mgm^{-3} to about 782.0 mgm^{-3}, the

maximum value recorded at 11:00 PM LT. The results indicate that there are time lags between the occurrences of the minima fluxes and concentration values (about 3 hrs), and the peaks (about 2 hrs) of CO_2 at the location. This may be attributed to the influence of possible climatic factors such as "intermittency of incoming solar radiation to the surface by the transient nature of convective clouds in the region." Additionally, the thermodynamic structure of the lower atmosphere in the area may inhibit some ecosystem exchange processes over the time (Ayoola et al., 2014, Ajao et al., 2020). For the occurrences of CO_2 fluxes in different months as observed in the Fig. 3, low fluxes were recorded in the wet months (that is April to October) particularly, during the daytime while large fluxes were recorded in the dry months (that is December, January and February).Consistently in the wet months, CO_2 fluxes were negative in the daytime but positive at nighttime indicating net uptake and release by plants respectively. Fluxes were less negative in the dry months than the wet months. According to Ajao et al. (2020), March and November are classified as transition months. In March, there is transition from dry-to-wet while the reverse is the case for November. Fluxes were less negative during the transition months than some wet months. The level of CO_2 concentration fell below 700.0 mgm^{-3} during the day both in wet and dry months as evident in the Fig. 4, but rose above this value in the night as CO_2 fluxes became positive due to stable boundary layer conditions and increased soil and plant respiration. Maximum and minimum values of CO_2 concentrations observed and recorded in December were 823.3 mgm^{-3} and 628.8 mgm^{-3} respectively. Annual mean and range for the period were 704.4±47.2 mgm^{-3} and 134.5 mgm^{-3} respectively as indicated in the Table 4. Figures 5 and 6 show the 'Box and whisker' plots of half-hourly averaged values of CO_2 fluxes and concentrations from January to December, whose statistical distributions contain the following scores: quartiles (25^{th} and 75^{th} percentiles), median (50^{th} percentiles), mean, minimum and maximum values respectively. From the box plots in Fig. 5, the grouping of the data shows that though the dry months recorded lower range of fluxes than the wet months, fluxes in the dry months were rather less negative than in wet months. Positive monthly mean values were recorded for dry months while wet months recorded negative values. The lowest and highest monthly mean CO_2 flux values, −0.08±0.26 $mgm^{-2}s^{-1}$ and 0.04±0.03 $mgm^{-2}s^{-1}$ were observed and recorded in October and February respectively as indicated in the Table 3. Strikingly in Fig. 6,the lowest and highest inter quartile range (25^{th} – 75th) in concentrations was found in August, 695.5 mgm^{-3} and December, 822.7 mgm^{-3} respectively. The lowest and highest monthly mean CO_2 concentration values, 669.5±24.9 $mgm^{-3}$and 722.3±54.3 mgm^{-3} were observed and recorded in August and October respectively as indicated in the Table 4.

b) Diurnal pattern of Wind speed and Direction at the study location

Diurnal pattern of surface wind speed at the study location in OAU Met-station, Ile-Ife, Nigeria for the observation period: January 2017 to December 2018 is plotted in the Fig. 7. 'It is of importance to note that previous studies by Hayward and Oguntoyinbo (1987) and Jegede (1998) observed and concluded that surface wind flow for Ile-Ife is weak. "The estimated mean surface wind for the area ≈ 1.5 ms^{-1}." Table 1 shows wind categories for the study period as observed at the location. The daily pattern of wind speed observed at the site showed an inverse relationship with CO_2 fluxes. The annual mean wind for the study period was 1.2±0.4 ms^{-1}. In the daytime when the condition was unstable at the location, wind became strong and rose from about 1.0 ms^{-1}around 8:00 AM to reach its peak value of about 2.1 ms^{-1} around 1:00 PM LT. By this time, CO_2 flux had dropped to its minimum value as observed in the Fig. 3. Similarly, in the Fig. 4, concentration value dropped from its peak to minimum. Around 5:30 PM, wind speed became weak and dropped sharply from about 2.0 $ms^{-1}$to its minimum value of about 0.6 ms^{-1} around midnight when both CO_2 flux and concentration had attained their peak values respectively. As such, both parameters displayed inverse relationship with wind speed in the daytime.CO_2 flux displayed little or no fluctuation with wind speed during nighttime whereas concentration showed some degree of fluctuations. For the monthly variation of wind speed as observed in the Fig. 7, surface wind was stronger in the wet months than in the dry months. From midnight till dawn, wind speed was weak (values ranged between 0.5 $ms^{-1}$and 1.0 ms^{-1}) for the months except in July and August when it was relatively weak (slightly above 1.0 ms^{-1}).This may be attributed to strong winds preceding heavy rains recorded in the two months, particularly at nighttime. The monthly mean relative humidity values observed and recorded for July and August were 88.5±8.4 % and 88.7±8.3 % respectivelyas indicated in the Table 3. The observed monthly mean relative humidity value in August (peak of rainy season) was the highest for the period of observation. For daytime period, from about 8:00 AM in each month of the year, the observed surface wind ranged between 1.0 ms^{-1} and 2.0 ms^{-1}. The value dropped from maximum to reach minimum from dusk to about midnight (6:30 PM – 12:00 AM). As such, surface wind was weaker at nighttime than in the daytime at the location. This is adduced to stable boundary layer (calm conditions) at nighttime and unstable conditions during the day. Figure 8 shows wind roses depicting dominant wind flows for the twelve months during the observation period at the study site. For dry months, the dominant

wind flows were south easterlies (SE) while southwester lies (SW) dominated the wet months. In the transition months, winds changed direction from SE to SW in March while SW occurred more often than SE in November (see Table 2). Figure 9 shows 'Box and whicker' plots of wind direction as observed at the location. As evident in the figure, the inter quartile range (25^{th} – 75th) for the dry months were found larger than those in the wet months. Also, the monthly mean wind direction for December and January were less than 150^{o}.

c) *Diurnal pattern of Friction velocity (u*) and its relationship with CO_2 Flux*

Figure 10 shows mean daily cycle of friction velocity (u^*) as observed at the study location.For the study period, surface friction velocity increased in value from dusk (about 7:00 PM) through to midnight till around 3:00 AM due to stable boundary layer conditions, while there was a sharp drop in its value between 4:30 AM and 7:00 A Mas a result of departure of air mass (wind shear)from the site. The daytime fluctuation and rising pattern of $u^*$was due to increase in atmospheric mixing resulting from unstable boundary layer. For the study period, the daily range of u^* was between 0.08 ms^{-1} and 0.18 ms^{-1}. The lowest monthly mean value, 0.12±0.02 $ms^{-1}$was observed and recorded in October and November, while the monthly peak value, 0.15±0.02 ms^{-1} occurred in July and August respectively. In relating friction velocity to CO_2 flux and concentration, it isevident in Fig. 10 that u^* showed inverse relationship with both parameters in the daytime at the location. For nighttime period, the rising and fluctuation of u^* did not really have any significantinfluence on the fluxes and concentration as both parameters seldomly rose, but were almost constant in values. This may be attributed to stable boundary layer at night and low frequency distribution of winds in the area.

d) *Monthly Trends of wind speed, CO_2fluxand concentration at the study site*

Figure 11 shows monthly trends of wind speed, CO_2 flux and concentration for the period of observation. In Fig. 11(a), monthly mean value of wind speed for January was 0.9±0.4 ms^{-1}. The value increased to 1.3±0.4 ms^{-1} in February at the peak of dry season. As the season transited to wet in March through to June, wind speed fell from 1.4±0.5 ms^{-1} to 1.3±0.4 ms^{-1} in June, and then rose through to August, 1.4±0.3 ms^{-1}. The strongest mean wind speed for the period was1.4±0.4 ms^{-1} observed in July. The increase in wind speed values observed for July and August as indicated in the Table 3 may be attributed to strong southwester lies which preceded rains that characterize the period. The observed and recorded value in August dropped sharply to 0.9±0.3 ms^{-1} in October being the weakest mean wind speed for the period. The value was constant until December when it increased a little to 0.9±0.4 ms^{-1}. For monthly variation of CO_2 flux at the site as shown in the Fig. 11(b), monthly mean flux in January was 0.01±0.04 $mgm^{-2}s^{-1}$. The value rose to 0.04±0.03 $mgm^{-2}s^{-1}$ in February. From March through to November, the flux dropped steadily and was almost constant in value until December when it rose. The flux values were negative for wet months but positive for dry months. The positive value of CO_2 flux recorded in dry months is attributed to dryness of surface and less uptake of CO_2 for photosynthesis during the period, as air temperature and global radiation rose from 25.9±6.2°C and 179.0±29.0 Wm^{-2} in January to 28.9±4.8°C and 189.3±40.9 Wm^{-2}in February respectively (see Table 3). Figure 11(c) shows monthly trend of CO_2 concentration at the location. In January, the monthly mean CO_2concentration dropped from 703.9±53.4 mgm^{-3} to 694.6±46.0 mgm^{-3} in February. The drop is attributed to same reason as stated earlier. As the season transited to wet in March, the value rose to 706.0±41.6 mgm^{-3}, and fluctuated steadily through to July until it fell to about 669.5±24.9 mgm^{-3} in August. The minimum mean CO_2 concentration for the period was recorded in August (peak of rainy season). This may be attributed to a break in the rains for some two to three weeks from late July to early August, a phenomenon termed "little dry season (LDS)" experienced within the sub-region of West Africa (Adejuwon, 2012; Ajao et al., 2020). By this period, both air temperature and global radiation fell to their minima values of 25.9±2.0°C and 125.2±63.5 Wm^{-2} respectively while relative humidity peaked at 88.7±8.3 %. The concentration value rose from its minimumin August through to October to attain its peak of 722.3±54.3mgm^{-3}while air temperature fell to 26.1±2.9 °C for the period. As the rains receded and the season transited to dry in November, CO_2 concentration fell to 688.8±21.4 mgm^{-3} due to increased air temperature and surface radiation which enhanced photosynthesis. The value climbed to718.3±71.3 mgm^{-3} in December when temperature and radiation values dropped to about 26.0±5.5°C and 184.7±34.9 Wm^{-2} respectively. The relative humidity also dropped from 79.8±16.8 % to 69.6±22.6 %.The risein CO_2 flux and concentration values coupled with the drop in the values of some major atmospheric variables (i.e. air temperature, relative humidity and global radiation)as observed in December is adduced to surface dryness, presence of strong convective clouds and prominent harmattan cooling from the Sahara desert.

IV. Conclusions

Eddy covariance measurements of fluxes of CO_2 with its associated concentration and other meteorological parameters taken over a grass-covered surface for two consecutive years (2017-2018) at Obafemi Awolowo University, Ile-Ife, southwest Nigeria

have been analyzed to investigate possible effect of wind speed and direction on the transport and distribution of the fluxes in the area.At the study location, diurnal fluctuations of CO_2 flux and concentration varied considerably with patterns of atmospheric transport and heating, particularly in the wet season. From sunrise, a sharp drop in CO_2 fluxes was observed from about 0.2 $mgm^{-2}s^{-1}$ around 7:00 AM LT to reach minimum of about – 0.5 $mgm^{-2}s^{-1}$ around 1:00PMLT due to uptake by plants for photosynthesis. The observed value continued to drop until around 3:00 PM when the fluxes rose steadily through sunset and then into the nighttime. The fluxes fluctuated steadily during nighttime due to stable atmospheric boundary layer conditions and CO_2release via soil respiration. Fluxes of CO_2 were observed to be less negative in the dry season than wet season due to surface dryness and reduced plant activities (cessation of photosynthesis) that characterize the former. Annual mean CO_2 flux and concentration recorded at the location were – 0.03 ± 0.18 $mgm^{-2}s^{-1}$ and 704.4 ± 47.2 mgm^{-3} respectively. The findings in this study are in good agreement with many results earlier obtained for both temperate and tropical climate regions. Of particular interests are the results obtained on the campus of Hokkaido University in Sapporo, Japan by Miyaoka et al. (2007) and those obtained at Dehradun valley in India by Sharma et al. (2013). From the present dataset, inverse correlation existed between wind speed and CO_2 fluxes with its associated correlation during the daytime but little or no significant effects of winds were observed on the fluxes at nighttime.

Acknowledgements

The authors are thankful to members of Atmospheric Physics Research Group (APRG) and staff of technical unit at the Department of Physics and Engineering Physics of Obafemi Awolowo University, Ile-Ife, Nigeria for their support during the conduct of the field experiment. They are grateful to the editor and reviewer(s) who provided insightful and constructive comments that helped in improving the study. This research did not receive any specific grant from funding agencies in the public, commercial, or not-for-profit sectors, but the CO_2flux measurements (from eddy covariance system) have been sustained since 2016 in a group led by Prof. Oluwagbemiga O. Jegede.

Declaration of Interest statement

The authors declared that they have no known competing financial interests or personal relationships that could have appeared to influence the work reported in this paper.

Funding Statement

The Nigeria Micrometeorological Experiment (NIMEX) project led by Prof. Oluwagbemiga Jegede has been responsible for the running and maintenance of the Obafemi Awolowo University meteorological station (OAU-Metstation) since 2014.

Author's Contribution

All authors contribute to the study conception and design. Material preparation, data collection and analysis were performed by Dr. Adewale Iyiola Ajao. The first draft of the manuscript was written by Dr. Adewale Iyiola Ajao, and all authors commented on previous versions of the manuscript. All authors read and approved the final manuscript before final submission was made.

Data Availability

The data for this study will be made available to any individual or organization on reasonable requests via a.ajao@oauife.edu.ng or iyiolamercy2005@yahoo.com.

Ethics approval

The manuscript is a result of the research ongoing at the Obafemi Awolowo University Ile-Ife, southwest Nigeria. The work reported here is in its original form and has not been submitted or published elsewhere. Proper acknowledgements have been given to all the works consulted in the course of its preparation.

Consent to Participate

All authors are core members of the Atmospheric Physics Research Group (APRG) at the department of Physics and Engineering Physics, and Center for Energy Research and Development (CERD) in Obafemi Awolowo University (OAU), Ile-Ife, southwest Nigeria. The group has been responsible for the maintenance and running of the existing meteorological station in OAU, where the data for the study was acquired. No human or animal participation was directly involved in the research.

Consent for Publication

All authors agreed with the content of the final copy of the manuscript, and appropriate authorities were consulted and acknowledged before the work was submitted to the Journal.

References Références Referencias

1. Abiye, O. E., Ajao, A. I., Borisade, A. O., Akinola, O. E., Sunmonu, L. A. and co-authors. 2019. A simple meteorological preprocessor (SIMETPRO) for optimizing hands-on application of air pollution dispersion models in limited data scenarios. *Ife Journal of Science,* 21(2), 389-399. https://dx.doi.org/10.4314/ijs.v21i2.12
2. Adejuwon, J. O. 2012. Rainfall seasonality in the Niger Delta Belt, Nigeria. *Journal of Geography and Regional Planning,* 5, 51–60. https://doi.org/10.5897/JGRP11.096

3. Ajao, A. I. andJegede, O. O. 2019. Eddy-Covariance Measurement of CO_2 Concentration and Turbulent Flux above Cowpea (*Vigna unguiculata (L.) Walp*) at an Agricultural Site in Ile-Ife, Nigeria. *Ife Journal of Science*, 21(1), 61-72. https://dx.doi.org/10.4314/ijs.v21i1.5
4. Ajao,A. I.,Jegede,O. O. and Ayoola, M. A. 2020. Diurnal and seasonal variability of sensible and latent heat fluxes at an Agricultural site in Ile-Ife, southwest Nigeria. *Theoretical and Applied Climatology*, 139(3-4), 1237–1246, doi: 10.1007/s00704-019-03043-z
5. Aubinet, M., Grelle, A., Ibrom, A., Rannik, Ü., Moncrieff, J. and co-authors. 2000. Estimates of the annual net carbon and water exchange of forest: The EUROFLUX methodology. *Advance Ecology Resources*, 30, 113–175.
6. Ayoola, M. A., Sunmonu, L. A., Bashiru, M. I.andJegede, O. O. 2014. Measurements of Net-All Wave Radiation at a Tropical Location, Ile-Ife, Nigeria. *Atmosfera*, 27, 305-315.
7. Baldocchi, D. D., Falge, E., Gu, L., Olson, R., Hollinger, D. and co-authors. 2001. FLUXNET: A new tool to study the temporal and spatial variability of ecosystem-scale carbon dioxide, water vapor and energy flux densities. *Bulletin of American Meteorological Society*, 82, 2415–2435.
8. Baldocchi, D. D. 2003. Assessing the eddy covariance technique for evaluating carbon dioxide exchange rates of ecosystems: past, present and future. *Global Change Biology*, 9, 479–492.
9. Baldocchi, D. D. 2008. 'Breathing' of the terrestrial biosphere: lessons learned from a global network of carbon dioxide flux measurement systems. *Australian Journal of Botany*., 56, 1–26.
10. Bubier, J., Crill, P.,Mosedale, A., Frolking, S. andLinder, E. 2003. Peatland responses to varying interannual moisture conditions as measured by automatic CO_2 chambers. *Global Biochemical Cycles,*17, 1066–1081.
11. Campbell Scientific. 2010. Open Path Eddy Covariance (OPEC) System for determination of surface turbulent fluxes: Operator's manual – CSAT3, LI 7500 and KH20. Campbell Scientific, Inc. Utah, Logan, USA, 60 pp.
12. Canadell, J. G., Le Quere, C., Raupach, M. R., Field, C. B., Buitenhuis, E. T. and co-authors. 2007. Contributions to accelerating atmospheric CO_2 growth from economic activity, carbon intensity, and efficiency of natural sinks, *Proceedings of the National Academy of Sciences, USA*., 104, 18866–18870, doi:10.1073/pnas.0702737104.
13. Cheah, W. Y., Show, P. L., Chang, J-S., Ling, T. C. andJuan, J. C. 2015. Biosequestration of atmospheric CO_2 and flue gas-containing CO_2 by microalgae. *Bioresource Technology*,184, 190-201,http://dx.doi.org/10.1016/j.biortech.2014.11.026
14. Chiemeka, I. U. 2008. Estimation of Solar radiation at Uturu, Nigeria. *International Journal of Physical Sciences,* 3(5), 126-130.
15. Christen, A. 2014. Atmospheric measurement techniques to quantify greenhouse gas emissions from cities. *Urban Climate*.10(P2), 241–260. http://dx.doi.org/10.1016/ j.uclim.2014.04.006.
16. Dietz, T., Gardner, G.T., Gilligan, J., Stern, P. C. and Vandenbergh, M. P. 2009. Household actions can provide a behavioral wedge to rapidly reduce US carbon emissions. *Proc. National Academy of Sciences, USA*.106, 18452–18456.
17. Foken, T. andWichura, B. 1996 Tools for quality assessment of surface-based flux measurements. *Agricultural and Forest Meteorology,*78(1–2), 83-105.
18. Ghosh, S., Jung, K., Chan Jeon, E. andKim, K-H. 2010. Seasonal and Diurnal Trend of Carbon Dioxide in a Mountainous Site in Seoul, Korea. *Asian Journal of Atmospheric Environ*ment, 4-3, 166-176.
19. Goulden, M. L., Miller, S. D. and da Rocha, H. R. 2006. Nocturnal cold air drainage and pooling in a tropical forest. *Journal of Geophysical Research Atmosphere,* 111, 1–14.
20. Hayward, D. F. and Oguntoyinbo, J. S., 1987. The climatology of West Africa. *Rowan and Littlefield*, New York, 271 pp.
21. Hernández-Paniagua, I. V., Lowry, D., Clemitshaw, K. C., Fisher, R. E., James L. France, J. L. and co-authors. 2015.Diurnal, seasonal, and annual trends in atmospheric CO_2 at southwest London during 2000-2012: Wind sector analysis and comparison with Mace Head, Ireland. *Atmospheric Environment*, 105(2015) 138-147.
22. Hong, J., Kim, J., Lee, D. and Lim, J. H. 2008. Estimation of the storage and advection effects on H_2O and CO_2 exchanges in a hilly KoFlux forest catchment. *Water Resources,* 44. doi:10.1029/2007WR006408.
23. Houghton, R. A. 2000. Interannual variability in the global carbon cycle, *Journal of Geophysical Research Atmosphere*, 105, 20121–20130.
24. IPCC. 2001. Climate change, 2001: The scientific basis. Contribution of Working Group I to the Third Assessment Report of the Intergovernmental Panel on Climate Change. Edited byHoughton, J. T., Ding, Y., Griggs, D. J., Noguer, M., van der Linden, P. J. and Xiaosu, D. *Cambridge University Press*, Cambridge, UK.
25. IPCC. 2006. IPCC Guidelines for National Greenhouse Gas Inventories; *United Kingdom Meteorological Office*: Bracknell, UK, 2006.
26. IPCC. 2007. Climate Change 2007: The Physical Basis. Contribution of Working Group I to the Fourth Assessment Report of the Intergovernmental Panel on Climate Change., edited by: Solomon, S., Qin, D., Manning, M., Chen, Z., Marquis, M., Averyt, K. B., Tignor, M., and Miller, H. L., *Cambridge*

University Press, Cambridge, United Kingdom and New York, NY, USA, 2007.

27. Järvi, L., Nordbo, A., Junninen, H., Riikonen, A., Moilanen, J. and co-authors. 2012. Seasonal and annual variation of carbon dioxide surface fluxes in Helsinki, Finland, in 2006–2010. *Atmospheric Chemistry and Physics,* 12, 8475–8489. http://dx.doi.org/10.5194/acp-12-8475-2012.
28. Jegede, O. O. 1998. A field study of the mean surface layer structure in sub-Saharan West Africa: the pre-monsoon (Dry) Season. *Mausam.*49(3), 361–370, 551.510.522:551.553.21(1-926.3).
29. Jung, M., Reichstein, M., Margolis, H. A., Cescatti, A., Richardson, A. D. and co-authors.2011.Global patterns of land-atmosphere fluxes of carbon dioxide, latent heat, and sensible heat derived from eddy covariance, satellite, and meteorological observations, *Journal of Geophysical Research*, 116, 16pp, G00J07, doi:10.1029/2010JG001566.
30. Kleingeld, E., van Hove, B., Elbers, J. and Jacobs, C. 2018. Carbon dioxide fluxes in the city center of Arnhem, A middle-sized Dutch city. *Urban Climate*, 24, 994-1010.
31. Kosugi, Y., Takanashi, S., Ohkubo, S., Matsuo, N., Tani, M. and co-authors. 2008. CO_2 exchange of a tropical rainforest at Pasoh in Peninsular Malaysia. *Agricultural and Forest Meteorology*, 148, 439–452.
32. Kotthaus, S. andGrimmond, C. S. B. 2012. Identification of micro-scale anthropogenic CO_2, heat and moisture sources - processing eddy covariance fluxes for a dense urban environment. *Atmospheric Environment,* 57, 301–316. http://dx.doi.org/10.1016/j.atmosenv.2012.04.024.
33. Lindroth, A., Lund, M., Nilsson, M., Aurela,M., Christensen, T. R. and co-authors. 2007. Environmental controls on the CO_2 exchange in north European mires, *Tellus*,59B, 812–825.
34. Liu, H.Z., Feng, J.W., Järvi, L. andVesala, T. 2012. Four-year (2006–2009) eddy covariance measurements of CO_2 flux over an urban area in Beijing. *Atmospheric Chemistry and Physics,*12, 7881–7892,http://dx.doi.org/10.5194/acp-12-7881-2012.
35. Liu, M., Fu, Y.-L. and Yang, F. 2014. Research progress on urban carbon fluxes based on eddy covariance technique. *Chinese Journal of Applied Ecology,*25(2), 611–619
36. Liu, L., Qu, J., Clarke-Sather, A., Maraseni, T. N. and Pang, J. 2017. Spatial Variations and Determinants of Per Capita Household CO_2 Emissions (PHCEs) in China. *Sustainability*, 9, 1277, 19pp.
37. Malhi, Y. and Grace, J. 2000. Tropical forests and atmospheric carbon dioxide. *Trends Ecology. Evolut*ion,15, 332–337.
38. Miyaoka, Y., Inoue, H. Y., Sawa, Y.,Matsueda, H. andTaguchi, S.2007. Diurnal and seasonal variations in Atmospheric CO_2 in Sapporo, Japan: Anthropogenic sources and Biogenic sinks, *Geochemical Journal*, 41, 429-436.
39. Ncipha, X. G., Sivakumar, V. and Malahlela, O. E. 2020. The Influence of Meteorology and Air Transport on CO_2 Atmospheric Distribution over South Africa. *Atmosphere*, 11, 287; doi: 10.3390/atmos11030287.
40. Nithiya, E. M., Tamilmani, J., Vasumathi, K. K. andPremalatha, M. 2017. Improved CO_2 fixation with Oscillatorial sp. in response to various supply frequencies of CO_2 supply, *Journal of CO_2 Utilization*, 18, 198-205. http://dx.doi.org/10.1016/j.jcou.2017.01.025.
41. NOAA. 2019. The Fourth-Highest Annual growth in the concentration of atmospheric carbon dioxide in 60 years of record-keeping. *Atmospheric CO_2 at Mauna Loa Observatory*, Hawaii. http://www.esrl.noaa.gov.
42. Novick, K. A., Biederman, J. A., Desai, A. R., Litvak, M. E., Moore, D. J. P. and co-authors. 2017. The AmeriFlux network: A coalition of the willing. *Agricultural and Forest Meteorology*., 249, 444 – 456. https://doi.org/10.1016/j.agrformet.2017.10.009.
43. Rahaman, M.S.A., Cheng, L.-H., Xu, X-H., Zhang, L. andChen, H.L. 2011. A review of carbon dioxide capture and utilization by membrane integrated microalgal cultivation processes. *Renewable and Sustainable Energy Reviews*, 15(8), 4002-4012.
44. Rebmann, C., Zeri, M., Lasslop, G., Mund, M. andKolle, O. 2010. Treatment and assessment of the CO_2-exchange at a complex forest site inThuringia, Germany. *Agricultural and Forest Meteorology,* 150(5), 684-691 doi: 10.1016/j.agrformet.2009.11.001.
45. Sánchez-Cañete, E. P., Oyonarte, C., Serrano-Ortiz, P., Yuste, Schulze, E-D., Feigen winter, J. C. and co-authors.2016. Winds induce CO_2 exchange with the atmosphere and vadose zone transport in a karstic ecosystem, *Journal of Geophysical Research Biogeosci*ences, 121, doi: 10.1002/2016JG003500.
46. Satar, E., Berhanu, T. A., Brunner, D., Henne, S. and Leuenberger, M. 2016. Continuous CO_2/CH4/CO measurements (2012–2014) at Beromünster tall tower station in Switzerland, *Biogeosciences*, 13, 2623–2635. doi: 10.5194/bg-13-2623-2016.
47. Schimel, D., Aubinet, M. andFinnigan, J. 2008. Flux measurements in difficult conditions. *Ecology Applications,*18, 1338–1339. Sharma, N., Nayak, R. K., Dadhwal, V. K., Kant, Y. and Ali, M. M. 2013. Temporal Variations of Atmospheric CO_2 in Dehradun, India during 2009, Air, Soil and Water Research, Libertas, *Academica*, 6, 37-45.
48. Smallman, T. L., Williams, M. andMoncrieff, J. B. 2014. Can seasonal and interannual variation in landscape CO_2 fluxes be detected by atmospheric observations of CO_2 concentrations made at a tall

tower? *Biogeosciences*, 11, 735–747. doi:10.5194/bg-11-735-2014.
49. Soneye, O. O., Ayoola, M. A., Ajao, A. I. andJegede, O. O. 2019. Diurnal and seasonal variations of the incoming Solar radiation flux at a tropical station, Ile-Ife, Nigeria. *Heliyon*, Elsevier Publication, 5, 1 – 7. https://doi.org/10.1016/j.heliyon.2019.e01673.
50. Stoy, P. C., Richardson, A. D., Baldocchi, D. D., Katul, G. G., Stanovick, J. and co-authors. 2009. Biosphere-atmosphere exchange of CO_2 in relation to climate: a cross-biome analysis across multiple time scales. *Biogeosciences*, 6, 2297–2312.
51. Van Den Hende, S., Vervaeren, H. and Boon, N. 2012. Flue gas compounds and microalgae:(Bio-) chemical interactions leading to biotechnological opportunities. *Biotechnology Advances*, 30(6), 1405-1424.
52. Van Gorsel, E., Leuning, R., Cleugh, H.A., Keith, H. and Suni, T. 2007. Nocturnal carbon efflux: reconciliation of eddy covariance and chamber measurements using an alternative to the u*-threshold filtering technique. *Tellus Series B-Chemical and Physical Meteorology*, 59(3), 397–403.
53. Van Gorsel, E., Delpierre, N., Leuning, R., Black, A., Munger, J. W. and co-authors. 2009. Estimating nocturnal ecosystem respiration from the vertical turbulent flux and change in storage of CO_2.*Agricultural and Forest Meteorology*, 149, 1919–1930.
54. Vasumathi, K. K., Nithiya, E. M., Pandey, R. and Premalatha, M. 2017. Studies on the effect of wind speed on loss of carbon dioxide during bio sequestration. *International Journal of Hydrogen Energy*. ScienceDirect, Elsevier Journal. 8pp.
55. Villa, J., Ju, Y., Vines, C., Rey-Sanchez, C., Morin, T.H. and co-authors. 2019. Relationships between Methane and Carbon dioxide Fluxes in a Temperate Cattail-dominated Freshwater Wetland, *Journal of Geophysical Research-Biogeosciences*, 124(7), 2076-2089.doi: 10.1029/2019JG005167.
56. Weissert, L. F., Salmond, J. A. and Schwendenmann, L. 2014. A review of the current progress in quantifying the potential of urban forests to mitigate urban CO_2 emissions. *Urban Climate,*8, 100–125. http://dx.doi.org/10.1016/j.uclim.2014.01.002.
57. Wilbanks, T.J. and Fernandez, S. 2014. Climate Change and Infrastructure, Urban Systems, and Vulnerabilities: Technical Report for the US Department of Energy in Support of the National Climate Assessment. NCA Regional Input Reports. *Island Press.*Chapter 4.
58. Zhao, D., Jia, N. and Dong, Y. 2018. Relationship between turbulent energy dissipation and gas transfer through the air-sea interface.TellusB, 70(1), 1528133. http://doi.org/10.1080/16000889.2018.1528133.

List of Figures

Fig. 1: Aerial view of experimental site at the Teaching and Research Farm, Obafemi Awolowo University. Insert is the outline map of Nigeria showing Ile-Ife, southwest Nigeria

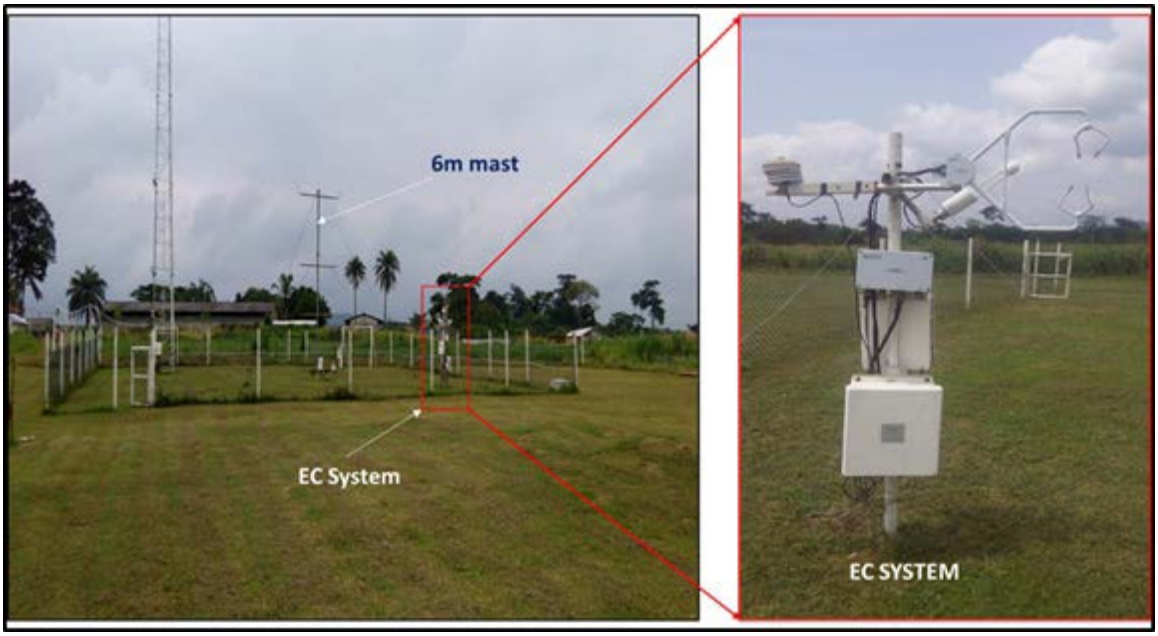

((Image Copyright © Abiye et al., 2019))

Fig. 2: Eddy covariance instrumentation positioned at OAU-Met station, Ile-Ife, Nigeria (source: Abiye et al., 2019).

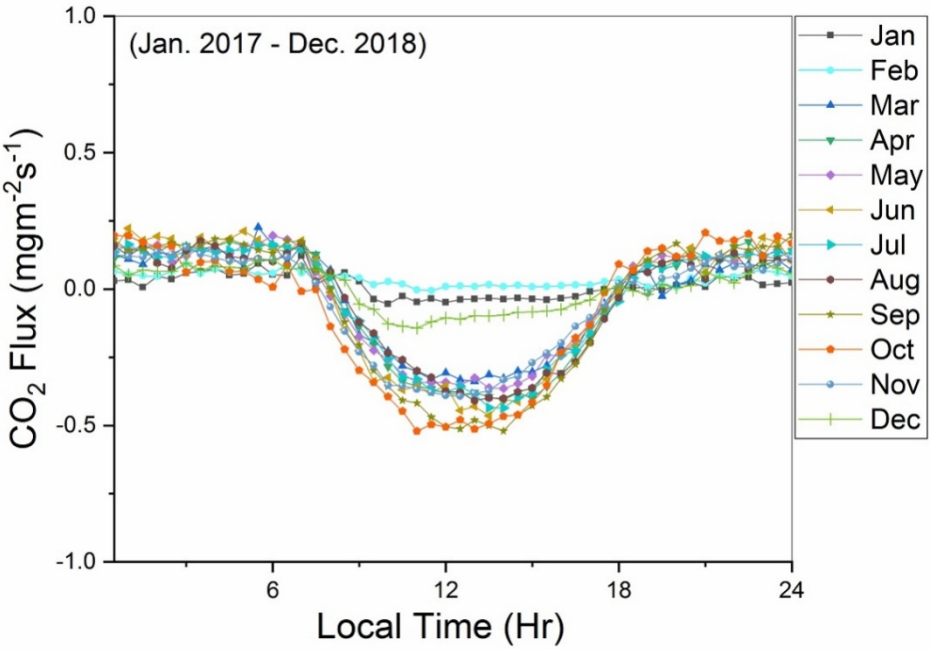

Fig. 3: Diurnal variation of CO_2 flux at OAU Met-station, Ile-Ife, Nigeria during the observation period: 2017-2018

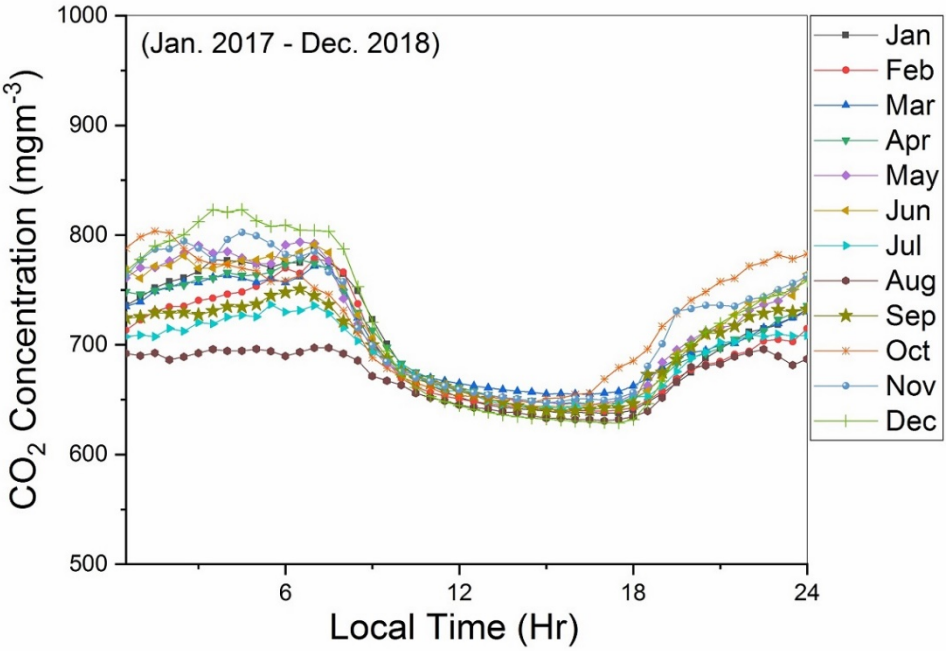

Fig. 4: Diurnal variation of CO_2 concentration at OAU Met-station, Ile-Ife, Nigeria during the observation period: 2017-2018.

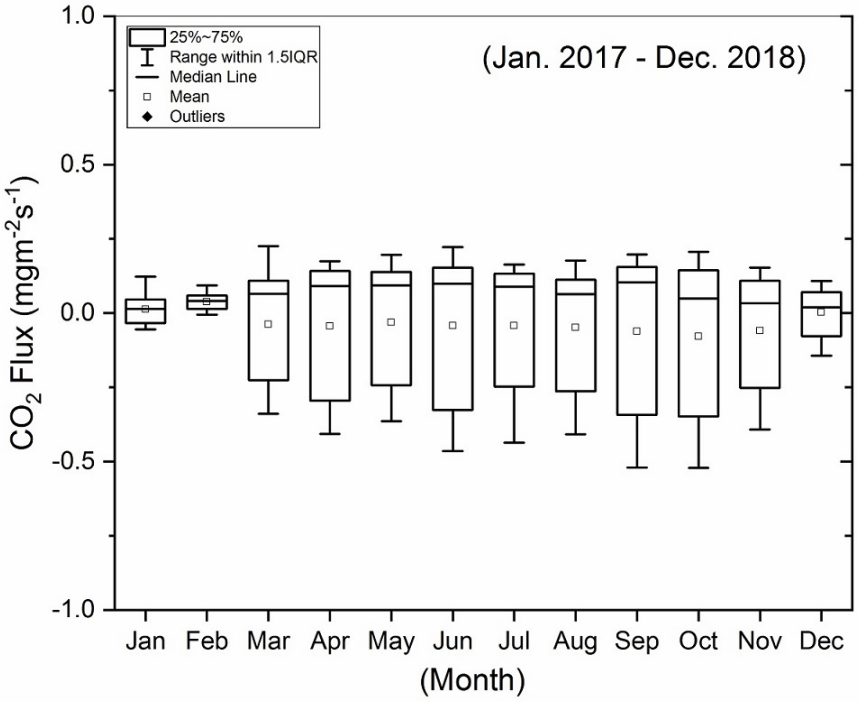

Fig. 5: Box and whisker plots of CO_2 flux at OAU Met-station, Ile-Ife, Nigeria during the observation period: 2017-2018.

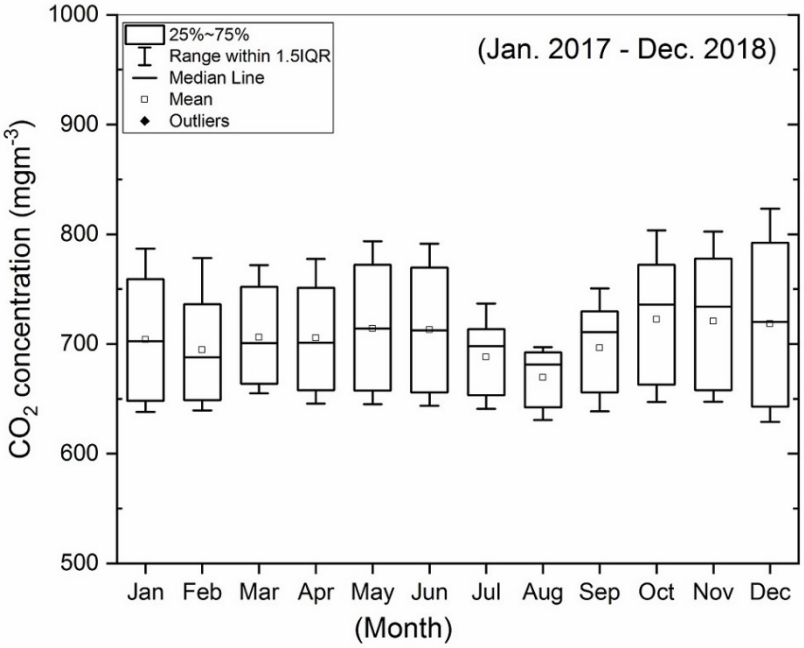

Fig. 6: Box and whisker plots of CO_2 concentration at OAU Met-station, Ile-Ife, Nigeria during the observation period: 2017-2018.

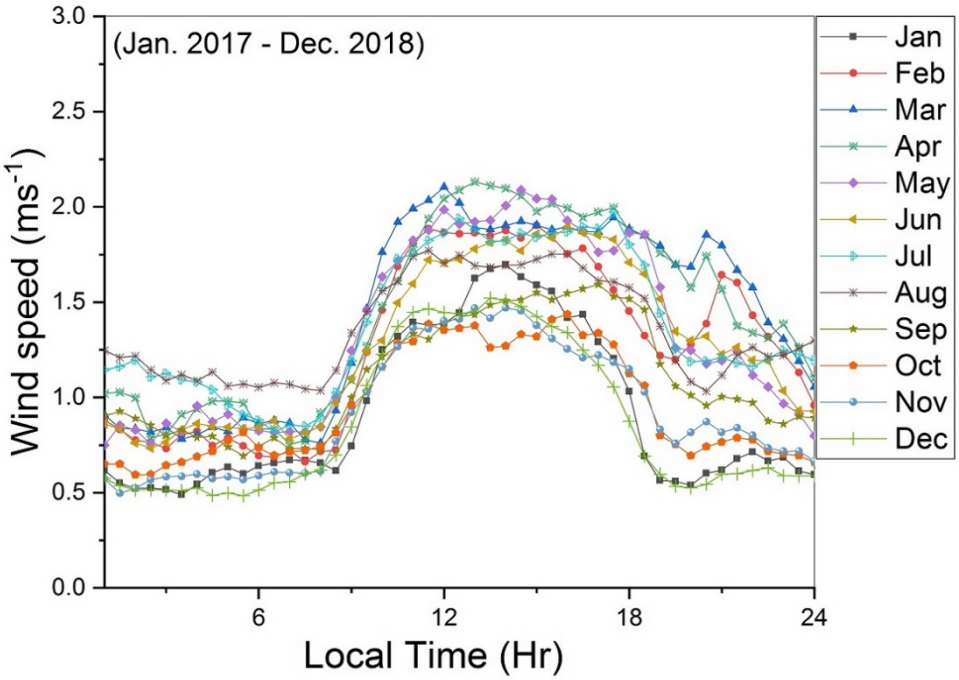

Fig. 7: Diurnal pattern of wind speed at OAU Met-station, Ile-Ife, Nigeria during the observation period: 2017-2018

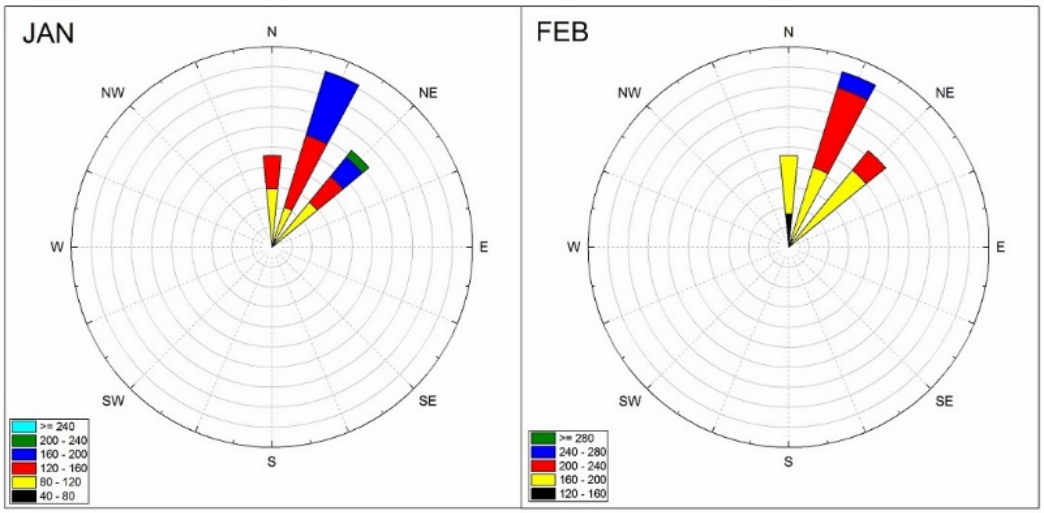

Fig. 8 (a)

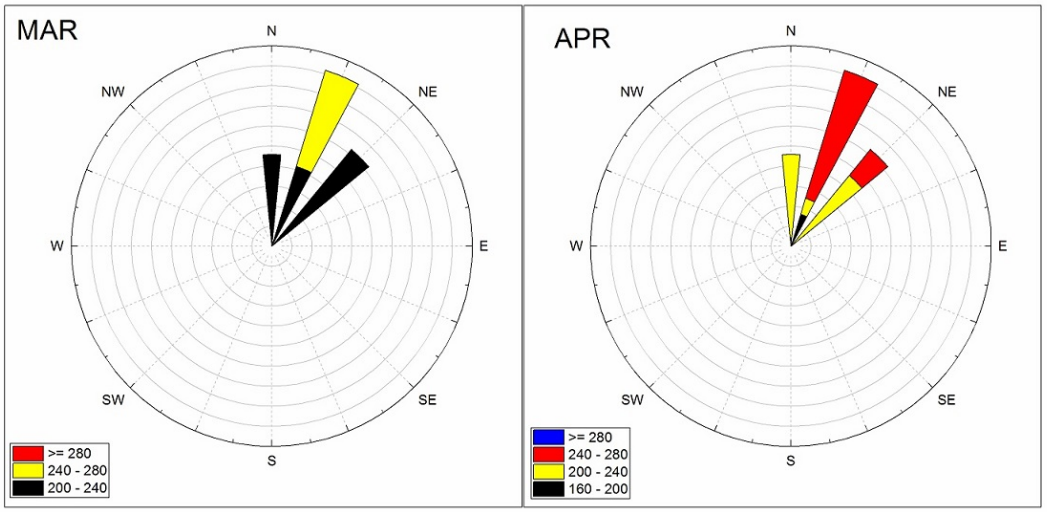

Fig. 8 (b)

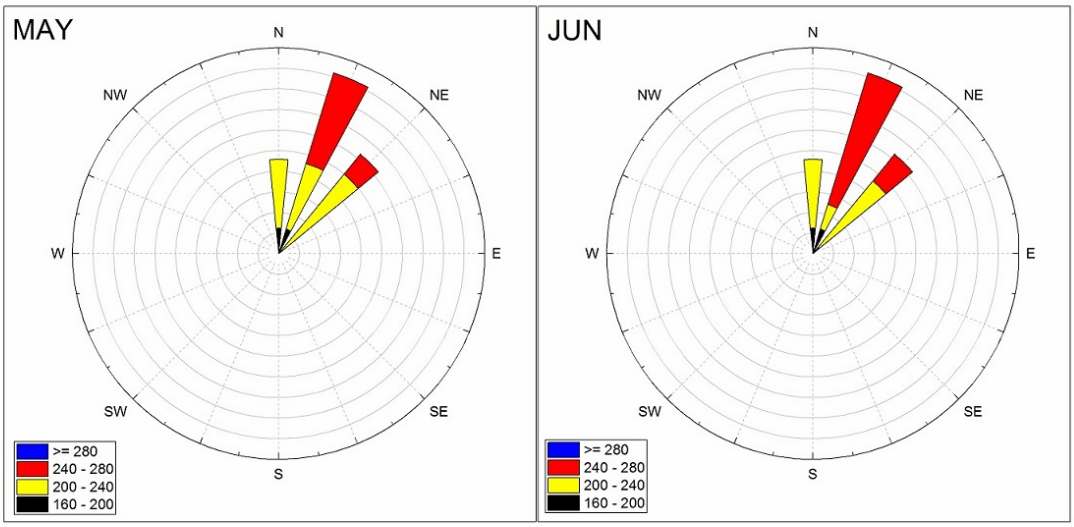

Fig. 8 (c)

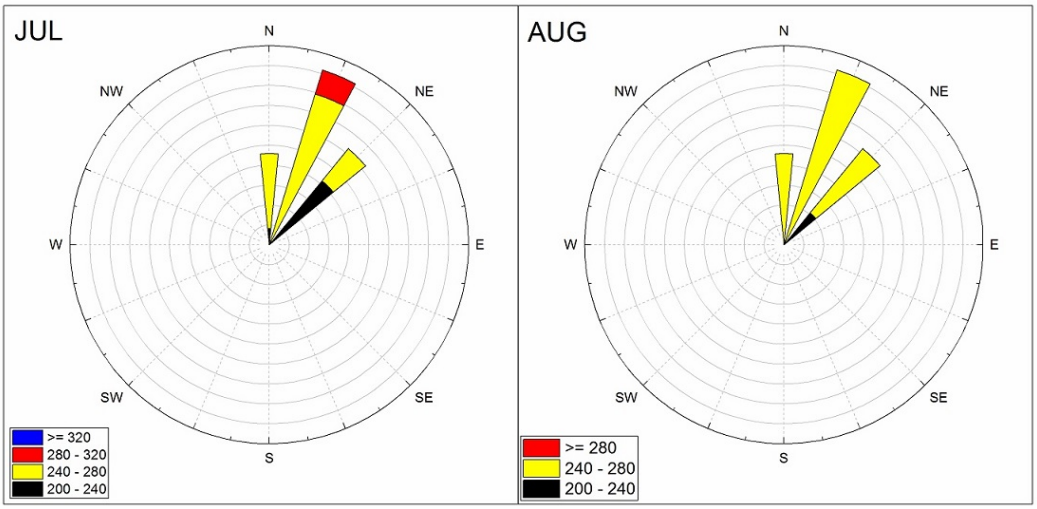

Fig. 8 (d)

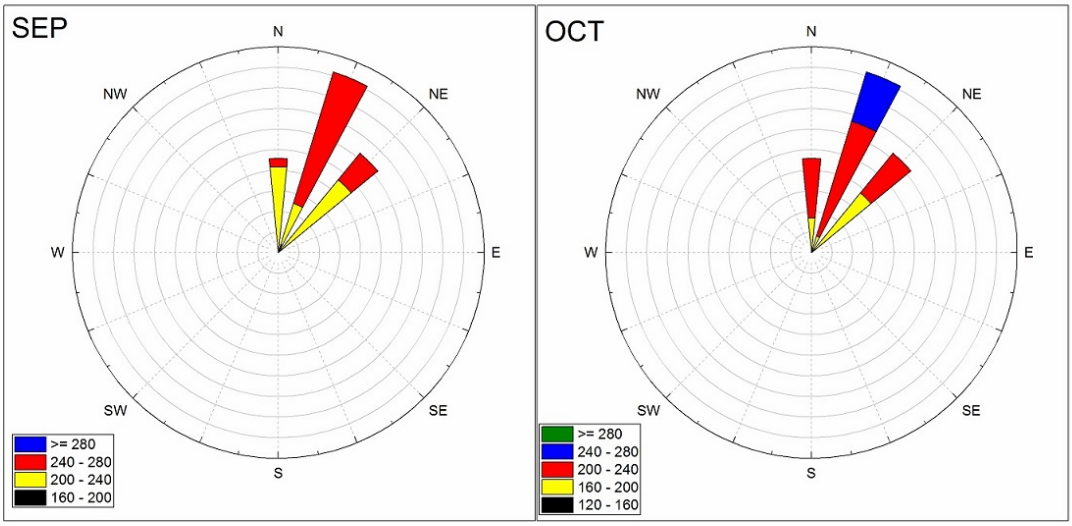

Fig. 8 (e)

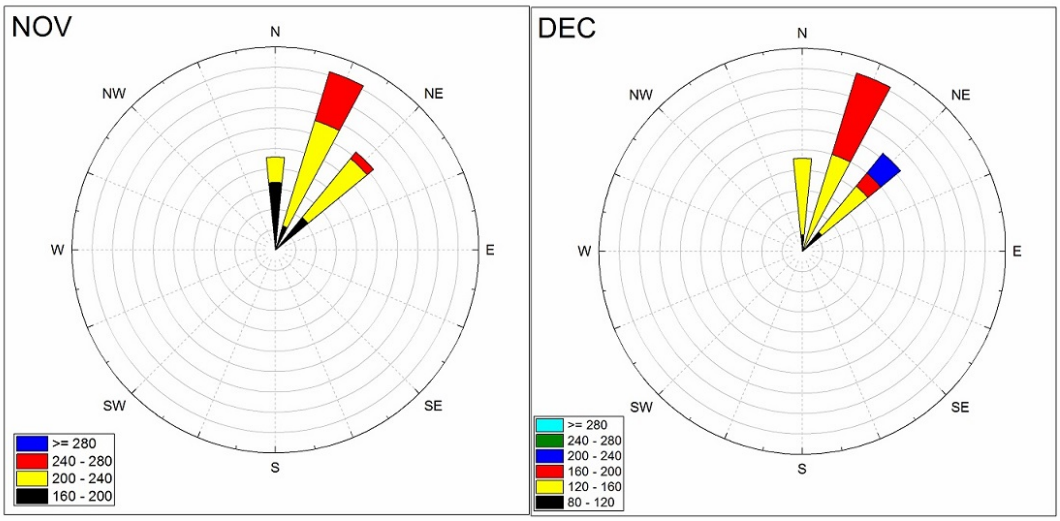

Fig. 8 (f)

Fig. 8: Wind roses depicting dominant wind flow sectors at OAU Met- station, Ile-Ife, Nigeria during the observation period: 2017-2018.

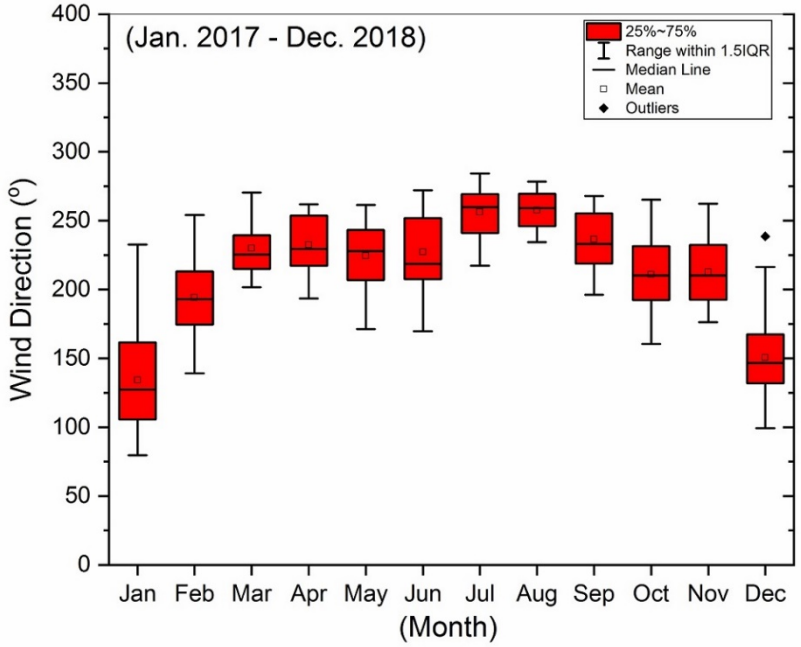

Fig. 9: Box and whisker plots depicting monthly and seasonal wind flow at OAU Met-station, Ile-Ife, Nigeria during the observation period: 2017-2018.

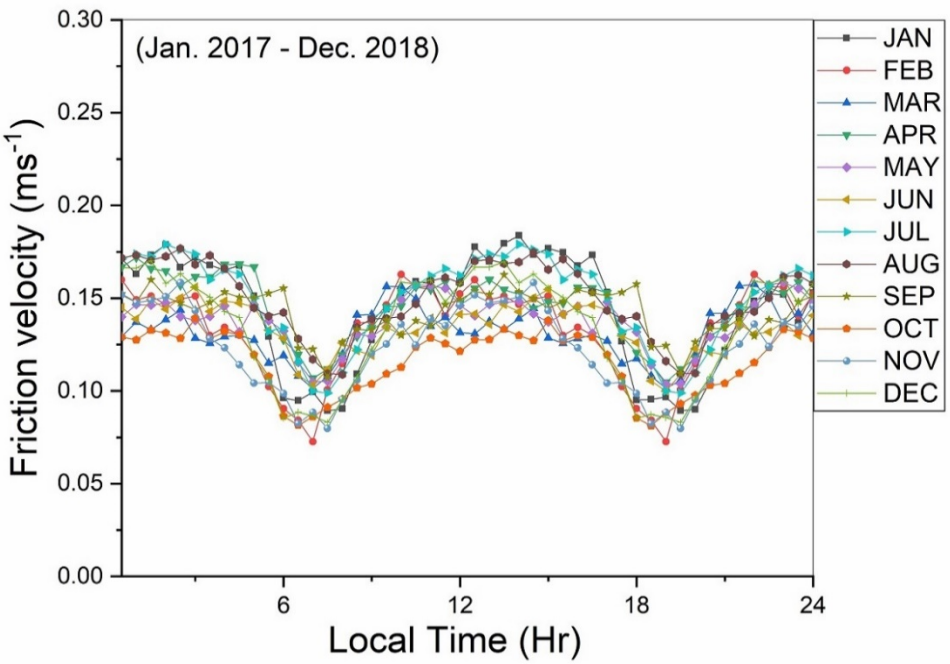

Fig. 10: Diurnal pattern of Friction velocity (u*) at OAU Met-station, Ile-Ife, Nigeria during the observation period: 2017-2018.

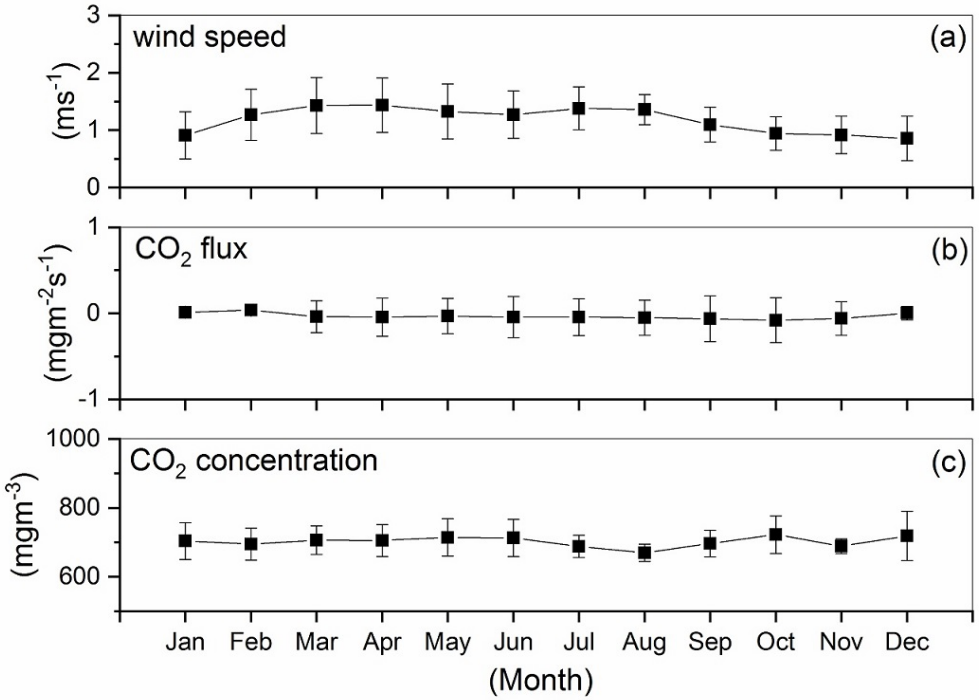

Fig. 11: Monthly Trends of (a) wind speed, (b) CO_2 flux, and (c) CO_2 concentration at OAU Met-station, Ile-Ife, Nigeria during the observation period: 2017-2018

List of Tables

Table 1: Wind classification as observed at the study location, OAU Met-station, Ile-Ife, Nigeria for the observation period: 2017-2018

Class	calm	weak	relatively weak	strong	relatively strong	very strong
Wind speed (ms^{-1})	< 0.5	0.5 – 1.0	1.0 – 1.5	1.5 –2.0	2.0 – 2.5	2.5 -3.0

Table 2: Dominant wind flow as observed at the study location, OAU Met-station, Ile-Ife, Nigeria for the observation period: 2017-2018

Month	Jan	Feb	Mar	Apr	May	Jun	Jul	Aug	Sep	Oct	Nov	Dec
Dominant wind	SE	SE, SW	SW	SW	SW	SW	SW	SW	SW	SW, SE	SW	SE

Table 3: Monthly mean values of CO_2 flux and other meteorological parameters as observed at the study location, OAU Met-station, Ile-Ife, Nigeria for the observation period: 2017-2018

Month	Mean Wind speed. (±SD) (ms^{-1})	Mean Friction vel.(±SD) (ms^{-1})	Mean Air Temp. (±SD) (°C)	Mean Rel. Hum. (±SD) (%)	Mean Global Rad. (±SD) (Wm^{-2})	Mean CO_2Flux (±SD) ($mgm^{-2}s^{-1}$)
Jan	0.9±0.4	0.14±0.03	25.9±6.2	58.1±23.1	179.0±29.0	0.01±0.04
Feb	1.3±0.4	0.13±0.03	28.9±4.8	67.9±20.3	189.3±40.9	0.04±0.03
Mar	1.4±0.5	0.13±0.01	28.8±4.1	77.0±17.6	219.1±54.2	- 0.04±0.18
Apr	1.4±0.5	0.14±0.02	28.2±3.4	80.9±13.3	204.0±61.5	- 0.04±0.22
May	1.3±0.5	0.14±0.01	27.7±3.0	84.0±12.4	199.9±77.0	- 0.03±0.20
June	1.3±0.4	0.13±0.01	27.0±2.8	85.5±11.5	184.1±70.2	- 0.04±0.24
July	1.4±0.4	0.15±0.02	25.9±2.0	88.5±8.4	146.5±70.2	- 0.04±0.21
Aug	1.4±0.3	0.15±0.02	25.9±2.0	88.7±8.3	125.2±63.5	- 0.05±0.20
Sept	1.1±0.3	0.14±0.01	26.7±2.6	87.3±11.1	160.1±72.5	- 0.06±0.27

Oct	0.9±0.3	0.12±0.02	26.1±2.9	86.2±11.4	187.7±63.0	- 0.08±0.26
Nov	0.9±0.3	0.12±0.02	27.3±2.0	79.8±16.8	194.8±48.5	- 0.06±0.20
Dec	0.9±0.4	0.13±0.03	26.0±5.5	69.6±22.6	184.7±34.9	0.00±0.08
Annual	1.2±0.4	0.14±0.02	27.0±3.4	79.5±14.7	181.2±57.1	- 0.03±0.18

Table 4: Monthly mean, minimum, maximum and range of CO_2 concentration at the study location, OAU Met-station, Ile-Ife, Nigeria for the observation period: 2017 – 2018

Month	Mean CO_2 Conc. (±SD) (mgm^{-3})	Min. CO_2 Conc.(mgm^{-3})	Max. CO_2 Conc. (mgm^{-3})	CO_2 Conc. Range (mgm^{-3})
Jan	703.9±53.4	637.9	786.7	148.8
Feb	694.6±46.0	639.5	778.3	138.8
Mar	706.0±41.6	655.0	771.8	116.8
Apr	705.4±46.5	645.6	777.6	132.0
May	714.3±54.4	645.2	793.7	148.5
Jun	713.0±54.2	643.7	791.3	147.6
Jul	688.2±32.1	640.8	736.7	95.9
Aug	669.5±24.9	630.7	697.2	66.5
Sept	696.4±38.6	638.6	750.7	112.1
Oct	722.3±54.3	647.0	803.6	156.6
Nov	688.8±21.4	647.2	802.5	155.3
Dec	718.3±71.3	628.8	823.3	194.5
Annual	704.4±47.2	641.7	776.1	134.5

Global Journals Guidelines Handbook 2023

www.GlobalJournals.org

Memberships

Fellows/Associates of Science Frontier Research Council

FSFRC/ASFRC Memberships

Introduction

FSFRC/ASFRC is the most prestigious membership of Global Journals accredited by Open Association of Research Society, U.S.A (OARS). The credentials of Fellow and Associate designations signify that the researcher has gained the knowledge of the fundamental and high-level concepts, and is a subject matter expert, proficient in an expertise course covering the professional code of conduct, and follows recognized standards of practice. The credentials are designated only to the researchers, scientists, and professionals that have been selected by a rigorous process by our Editorial Board and Management Board.

Associates of FSFRC/ASFRC are scientists and researchers from around the world are working on projects/researches that have huge potentials. Members support Global Journals' mission to advance technology for humanity and the profession.

FSFRC

Fellow of Science Frontier Research Council

FELLOW OF SCIENCE FRONTIER RESEARCH COUNCIL is the most prestigious membership of Global Journals. It is an award and membership granted to individuals that the Open Association of Research Society judges to have made a 'substantial contribution to the improvement of computer science, technology, and electronics engineering.

The primary objective is to recognize the leaders in research and scientific fields of the current era with a global perspective and to create a channel between them and other researchers for better exposure and knowledge sharing. Members are most eminent scientists, engineers, and technologists from all across the world. Fellows are elected for life through a peer review process on the basis of excellence in the respective domain. There is no limit on the number of new nominations made in any year. Each year, the Open Association of Research Society elect up to 12 new Fellow Members.

Benefit

To the institution

Get letter of appreciation

Global Journals sends a letter of appreciation of author to the Dean or CEO of the University or Company of which author is a part, signed by editor in chief or chief author.

Exclusive Network

Get access to a closed network

A FSFRC member gets access to a closed network of Tier 1 researchers and scientists with direct communication channel through our website. Fellows can reach out to other members or researchers directly. They should also be open to reaching out by other.

Career | Credibility | Exclusive | Reputation

Certificate

Receive a print ed copy of a certificate

Fellows receive a printed copy of a certificate signed by our Chief Author that may be used for academic purposes and a personal recommendation letter to the dean of member's university.

Career | Credibility | Exclusive | Reputation

Designation

Get honored title of membership

Fellows can use the honored title of membership. The “FSFRC” is an honored title which is accorded to a person’s name viz. Dr. John E. Hall, Ph.D., FSFRC or William Walldroff, M.S., FSFRC.

Career | Credibility | Exclusive | Reputation

Recognition on the Platform

Better visibility and citation

All the Fellow members of FSFRC get a badge of "Leading Member of Global Journals" on the Research Community that distinguishes them from others. Additionally, the profile is also partially maintained by our team for better visibility and citation. All fellows get a dedicated page on the website with their biography.

Career | Credibility | Reputation

Future Work

Get discounts on the future publications

Fellows receive discounts on future publications with Global Journals up to 60%. Through our recommendation programs, members also receive discounts on publications made with OARS affiliated organizations.

Career | Financial

GJ Internal Account

Unlimited forward of Emails

Fellows get secure and fast GJ work emails with unlimited forward of emails that they may use them as their primary email. For example,
john [AT] globaljournals [DOT] org.

Career | Credibility | Reputation

Premium Tools

Access to all the premium tools

To take future researches to the zenith, fellows and associates receive access to all the premium tools that Global Journals have to offer along with the partnership with some of the best marketing leading tools out there.

Financial

Conferences & Events

Organize seminar/conference

Fellows are authorized to organize symposium/seminar/conference on behalf of Global Journal Incorporation (USA). They can also participate in the same organized by another institution as representative of Global Journal. In both the cases, it is mandatory for him to discuss with us and obtain our consent. Additionally, they get free research conferences (and others) alerts.

Career | Credibility | Financial

Early Invitations

Early invitations to all the symposiums, seminars, conferences

All fellows receive the early invitations to all the symposiums, seminars, conferences and webinars hosted by Global Journals in their subject.

Exclusive

Publishing Articles & Books

Earn 60% of sales proceeds

Fellows can publish articles (limited) without any fees. Also, they can earn up to 60% of sales proceeds from the sale of reference/review books/literature/ publishing of research paper. The FSFRC member can decide its price and we can help in making the right decision.

Exclusive | Financial

Reviewers

Get a remuneration of 15% of author fees

Fellow members are eligible to join as a paid peer reviewer at Global Journals Incorporation (USA) and can get a remuneration of 15% of author fees, taken from the author of a respective paper.

Financial

Access to Editorial Board

Become a member of the Editorial Board

Fellows may join as a member of the Editorial Board of Global Journals Incorporation (USA) after successful completion of three years as Fellow and as Peer Reviewer. Additionally, Fellows get a chance to nominate other members for Editorial Board.

Career | Credibility | Exclusive | Reputation

And Much More

Get access to scientific museums and observatories across the globe

All members get access to 5 selected scientific museums and observatories across the globe. All researches published with Global Journals will be kept under deep archival facilities across regions for future protections and disaster recovery. They get 10 GB free secure cloud access for storing research files.

ASSOCIATE OF SCIENCE FRONTIER RESEARCH COUNCIL

ASSOCIATE OF SCIENCE FRONTIER RESEARCH COUNCIL is the membership of Global Journals awarded to individuals that the Open Association of Research Society judges to have made a 'substantial contribution to the improvement of computer science, technology, and electronics engineering.

The primary objective is to recognize the leaders in research and scientific fields of the current era with a global perspective and to create a channel between them and other researchers for better exposure and knowledge sharing. Members are most eminent scientists, engineers, and technologists from all across the world. Associate membership can later be promoted to Fellow Membership. Associates are elected for life through a peer review process on the basis of excellence in the respective domain. There is no limit on the number of new nominations made in any year. Each year, the Open Association of Research Society elect up to 12 new Associate Members.

To the institution

Get letter of appreciation

Global Journals sends a letter of appreciation of author to the Dean or CEO of the University or Company of which author is a part, signed by editor in chief or chief author.

Exclusive Network

Get access to a closed network

A ASFRC member gets access to a closed network of Tier 1 researchers and scientists with direct communication channel through our website. Associates can reach out to other members or researchers directly. They should also be open to reaching out by other.

Career | Credibility | Exclusive | Reputation

Certificate

Receive a print ed copy of a certificate

Associates receive a printed copy of a certificate signed by our Chief Author that may be used for academic purposes and a personal recommendation letter to the dean of member's university.

Career | Credibility | Exclusive | Reputation

Designation

Get honored title of membership

Associates can use the honored title of membership. The “ASFRC” is an honored title which is accorded to a person’s name viz. Dr. John E. Hall, Ph.D., ASFRC or William Walldroff, M.S., ASFRC.

Career | Credibility | Exclusive | Reputation

Recognition on the Platform

Better visibility and citation

All the Associate members of ASFRC get a badge of "Leading Member of Global Journals" on the Research Community that distinguishes them from others. Additionally, the profile is also partially maintained by our team for better visibility and citation. All associates get a dedicated page on the website with their biography.

Career | Credibility | Reputation

Future Work

Get discounts on the future publications

Associates receive discounts on the future publications with Global Journals up to 60%. Through our recommendation programs, members also receive discounts on publications made with OARS affiliated organizations.

Career | Financial

GJ Internal Account

Unlimited forward of Emails

Associates get secure and fast GJ work emails with unlimited forward of emails that they may use them as their primary email. For example, john [AT] globaljournals [DOT] org.

Career | Credibility | Reputation

Premium Tools

Access to all the premium tools

To take future researches to the zenith, fellows receive access to almost all the premium tools that Global Journals have to offer along with the partnership with some of the best marketing leading tools out there.

Financial

Conferences & Events

Organize seminar/conference

Associates are authorized to organize symposium/seminar/conference on behalf of Global Journal Incorporation (USA). They can also participate in the same organized by another institution as representative of Global Journal. In both the cases, it is mandatory for him to discuss with us and obtain our consent. Additionally, they get free research conferences (and others) alerts.

Career | Credibility | Financial

Early Invitations

Early invitations to all the symposiums, seminars, conferences

All associates receive the early invitations to all the symposiums, seminars, conferences and webinars hosted by Global Journals in their subject.

Exclusive

Publishing Articles & Books

Earn 30-40% of sales proceeds

Associates can publish articles (limited) without any fees. Also, they can earn up to 30-40% of sales proceeds from the sale of reference/review books/literature/publishing of research paper.

Exclusive | Financial

Reviewers

Get a remuneration of 15% of author fees

Associate members are eligible to join as a paid peer reviewer at Global Journals Incorporation (USA) and can get a remuneration of 15% of author fees, taken from the author of a respective paper.

Financial

And Much More

Get access to scientific museums and observatories across the globe

All members get access to 2 selected scientific museums and observatories across the globe. All researches published with Global Journals will be kept under deep archival facilities across regions for future protections and disaster recovery. They get 5 GB free secure cloud access for storing research files.

Associate	Fellow	Research Group	Basic
$4800 **lifetime designation**	$6800 **lifetime designation**	$12500.00 **organizational**	APC **per article**
Certificate, LoR and Momento **2** discounted publishing/year **Gradation** of Research **10** research contacts/day **1 GB** Cloud Storage **GJ** Community Access	**Certificate,** LoR and Momento **Unlimited** discounted publishing/year **Gradation** of Research **Unlimited** research contacts/day **5 GB** Cloud Storage **Online Presense** Assistance **GJ** Community Access	**Certificates,** LoRs and Momentos **Unlimited** free publishing/year **Gradation** of Research **Unlimited** research contacts/day **Unlimited** Cloud Storage **Online Presense** Assistance **GJ** Community Access	**GJ** Community Access

Preferred Author Guidelines

We accept the manuscript submissions in any standard (generic) format.

We typeset manuscripts using advanced typesetting tools like Adobe In Design, CorelDraw, TeXnicCenter, and TeXStudio. We usually recommend authors submit their research using any standard format they are comfortable with, and let Global Journals do the rest.

Alternatively, you can download our basic template from https://globaljournals.org/Template.zip

Authors should submit their complete paper/article, including text illustrations, graphics, conclusions, artwork, and tables. Authors who are not able to submit manuscript using the form above can email the manuscript department at submit@globaljournals.org or get in touch with chiefeditor@globaljournals.org if they wish to send the abstract before submission.

Before and during Submission

Authors must ensure the information provided during the submission of a paper is authentic. Please go through the following checklist before submitting:

1. Authors must go through the complete author guideline and understand and *agree to Global Journals' ethics and code of conduct,* along with author responsibilities.
2. Authors must accept the privacy policy, terms, and conditions of Global Journals.
3. Ensure corresponding author's email address and postal address are accurate and reachable.
4. Manuscript to be submitted must include keywords, an abstract, a paper title, co-author(s') names and details (email address, name, phone number, and institution), figures and illustrations in vector format including appropriate captions, tables, including titles and footnotes, a conclusion, results, acknowledgments and references.
5. Authors should submit paper in a ZIP archive if any supplementary files are required along with the paper.
6. Proper permissions must be acquired for the use of any copyrighted material.
7. Manuscript submitted *must not have been submitted or published elsewhere* and all authors must be aware of the submission.

Declaration of Conflicts of Interest

It is required for authors to declare all financial, institutional, and personal relationships with other individuals and organizations that could influence (bias) their research.

Policy on Plagiarism

Plagiarism is not acceptable in Global Journals submissions at all.

Plagiarized content will not be considered for publication. We reserve the right to inform authors' institutions about plagiarism detected either before or after publication. If plagiarism is identified, we will follow COPE guidelines:

Authors are solely responsible for all the plagiarism that is found. The author must not fabricate, falsify or plagiarize existing research data. The following, if copied, will be considered plagiarism:

- Words (language)
- Ideas
- Findings
- Writings
- Diagrams
- Graphs
- Illustrations
- Lectures

- Printed material
- Graphic representations
- Computer programs
- Electronic material
- Any other original work

Authorship Policies

Global Journals follows the definition of authorship set up by the Open Association of Research Society, USA. According to its guidelines, authorship criteria must be based on:

1. Substantial contributions to the conception and acquisition of data, analysis, and interpretation of findings.
2. Drafting the paper and revising it critically regarding important academic content.
3. Final approval of the version of the paper to be published.

Changes in Authorship

The corresponding author should mention the name and complete details of all co-authors during submission and in manuscript. We support addition, rearrangement, manipulation, and deletions in authors list till the early view publication of the journal. We expect that corresponding author will notify all co-authors of submission. We follow COPE guidelines for changes in authorship.

Copyright

During submission of the manuscript, the author is confirming an exclusive license agreement with Global Journals which gives Global Journals the authority to reproduce, reuse, and republish authors' research. We also believe in flexible copyright terms where copyright may remain with authors/employers/institutions as well. Contact your editor after acceptance to choose your copyright policy. You may follow this form for copyright transfers.

Appealing Decisions

Unless specified in the notification, the Editorial Board's decision on publication of the paper is final and cannot be appealed before making the major change in the manuscript.

Acknowledgments

Contributors to the research other than authors credited should be mentioned in Acknowledgments. The source of funding for the research can be included. Suppliers of resources may be mentioned along with their addresses.

Declaration of funding sources

Global Journals is in partnership with various universities, laboratories, and other institutions worldwide in the research domain. Authors are requested to disclose their source of funding during every stage of their research, such as making analysis, performing laboratory operations, computing data, and using institutional resources, from writing an article to its submission. This will also help authors to get reimbursements by requesting an open access publication letter from Global Journals and submitting to the respective funding source.

Preparing your Manuscript

Authors can submit papers and articles in an acceptable file format: MS Word (doc, docx), LaTeX (.tex, .zip or .rar including all of your files), Adobe PDF (.pdf), rich text format (.rtf), simple text document (.txt), Open Document Text (.odt), and Apple Pages (.pages). Our professional layout editors will format the entire paper according to our official guidelines. This is one of the highlights of publishing with Global Journals—authors should not be concerned about the formatting of their paper. Global Journals accepts articles and manuscripts in every major language, be it Spanish, Chinese, Japanese, Portuguese, Russian, French, German, Dutch, Italian, Greek, or any other national language, but the title, subtitle, and abstract should be in English. This will facilitate indexing and the pre-peer review process.

The following is the official style and template developed for publication of a research paper. Authors are not required to follow this style during the submission of the paper. It is just for reference purposes.

Manuscript Style Instruction (Optional)

- Microsoft Word Document Setting Instructions.
- Font type of all text should be Swis721 Lt BT.
- Page size: 8.27" x 11'", left margin: 0.65, right margin: 0.65, bottom margin: 0.75.
- Paper title should be in one column of font size 24.
- Author name in font size of 11 in one column.
- Abstract: font size 9 with the word "Abstract" in bold italics.
- Main text: font size 10 with two justified columns.
- Two columns with equal column width of 3.38 and spacing of 0.2.
- First character must be three lines drop-capped.
- The paragraph before spacing of 1 pt and after of 0 pt.
- Line spacing of 1 pt.
- Large images must be in one column.
- The names of first main headings (Heading 1) must be in Roman font, capital letters, and font size of 10.
- The names of second main headings (Heading 2) must not include numbers and must be in italics with a font size of 10.

Structure and Format of Manuscript

The recommended size of an original research paper is under 15,000 words and review papers under 7,000 words. Research articles should be less than 10,000 words. Research papers are usually longer than review papers. Review papers are reports of significant research (typically less than 7,000 words, including tables, figures, and references)

A research paper must include:

a) A title which should be relevant to the theme of the paper.
b) A summary, known as an abstract (less than 150 words), containing the major results and conclusions.
c) Up to 10 keywords that precisely identify the paper's subject, purpose, and focus.
d) An introduction, giving fundamental background objectives.
e) Resources and techniques with sufficient complete experimental details (wherever possible by reference) to permit repetition, sources of information must be given, and numerical methods must be specified by reference.
f) Results which should be presented concisely by well-designed tables and figures.
g) Suitable statistical data should also be given.
h) All data must have been gathered with attention to numerical detail in the planning stage.

Design has been recognized to be essential to experiments for a considerable time, and the editor has decided that any paper that appears not to have adequate numerical treatments of the data will be returned unrefereed.

i) Discussion should cover implications and consequences and not just recapitulate the results; conclusions should also be summarized.
j) There should be brief acknowledgments.
k) There ought to be references in the conventional format. Global Journals recommends APA format.

Authors should carefully consider the preparation of papers to ensure that they communicate effectively. Papers are much more likely to be accepted if they are carefully designed and laid out, contain few or no errors, are summarizing, and follow instructions. They will also be published with much fewer delays than those that require much technical and editorial correction.

The Editorial Board reserves the right to make literary corrections and suggestions to improve brevity.

Format Structure

It is necessary that authors take care in submitting a manuscript that is written in simple language and adheres to published guidelines.

All manuscripts submitted to Global Journals should include:

Title

The title page must carry an informative title that reflects the content, a running title (less than 45 characters together with spaces), names of the authors and co-authors, and the place(s) where the work was carried out.

Author details

The full postal address of any related author(s) must be specified.

Abstract

The abstract is the foundation of the research paper. It should be clear and concise and must contain the objective of the paper and inferences drawn. It is advised to not include big mathematical equations or complicated jargon.

Many researchers searching for information online will use search engines such as Google, Yahoo or others. By optimizing your paper for search engines, you will amplify the chance of someone finding it. In turn, this will make it more likely to be viewed and cited in further works. Global Journals has compiled these guidelines to facilitate you to maximize the web-friendliness of the most public part of your paper.

Keywords

A major lynchpin of research work for the writing of research papers is the keyword search, which one will employ to find both library and internet resources. Up to eleven keywords or very brief phrases have to be given to help data retrieval, mining, and indexing.

One must be persistent and creative in using keywords. An effective keyword search requires a strategy: planning of a list of possible keywords and phrases to try.

Choice of the main keywords is the first tool of writing a research paper. Research paper writing is an art. Keyword search should be as strategic as possible.

One should start brainstorming lists of potential keywords before even beginning searching. Think about the most important concepts related to research work. Ask, “What words would a source have to include to be truly valuable in a research paper?” Then consider synonyms for the important words.

It may take the discovery of only one important paper to steer in the right keyword direction because, in most databases, the keywords under which a research paper is abstracted are listed with the paper.

Numerical Methods

Numerical methods used should be transparent and, where appropriate, supported by references.

Abbreviations

Authors must list all the abbreviations used in the paper at the end of the paper or in a separate table before using them.

Formulas and equations

Authors are advised to submit any mathematical equation using either MathJax, KaTeX, or LaTeX, or in a very high-quality image.

Tables, Figures, and Figure Legends

Tables: Tables should be cautiously designed, uncrowned, and include only essential data. Each must have an Arabic number, e.g., Table 4, a self-explanatory caption, and be on a separate sheet. Authors must submit tables in an editable format and not as images. References to these tables (if any) must be mentioned accurately.

Figures

Figures are supposed to be submitted as separate files. Always include a citation in the text for each figure using Arabic numbers, e.g., Fig. 4. Artwork must be submitted online in vector electronic form or by emailing it.

Preparation of Eletronic Figures for Publication

Although low-quality images are sufficient for review purposes, print publication requires high-quality images to prevent the final product being blurred or fuzzy. Submit (possibly by e-mail) EPS (line art) or TIFF (halftone/ photographs) files only. MS PowerPoint and Word Graphics are unsuitable for printed pictures. Avoid using pixel-oriented software. Scans (TIFF only) should have a resolution of at least 350 dpi (halftone) or 700 to 1100 dpi (line drawings). Please give the data for figures in black and white or submit a Color Work Agreement form. EPS files must be saved with fonts embedded (and with a TIFF preview, if possible).

For scanned images, the scanning resolution at final image size ought to be as follows to ensure good reproduction: line art: >650 dpi; halftones (including gel photographs): >350 dpi; figures containing both halftone and line images: >650 dpi.

Color charges: Authors are advised to pay the full cost for the reproduction of their color artwork. Hence, please note that if there is color artwork in your manuscript when it is accepted for publication, we would require you to complete and return a Color Work Agreement form before your paper can be published. Also, you can email your editor to remove the color fee after acceptance of the paper.

Tips for Writing a Good Quality Science Frontier Research Paper

Techniques for writing a good quality Science Frontier Research paper:

1. Choosing the topic: In most cases, the topic is selected by the interests of the author, but it can also be suggested by the guides. You can have several topics, and then judge which you are most comfortable with. This may be done by asking several questions of yourself, like "Will I be able to carry out a search in this area? Will I find all necessary resources to accomplish the search? Will I be able to find all information in this field area?" If the answer to this type of question is "yes," then you ought to choose that topic. In most cases, you may have to conduct surveys and visit several places. Also, you might have to do a lot of work to find all the rises and falls of the various data on that subject. Sometimes, detailed information plays a vital role, instead of short information. Evaluators are human: The first thing to remember is that evaluators are also human beings. They are not only meant for rejecting a paper. They are here to evaluate your paper. So present your best aspect.

2. Think like evaluators: If you are in confusion or getting demotivated because your paper may not be accepted by the evaluators, then think, and try to evaluate your paper like an evaluator. Try to understand what an evaluator wants in your research paper, and you will automatically have your answer. Make blueprints of paper: The outline is the plan or framework that will help you to arrange your thoughts. It will make your paper logical. But remember that all points of your outline must be related to the topic you have chosen.

3. Ask your guides: If you are having any difficulty with your research, then do not hesitate to share your difficulty with your guide (if you have one). They will surely help you out and resolve your doubts. If you can't clarify what exactly you require for your work, then ask your supervisor to help you with an alternative. He or she might also provide you with a list of essential readings.

4. Use of computer is recommended: As you are doing research in the field of science frontier then this point is quite obvious. Use right software: Always use good quality software packages. If you are not capable of judging good software, then you can lose the quality of your paper unknowingly. There are various programs available to help you which you can get through the internet.

5. Use the internet for help: An excellent start for your paper is using Google. It is a wondrous search engine, where you can have your doubts resolved. You may also read some answers for the frequent question of how to write your research paper or find a model research paper. You can download books from the internet. If you have all the required books, place importance on reading, selecting, and analyzing the specified information. Then sketch out your research paper. Use big pictures: You may use encyclopedias like Wikipedia to get pictures with the best resolution. At Global Journals, you should strictly follow here.

6. Bookmarks are useful: When you read any book or magazine, you generally use bookmarks, right? It is a good habit which helps to not lose your continuity. You should always use bookmarks while searching on the internet also, which will make your search easier.

7. Revise what you wrote: When you write anything, always read it, summarize it, and then finalize it.

8. Make every effort: Make every effort to mention what you are going to write in your paper. That means always have a good start. Try to mention everything in the introduction—what is the need for a particular research paper. Polish your work with good writing skills and always give an evaluator what he wants. Make backups: When you are going to do any important thing like making a research paper, you should always have backup copies of it either on your computer or on paper. This protects you from losing any portion of your important data.

9. Produce good diagrams of your own: Always try to include good charts or diagrams in your paper to improve quality. Using several unnecessary diagrams will degrade the quality of your paper by creating a hodgepodge. So always try to include diagrams which were made by you to improve the readability of your paper. Use of direct quotes: When you do research relevant to literature, history, or current affairs, then use of quotes becomes essential, but if the study is relevant to science, use of quotes is not preferable.

10. Use proper verb tense: Use proper verb tenses in your paper. Use past tense to present those events that have happened. Use present tense to indicate events that are going on. Use future tense to indicate events that will happen in the future. Use of wrong tenses will confuse the evaluator. Avoid sentences that are incomplete.

11. Pick a good study spot: Always try to pick a spot for your research which is quiet. Not every spot is good for studying.

12. Know what you know: Always try to know what you know by making objectives, otherwise you will be confused and unable to achieve your target.

13. Use good grammar: Always use good grammar and words that will have a positive impact on the evaluator; use of good vocabulary does not mean using tough words which the evaluator has to find in a dictionary. Do not fragment sentences. Eliminate one-word sentences. Do not ever use a big word when a smaller one would suffice.

Verbs have to be in agreement with their subjects. In a research paper, do not start sentences with conjunctions or finish them with prepositions. When writing formally, it is advisable to never split an infinitive because someone will (wrongly) complain. Avoid clichés like a disease. Always shun irritating alliteration. Use language which is simple and straightforward. Put together a neat summary.

14. Arrangement of information: Each section of the main body should start with an opening sentence, and there should be a changeover at the end of the section. Give only valid and powerful arguments for your topic. You may also maintain your arguments with records.

15. Never start at the last minute: Always allow enough time for research work. Leaving everything to the last minute will degrade your paper and spoil your work.

16. Multitasking in research is not good: Doing several things at the same time is a bad habit in the case of research activity. Research is an area where everything has a particular time slot. Divide your research work into parts, and do a particular part in a particular time slot.

17. Never copy others' work: Never copy others' work and give it your name because if the evaluator has seen it anywhere, you will be in trouble. Take proper rest and food: No matter how many hours you spend on your research activity, if you are not taking care of your health, then all your efforts will have been in vain. For quality research, take proper rest and food.

18. Go to seminars: Attend seminars if the topic is relevant to your research area. Utilize all your resources.

19. Refresh your mind after intervals: Try to give your mind a rest by listening to soft music or sleeping in intervals. This will also improve your memory. Acquire colleagues: Always try to acquire colleagues. No matter how sharp you are, if you acquire colleagues, they can give you ideas which will be helpful to your research.

20. Think technically: Always think technically. If anything happens, search for its reasons, benefits, and demerits. Think and then print: When you go to print your paper, check that tables are not split, headings are not detached from their descriptions, and page sequence is maintained.

21. Adding unnecessary information: Do not add unnecessary information like "I have used MS Excel to draw graphs." Irrelevant and inappropriate material is superfluous. Foreign terminology and phrases are not apropos. One should never take a broad view. Analogy is like feathers on a snake. Use words properly, regardless of how others use them. Remove quotations. Puns are for kids, not grunt readers. Never oversimplify: When adding material to your research paper, never go for oversimplification; this will definitely irritate the evaluator. Be specific. Never use rhythmic redundancies. Contractions shouldn't be used in a research paper. Comparisons are as terrible as clichés. Give up ampersands, abbreviations, and so on. Remove commas that are not necessary. Parenthetical words should be between brackets or commas. Understatement is always the best way to put forward earth-shaking thoughts. Give a detailed literary review.

22. Report concluded results: Use concluded results. From raw data, filter the results, and then conclude your studies based on measurements and observations taken. An appropriate number of decimal places should be used. Parenthetical remarks are prohibited here. Proofread carefully at the final stage. At the end, give an outline to your arguments. Spot perspectives of further study of the subject. Justify your conclusion at the bottom sufficiently, which will probably include examples.

23. Upon conclusion: Once you have concluded your research, the next most important step is to present your findings. Presentation is extremely important as it is the definite medium though which your research is going to be in print for the rest of the crowd. Care should be taken to categorize your thoughts well and present them in a logical and neat manner. A good quality research paper format is essential because it serves to highlight your research paper and bring to light all necessary aspects of your research.

Informal Guidelines of Research Paper Writing

Key points to remember:

- Submit all work in its final form.
- Write your paper in the form which is presented in the guidelines using the template.
- Please note the criteria peer reviewers will use for grading the final paper.

Final points:

One purpose of organizing a research paper is to let people interpret your efforts selectively. The journal requires the following sections, submitted in the order listed, with each section starting on a new page:

The introduction: This will be compiled from reference matter and reflect the design processes or outline of basis that directed you to make a study. As you carry out the process of study, the method and process section will be constructed like that. The results segment will show related statistics in nearly sequential order and direct reviewers to similar intellectual paths throughout the data that you gathered to carry out your study.

The discussion section:

This will provide understanding of the data and projections as to the implications of the results. The use of good quality references throughout the paper will give the effort trustworthiness by representing an alertness to prior workings.

Writing a research paper is not an easy job, no matter how trouble-free the actual research or concept. Practice, excellent preparation, and controlled record-keeping are the only means to make straightforward progression.

General style:

Specific editorial column necessities for compliance of a manuscript will always take over from directions in these general guidelines.

To make a paper clear: Adhere to recommended page limits.

Mistakes to avoid:

- Insertion of a title at the foot of a page with subsequent text on the next page.
- Separating a table, chart, or figure—confine each to a single page.
- Submitting a manuscript with pages out of sequence.
- In every section of your document, use standard writing style, including articles ("a" and "the").
- Keep paying attention to the topic of the paper.
- Use paragraphs to split each significant point (excluding the abstract).
- Align the primary line of each section.
- Present your points in sound order.
- Use present tense to report well-accepted matters.
- Use past tense to describe specific results.
- Do not use familiar wording; don't address the reviewer directly. Don't use slang or superlatives.
- Avoid use of extra pictures—include only those figures essential to presenting results.

Title page:

Choose a revealing title. It should be short and include the name(s) and address(es) of all authors. It should not have acronyms or abbreviations or exceed two printed lines.

Abstract: This summary should be two hundred words or less. It should clearly and briefly explain the key findings reported in the manuscript and must have precise statistics. It should not have acronyms or abbreviations. It should be logical in itself. Do not cite references at this point.

An abstract is a brief, distinct paragraph summary of finished work or work in development. In a minute or less, a reviewer can be taught the foundation behind the study, common approaches to the problem, relevant results, and significant conclusions or new questions.

Write your summary when your paper is completed because how can you write the summary of anything which is not yet written? Wealth of terminology is very essential in abstract. Use comprehensive sentences, and do not sacrifice readability for brevity; you can maintain it succinctly by phrasing sentences so that they provide more than a lone rationale. The author can at this moment go straight to shortening the outcome. Sum up the study with the subsequent elements in any summary. Try to limit the initial two items to no more than one line each.

Reason for writing the article—theory, overall issue, purpose.

- Fundamental goal.
- To-the-point depiction of the research.
- Consequences, including definite statistics—if the consequences are quantitative in nature, account for this; results of any numerical analysis should be reported. Significant conclusions or questions that emerge from the research.

Approach:

- Single section and succinct.
- An outline of the job done is always written in past tense.
- Concentrate on shortening results—limit background information to a verdict or two.
- Exact spelling, clarity of sentences and phrases, and appropriate reporting of quantities (proper units, important statistics) are just as significant in an abstract as they are anywhere else.

Introduction:

The introduction should "introduce" the manuscript. The reviewer should be presented with sufficient background information to be capable of comprehending and calculating the purpose of your study without having to refer to other works. The basis for the study should be offered. Give the most important references, but avoid making a comprehensive appraisal of the topic. Describe the problem visibly. If the problem is not acknowledged in a logical, reasonable way, the reviewer will give no attention to your results. Speak in common terms about techniques used to explain the problem, if needed, but do not present any particulars about the protocols here.

The following approach can create a valuable beginning:

- Explain the value (significance) of the study.
- Defend the model—why did you employ this particular system or method? What is its compensation? Remark upon its appropriateness from an abstract point of view as well as pointing out sensible reasons for using it.
- Present a justification. State your particular theory(-ies) or aim(s), and describe the logic that led you to choose them.
- Briefly explain the study's tentative purpose and how it meets the declared objectives.

Approach:

Use past tense except for when referring to recognized facts. After all, the manuscript will be submitted after the entire job is done. Sort out your thoughts; manufacture one key point for every section. If you make the four points listed above, you will need at least four paragraphs. Present surrounding information only when it is necessary to support a situation. The reviewer does not desire to read everything you know about a topic. Shape the theory specifically—do not take a broad view.

As always, give awareness to spelling, simplicity, and correctness of sentences and phrases.

Procedures (methods and materials):

This part is supposed to be the easiest to carve if you have good skills. A soundly written procedures segment allows a capable scientist to replicate your results. Present precise information about your supplies. The suppliers and clarity of reagents can be helpful bits of information. Present methods in sequential order, but linked methodologies can be grouped as a segment. Be concise when relating the protocols. Attempt to give the least amount of information that would permit another capable scientist to replicate your outcome, but be cautious that vital information is integrated. The use of subheadings is suggested and ought to be synchronized with the results section.

When a technique is used that has been well-described in another section, mention the specific item describing the way, but draw the basic principle while stating the situation. The purpose is to show all particular resources and broad procedures so that another person may use some or all of the methods in one more study or referee the scientific value of your work. It is not to be a step-by-step report of the whole thing you did, nor is a methods section a set of orders.

Materials:

Materials may be reported in part of a section or else they may be recognized along with your measures.

Methods:

- Report the method and not the particulars of each process that engaged the same methodology.
- Describe the method entirely.
- To be succinct, present methods under headings dedicated to specific dealings or groups of measures.
- Simplify—detail how procedures were completed, not how they were performed on a particular day.
- If well-known procedures were used, account for the procedure by name, possibly with a reference, and that's all.

Approach:

It is embarrassing to use vigorous voice when documenting methods without using first person, which would focus the reviewer's interest on the researcher rather than the job. As a result, when writing up the methods, most authors use third person passive voice.

Use standard style in this and every other part of the paper—avoid familiar lists, and use full sentences.

What to keep away from:

- Resources and methods are not a set of information.
- Skip all descriptive information and surroundings—save it for the argument.
- Leave out information that is immaterial to a third party.

Results:

The principle of a results segment is to present and demonstrate your conclusion. Create this part as entirely objective details of the outcome, and save all understanding for the discussion.

The page length of this segment is set by the sum and types of data to be reported. Use statistics and tables, if suitable, to present consequences most efficiently.

You must clearly differentiate material which would usually be incorporated in a study editorial from any unprocessed data or additional appendix matter that would not be available. In fact, such matters should not be submitted at all except if requested by the instructor.

Content:

- Sum up your conclusions in text and demonstrate them, if suitable, with figures and tables.
- In the manuscript, explain each of your consequences, and point the reader to remarks that are most appropriate.
- Present a background, such as by describing the question that was addressed by creation of an exacting study.
- Explain results of control experiments and give remarks that are not accessible in a prescribed figure or table, if appropriate.
- Examine your data, then prepare the analyzed (transformed) data in the form of a figure (graph), table, or manuscript.

What to stay away from:

- Do not discuss or infer your outcome, report surrounding information, or try to explain anything.
- Do not include raw data or intermediate calculations in a research manuscript.
- Do not present similar data more than once.
- A manuscript should complement any figures or tables, not duplicate information.
- Never confuse figures with tables—there is a difference.

Approach:

As always, use past tense when you submit your results, and put the whole thing in a reasonable order.

Put figures and tables, appropriately numbered, in order at the end of the report.

If you desire, you may place your figures and tables properly within the text of your results section.

Figures and tables:

If you put figures and tables at the end of some details, make certain that they are visibly distinguished from any attached appendix materials, such as raw facts. Whatever the position, each table must be titled, numbered one after the other, and include a heading. All figures and tables must be divided from the text.

Discussion:

The discussion is expected to be the trickiest segment to write. A lot of papers submitted to the journal are discarded based on problems with the discussion. There is no rule for how long an argument should be.

Position your understanding of the outcome visibly to lead the reviewer through your conclusions, and then finish the paper with a summing up of the implications of the study. The purpose here is to offer an understanding of your results and support all of your conclusions, using facts from your research and generally accepted information, if suitable. The implication of results should be fully described.

Infer your data in the conversation in suitable depth. This means that when you clarify an observable fact, you must explain mechanisms that may account for the observation. If your results vary from your prospect, make clear why that may have happened. If your results agree, then explain the theory that the proof supported. It is never suitable to just state that the data approved the prospect, and let it drop at that. Make a decision as to whether each premise is supported or discarded or if you cannot make a conclusion with assurance. Do not just dismiss a study or part of a study as "uncertain."

Research papers are not acknowledged if the work is imperfect. Draw what conclusions you can based upon the results that you have, and take care of the study as a finished work.

- You may propose future guidelines, such as how an experiment might be personalized to accomplish a new idea.
- Give details of all of your remarks as much as possible, focusing on mechanisms.
- Make a decision as to whether the tentative design sufficiently addressed the theory and whether or not it was correctly restricted. Try to present substitute explanations if they are sensible alternatives.
- One piece of research will not counter an overall question, so maintain the large picture in mind. Where do you go next? The best studies unlock new avenues of study. What questions remain?
- Recommendations for detailed papers will offer supplementary suggestions.

Approach:

When you refer to information, differentiate data generated by your own studies from other available information. Present work done by specific persons (including you) in past tense.

Describe generally acknowledged facts and main beliefs in present tense.

The Administration Rules

Administration Rules to Be Strictly Followed before Submitting Your Research Paper to Global Journals Inc.

Please read the following rules and regulations carefully before submitting your research paper to Global Journals Inc. to avoid rejection.

Segment draft and final research paper: You have to strictly follow the template of a research paper, failing which your paper may get rejected. You are expected to write each part of the paper wholly on your own. The peer reviewers need to identify your own perspective of the concepts in your own terms. Please do not extract straight from any other source, and do not rephrase someone else's analysis. Do not allow anyone else to proofread your manuscript.

Written material: You may discuss this with your guides and key sources. Do not copy anyone else's paper, even if this is only imitation, otherwise it will be rejected on the grounds of plagiarism, which is illegal. Various methods to avoid plagiarism are strictly applied by us to every paper, and, if found guilty, you may be blacklisted, which could affect your career adversely. To guard yourself and others from possible illegal use, please do not permit anyone to use or even read your paper and file.

Criterion for Grading a Research Paper (Compilation) by Global Journals

Please note that following table is only a Grading of "Paper Compilation" and not on "Performed/Stated Research" whose grading solely depends on Individual Assigned Peer Reviewer and Editorial Board Member. These can be available only on request and after decision of Paper. This report will be the property of Global Journals.

Topics	Grades		
	A-B	**C-D**	**E-F**
Abstract	Clear and concise with appropriate content, Correct format. 200 words or below	Unclear summary and no specific data, Incorrect form Above 200 words	No specific data with ambiguous information Above 250 words
Introduction	Containing all background details with clear goal and appropriate details, flow specification, no grammar and spelling mistake, well organized sentence and paragraph, reference cited	Unclear and confusing data, appropriate format, grammar and spelling errors with unorganized matter	Out of place depth and content, hazy format
Methods and Procedures	Clear and to the point with well arranged paragraph, precision and accuracy of facts and figures, well organized subheads	Difficult to comprehend with embarrassed text, too much explanation but completed	Incorrect and unorganized structure with hazy meaning
Result	Well organized, Clear and specific, Correct units with precision, correct data, well structuring of paragraph, no grammar and spelling mistake	Complete and embarrassed text, difficult to comprehend	Irregular format with wrong facts and figures
Discussion	Well organized, meaningful specification, sound conclusion, logical and concise explanation, highly structured paragraph reference cited	Wordy, unclear conclusion, spurious	Conclusion is not cited, unorganized, difficult to comprehend
References	Complete and correct format, well organized	Beside the point, Incomplete	Wrong format and structuring

INDEX

Global Journal of Science Frontier Research

Visit us on the Web at www.GlobalJournals.org | www.JournalofScience.org
or email us at helpdesk@globaljournals.org

ISSN 9755896